

CHEMICAL KINETICS OF ORGANOPHOSPHORUS FIRE SUPPRESSANTS

A Dissertation

by

TRAVIS GLENN SIKES III

Submitted to the Office of Graduate and Professional Studies of
Texas A&M University
in partial fulfillment of the requirements for the degree of

DOCTOR OF PHILOSOPHY

Chair of Committee,
Co-Chair of Committee,
Committee Members,

Head of Department,

Eric L. Petersen
M. Sam Mannan
Timothy Jacobs
Waruna Kulatilaka
Andreas A. Polycarpou

August 2018

Major Subject: Mechanical Engineering

Copyright 2018 Travis Sikes

ABSTRACT

Organophosphorus compounds (OPCs) have significant fire suppression capabilities but are not well understood. Chemical kinetics mechanisms can provide invaluable information about how OPCs suppress flames; however, the currently available OPC mechanisms are deficient and could use further refinement. In this dissertation, two types of experimental data were taken which can be used as benchmarks to improve mechanisms: laminar flame speeds and ignition delay times. In the laminar flame speed experiments, dimethyl methylphosphonate (DMMP), diethyl methylphosphonate (DEMP), diisopropyl methylphosphonate (DIMP), and trimethyl phosphate (TEP) were added to hydrogen/air and methane/air mixtures to assess their suppression capabilities at 0.1% and 0.3% (DMMP only) of the total mixture volume. The experiments were performed in an optically tracked, spherically expanding flame setup at 1 atm and 120 °C. Results show a 30% decrease in laminar flame speed for all OPCs at 0.1% on the methane/air parent mixture. For the hydrogen/air mixtures, the OPCs differentiate themselves by having an increasing suppression effect corresponding with higher carbon moiety, i.e., DIMP (20% overall reduction), > TEP (15%) > DEMP (13%) > DMMP (9%). The OPCs also have an increasing effect with increasing equivalence ratio on hydrogen/air. Ignition delay time experiments were performed in a glass shock tube at ICARE – CNRS. The simple OPCs studied were dimethyl phosphite (DMP), trimethyl phosphate (TMP), and diethyl phosphite (DEP). The OPCs were added as 10% of the fuel in hydrogen/ethylene mixtures diluted with 98% argon. The results show that the three OPCs behave similarly in both

hydrogen and ethylene mixtures by decreasing the ignition delay time ~30% at high temperatures and then decreasing in effect until the neat and OPC data are indistinguishable. Additionally, quantum chemistry calculations were performed to improve an existing OPC submechanism using ROCBS-QB3 level of theory for thermochemistry and G3X-K for the transition state calculations. The thermochemistry data are an improvement on previous OPC mechanisms, but overall the model does not predict the ignition delay times. Further OPC submechanism improvement is needed to resolve simple OPC reactions so that larger OPC submechanisms will be able to properly predict OPC behavior in applications such as fire suppression.

ACKNOWLEDGMENTS

I would like to thank my advisor, Dr. Eric Petersen. It has been a long journey that began in spring 2011's undergraduate fluid mechanics class and has led me here. I cannot imagine a better advisor and he is one of the biggest reasons why I've come as far as I have. He has taught me persistence in the face of adversity, to always carefully consider all possibilities for anything from an experimental error to developing a new program, and most importantly, through his own example, how to accomplish great things with a strong work ethic. Dr. Petersen is who I imagine as the ideal advisor, teacher, academic, and supervisor. Thank you for taking a chance on me and giving me your support. It has meant more than you may ever know.

I would like to thank my committee co-chair, Dr. Sam Mannan, and my committee members, Dr. Jacobs, and Dr. Kulatilaka for their guidance and support throughout the course of this research.

I am extremely grateful to Dr. Laurent Catoire for hosting me at ENSTA ParisTech. Through this experience I learned about French culture and was able to live the French life for 6 months. My trip was life changing and I will never forget it. I also thank Dr. Pascal Diévert for his time and patience. He taught me everything I know about quantum chemical modeling, and he has also helped me in performing the transition state theory calculations while I was busy with thermochemistry.

A thank you must go to Dr. Nabiha Chaumeix and Dr. Andrea Comandini for their help both professional and personal during my time at CNRS-Orléans. I was only able to

accomplish the quantity and quality of ignition delay experiments with their experience and expertise. Working with both of them was truly a pleasure.

Thanks to my friends and colleagues within the Petersen Research Group. Being able to always have someone that I can bounce ideas off of, get help with a problem, or even just joke around with has made my graduate experience an absolute joy. I only hope that I can one day find another group of coworkers as great as the one I'm leaving, past and present.

Finally, a special thanks to my family for their never-ending encouragement and to my wife for her patience during my entire graduate career and her unshakable love.

CONTRIBUTORS AND FUNDING SOURCES

This work was supported by a dissertation committee consisting of my committee co-chairs Dr. Eric L. Petersen, Nelson-Jackson professor of the Department of Mechanical Engineering, and Dr. M. Sam Mannan, regents professor of the Department of Chemical Engineering and director of Mary Kay O'Connor Process Safety Center; as well as, my committee members Dr. Timothy Jacobs and Dr. Waruna Kulatilaka, professor and associate professor in the Department of Mechanical Engineering, respectively. During the oral defense Dr. Chad Mashuga, assistant professor in the Department of Chemical Engineering, stood in for Dr. M. Sam Mannan.

Flame speed modeling and ignition delay time measurements in Chapter III and Chapter IV were performed with assistance from Dr. Nabiha Chaumeix, Research Director of ICARE-CNRS (Orléans, France), and Dr. Andrea Comandini of ICARE-CNRS.

Quantum chemistry modeling efforts in Chapter V were performed in part with Dr. Laurent Catoire, Director of the UCP in ENSTA ParisTech, and Dr. Pascal Diévert, professor at ENSTA Paristech. Dr. Pascal Diévert has performed the Arrhenius parameter calculations for the updated reactions.

All other work conducted for the dissertation was completed by the student independently.

This research was supported by the Mary Kay O'Connor Process Safety Center, a STEM fellowship from the Chateaubriand Fellowship Program, and the Defense Threat Reduction Agency (DTRA) under grant number HDTRA1-16-1-0031.

TABLE OF CONTENTS

	Page
ABSTRACT	ii
ACKNOWLEDGMENTS.....	iv
CONTRIBUTORS AND FUNDING SOURCES.....	vi
TABLE OF CONTENTS	vii
LIST OF FIGURES	ix
LIST OF TABLES	xii
CHAPTER I INTRODUCTION AND LITERATURE REVIEW	1
I.1 References	8
CHAPTER II LAMINAR FLAME SPEED METHODOLOGY	11
II.1 TAMU Spherically Expanding Flame Facility	11
II.2 Experimental Analysis	16
II.3 References	23
CHAPTER III LAMINAR FLAME SPEED MEASUREMENTS.....	25
III.1 Methane	28
III.2 Hydrogen	32
III.3 Fire Suppressant Comparison.....	36
III.4 Flame Speed Sensitivity Analysis	38
III.5 References	41
CHAPTER IV IGNITION DELAY TIME MEASUREMENTS	44
IV.1 Experimental Facility and Procedure	46
IV.2 Mixtures and Preparation	53
IV.3 OPC Ignition Delay Times in Hydrogen Mixtures	55
IV.4 OPC Ignition Delay Times in Ethylene Mixtures	59
IV.5 References	63

CHAPTER V QUANTUM CHEMISTRY MODELING	65
V.1 Heat of Formation	65
V.2 Sensible Enthalpy, Specific Heat, and Entropy.....	71
V.3 Arrhenius Parameters	81
V.4 Model Comparisons	90
V.5 References	98
CHAPTER VI CONCLUSIONS	102
VI.1 References	105
APPENDIX	106
A.1 Markstein Length Plots	106
A.2 Laminar Flame Speed Sensitivity Plots	107
A.3 CH ₄ Flame Speed Data Tables	110
A.4 H ₂ Flame Speed Data Tables.....	112
A.5 H ₂ Ignition Delay Time Data Tables.....	115
A.6 Neat OPC Ignition Delay Time Data Tables.....	118
A.7 C ₂ H ₄ Ignition Delay Time Data Tables.....	119
A.8 Additional C ₂ H ₄ Ignition Delay Time Modeling Plots	123
A.9 DMP and TMP OPC Submechanism	124

LIST OF FIGURES

	Page
Figure 1. Molecular diagrams of OPCs of interest.....	6
Figure 2. High-temperature, high-pressure (HTHP) laminar flame speed vessel at Texas A&M University	12
Figure 3. (a) Modified Z-type schlieren schematic and (b) Lens-based schlieren schematic used on the HTHP vessel. Lenses are plano-convex. Lens #1 is Ø50.8 mm, f = 100 mm and lens #2 is Ø200 mm, f = 800 mm.....	13
Figure 4. Contrast-adjusted images of ~120°C, 1 atm flames for (a) Methane/ 0.1% DEMP, $\phi = 1.1$ and (b) Hydrogen/ 0.1% TEP, $\phi = 1.9$	15
Figure 5. Conceptual solution paths for laminar flame speed extrapolation by (a) differentiating experimental data and (b) the integrating extrapolation model.	19
Figure 6. The effect of local 2nd-order polynomial smoothing on laminar flame speed data based on smoothing span % of data.	20
Figure 7. (a) Sample dr/dt -versus-stretch plot and (b) accompanying histogram of possible flame speed values within bounds (gray dashed lines) of CH ₄ /air mixture at $\phi = 1$, 1 atm, and 294.4 K.	22
Figure 8. Laminar flame speeds of OPCs in methane/air mixtures at 1 atm, 120 °C.	29
Figure 9. Laminar flame speeds of DIMP in methane/air mixtures at 1 atm, 120 °C. The DIMP model curve is calculated using the Glaude et al. [9] mechanism, which is the precursor to the LLNL model.	31
Figure 10. Laminar flame speeds of OPCs in hydrogen/air mixtures at 1 atm, 120 °C.	32
Figure 11. Laminar flame speeds of DIMP in hydrogen/air mixtures at 1 atm, 120 °C. The DIMP model curve is calculated using the Glaude et al. [9] mechanism.	34
Figure 12. Laminar flame speeds of DIMP in hydrogen/air mixtures at $\phi = 1.6$, 1 atm, 120 °C. The DIMP model curve is calculated using the Glaude et al. [9] mechanism.	35

Figure 13. Qualitative comparison of fire suppressant effect of OPCs (1 atm, 120 °C) to more-established fire suppressants: Halon 1301 (CF ₃ Br) [2] and C ₂ HF ₅ [17] (1 atm, 21 °C). The 21 °C data are temperature corrected to 393 K. Filled circles are the current data and the solid lines are their experimental fits. Open circles are previous fire suppressant studies at TAMU with dashed lines as their experimental fits.	37
Figure 14. Top 10 OPC reactions containing phosphorous of 0.1% DMMP/CH ₄ /air relative laminar flame speed sensitivity at 1 atm, 120 °C.	39
Figure 15. Shock-tube schematic and x-t diagram.	44
Figure 16. Characteristic timer signals in the glass shock tube. Timers are spaced by 150 mm and are numbered 1 – 4 from bottom to top.	48
Figure 17. Representative velocity fitting (left) and attenuation (right) plot based on timer data from Figure 16. The dashed lines are experimental fits and the red line is the fit extrapolated to the endwall.	50
Figure 18. Sample signals from shock-tube experiments. From top to bottom: OH* emission profile, endwall pressure, and timer 4 signal. P ₅ is calculated from normal shock relations, Eq. 1.	52
Figure 19. Hydrogen ignition delay times at $\phi = 1.0$, diluted with 98% argon. TAMU data are from Krejci et al. [9] and Kéromnès et al. [10]. ICARE T ₅ uncertainty is estimated to be 1%.	56
Figure 20. Hydrogen-based ignition delay times ($\phi = 0.5$, 1 atm, diluted with 98% argon). ICARE T ₅ uncertainty is estimated to be 1%.	57
Figure 21. Concentration-varying experiments. The base OPC/H ₂ are $\phi = 0.5$ and the concentrations are modified by replacing H ₂ with Ar. ICARE T ₅ uncertainty is estimated to be 1%.	58
Figure 22. Ethylene-based ignition delay times ($\phi = 1.0$, 1 atm, diluted with 98% argon). ICARE T ₅ uncertainty is estimated to be 1%.	60
Figure 23. Ethylene-based ignition delay times ($\phi = 0.5$, 1 atm, diluted with 98% argon). ICARE T ₅ uncertainty is estimated to be 1%.	61
Figure 24. Normalized ethylene OH* sidewall profiles ($\phi = 1.0$, 1 atm, diluted with 98% argon). Temperature uncertainty is 1%.	62
Figure 25. O ₂ thermodynamic fitting error compared to NIST reference data [15]. The heat of formation constraint is $\Delta H_f, O_2 = 0$	76

Figure 26. Thermodynamic data comparison for (upper) DMP and (lower) TMP.....	78
Figure 27. Thermodynamic data comparison for (upper) PO[OH]Me and (lower) PO[OH]Me[Oet].	79
Figure 28. A potential energy surface of two reactants (A, B) into products along a reaction coordinate.....	82
Figure 29. Optimized geometry at G3X-K level of theory of the reaction $\text{DMP} + \text{CH}_3 \rightleftharpoons \text{TS} \rightarrow \text{PO[Ome]}_2 + \text{CH}_4$. Optimized (a) reactants' geometries, (b) transition state geometry, and (c) products' geometries.	86
Figure 30. Hydrogen based ignition delay time modeling comparison ($\phi = 0.5$, 1 atm, diluted with 98% argon).	92
Figure 31. Direct comparison of hydrogen DMP and TMP ignition delay time modeling ($\phi = 0.5$, 1 atm, diluted with 98% argon).....	94
Figure 32. 10% DMP/90% ethylene ignition delay times at (a) $\phi = 0.5$ and (b) $\phi = 1.0$, 1 atm, diluted with 98% argon. ICARE T ₅ uncertainty is estimated to be 1%.	95
Figure 33. Experimental and model OH* profiles for (a) 10% DMP/ 10% H ₂ $\phi = 0.5$, 1447 K, 1.03 atm and (b) 10% DMP/ 90% C ₂ H ₄ $\phi = 1.0$, 1524.5 K, 1.05 atm.	97
Figure A-1. Burned Markstein lengths of OPCs in methane/air mixture at 1 atm, 120 °C. Dashed lines represent experimental fits.....	106
Figure A-2. Burned Markstein lengths of OPCs in hydrogen/air mixture at 1 atm, 120 °C. Dashed lines represent experimental fits.....	106
Figure A-3. Top 10 OPC reactions of 0.1% DMMP/H ₂ /air relative laminar flame speed sensitivity at 1 atm, 120 °C.....	107
Figure A-4. Top 10 OPC reactions of 0.1% DIMP/CH ₄ /air relative laminar flame speed sensitivity at 1 atm, 120 °C.....	108
Figure A-5. Top 10 OPC reactions of 0.1% DIMP/H ₂ /air relative laminar flame speed sensitivity at 1 atm, 120 °C.....	109
Figure A-6. Ethylene-based ignition delay times ($\phi = 0.5$, 1 atm, diluted with 98% argon). ICARE T ₅ uncertainty is estimated to be 1%.	123
Figure A-7. Ethylene-based ignition delay times ($\phi = 1.0$, 1 atm, diluted with 98% argon). ICARE T ₅ uncertainty is estimated to be 1%.	123

LIST OF TABLES

	Page
Table 1. Top reactions ranked from most important to least (1 – 10) for each set of sensitivity analyses performed.....	40
Table 2. Heats of formation of various methods with BAC for known literature species. Units are kcal/mol. Literature references: ^a Chase [15], ^b Gurvich et al. [17], ^c Cox et al. [18], ^d Luo [19] , ^e Berkowitz et al. [20], ^f Gunn and Green [21], ^g Gingerich [22], ^h Potter and DiStefano [23], ⁱ Gaydon [24], ^j Hildenbrand and Lau [25], ^k Hartley [26], ^l Dorofeeva and Moiseeva [3], ^m Rabinovich et al. [27], ⁿ Al-Maydama et al. [28], ^o Davies et al. [29], ^p Luo and Benson [30], ^q Lodders [14].....	70
Table 3. New CH ₃ OPO and CH ₂ OPO reactions valid at 1 atm and 500 – 2500 K.....	88
Table 4. DMP unimolecular decomposition, H abstraction, and radical decomposition reactions valid at 1 atm and 500 – 2500 K.....	89
Table A-1. Laminar flame speed data for neat CH ₄ /air.....	110
Table A-2. Laminar flame speed data for TEP/CH ₄ /air.....	110
Table A-3. Laminar flame speed data for 0.1% DEMP/CH ₄ /air.....	111
Table A-4. Laminar flame speed data for DMMP/CH ₄ /air.....	111
Table A-5. Laminar flame speed data for DIMP/CH ₄ /air.	112
Table A-6. Laminar flame speed data for Neat H ₂ /air.	112
Table A-7. Laminar flame speed data for 0.1% TEP/H ₂ /air.	113
Table A-8. Laminar flame speed data for 0.1% DEMP/H ₂ /air.	113
Table A-9. Laminar flame speed data for DMMP/H ₂ /air.....	114
Table A-10. Laminar flame speed data for DIMP/H ₂ /air.	115
Table A-11. Hydrogen ignition delay times at $\phi = 0.5$ and 98% Ar dilution (1.00% H ₂ / 1.00% O ₂ / 98.00% Ar).	115
Table A-12. Hydrogen ignition delay times at $\phi = 1.0$ and 98% Ar dilution (1.35% H ₂ / 0.67% O ₂ / 97.98% Ar).	116

Table A-13. Hydrogen/DMP ignition delay times at $\phi = 0.5$ and 98% Ar dilution (0.08% DMP/0.69% H ₂ / 1.23% O ₂ / 97.99% Ar).....	116
Table A-14. Hydrogen/DEP ignition delay times at $\phi = 0.5$ and 98% Ar dilution (0.07% DEP/0.56% H ₂ / 1.37% O ₂ / 98.00% Ar).....	117
Table A-15. Hydrogen/TMP ignition delay times at $\phi = 0.5$ and 98% Ar dilution (0.08% TMP/0.63% H ₂ / 1.31% O ₂ / 97.98% Ar).	117
Table A-16. DEP ignition delay times with hydrogen from Table A-14 replaced with Ar. (0.007% DEP/ 1.38% O ₂ / 98.56% Ar).	118
Table A-17. TMP ignition delay times with hydrogen from Table A-15 replaced with Ar. (0.008% TMP/ 1.31% O ₂ / 98.61% Ar).	118
Table A-18. Ethylene ignition delay times at $\phi = 0.5$ and 98% Ar dilution (0.29% C ₂ H ₄ / 1.71% O ₂ / 98.00% Ar).	119
Table A-19. Ethylene ignition delay times at $\phi = 1.0$ and 98% Ar dilution (0.5% C ₂ H ₄ / 1.50% O ₂ / 98.00% Ar).	119
Table A-20. Ethylene/DMP ignition delay times at $\phi = 0.5$ and 98% Ar dilution (0.03% DMP/0.25% C ₂ H ₄ / 1.72% O ₂ / 97.99% Ar).....	120
Table A-21. Ethylene/DMP ignition delay times at $\phi = 1.0$ and 98% Ar dilution (0.05% DMP/0.44% C ₂ H ₄ / 1.51% O ₂ / 97.99% Ar).....	120
Table A-22. Ethylene/DEP ignition delay times at $\phi = 0.5$ and 98% Ar dilution (0.03% DEP/0.23% C ₂ H ₄ / 1.73% O ₂ / 98.01% Ar).....	121
Table A-23. Ethylene/DEP ignition delay times at $\phi = 1.0$ and 98% Ar dilution (0.05% DEP/0.41% C ₂ H ₄ / 1.54% O ₂ / 98.00% Ar).....	121
Table A-24. Ethylene/TMP ignition delay times at $\phi = 0.5$ and 98% Ar dilution (0.03% TMP/0.24% C ₂ H ₄ / 1.72% O ₂ / 98.00% Ar).	122
Table A-25. Ethylene/TMP ignition delay times at $\phi = 1.0$ and 98% Ar dilution (0.05% TMP/0.43% C ₂ H ₄ / 1.52% O ₂ / 98.00% Ar).	122
Table A-26. DMP/TMP mechanism thermodynamic properties.	124
Table A-27. DMP/TMP mechanism.	128
Table A-28. DMP/TMP submechanism transport properties.....	137

CHAPTER I

INTRODUCTION AND LITERATURE REVIEW*

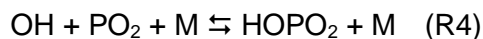
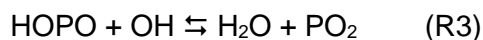
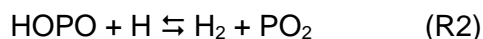
Halon 1301 (CF_3Br) has historically been the standard of fire suppressants. Halon 1301 was developed in the 1950's, and shortly thereafter, the interest in investigating new fire suppressants diminished until it was found that Halon 1301 was causing ozone depletion [2]. Since being phased out in the Montreal Protocol, the usage of Halon 1301 has been virtually eliminated, leaving room for new investigations into fire suppressants that can meet or exceed the capabilities of Halon 1301 [3]. Initial interest in Halon 1301 replacements was focused on closely related halogenated species; however, such studies only elucidated the poor relative performance of the closely related molecules [4]. Upon this discovery, effort was redirected into investigating chemical species that had a few more undesirable traits such as unfavorable physical characteristics or higher toxicity [5]. One of the families of interest was organophosphorus compounds (OPCs)

Recent fire suppressant studies [6, 7] have shown that the phosphorus atom from dimethyl methylphosphonate (DMMP) is more effective by a factor of around 4 to 6, respectively, than bromine and CF_3Br at lower concentration, whereas the performance of DMMP is close to CF_3Br at higher concentrations. However, based on purely numerical results, Babushok et al. [7] found that the burning velocity of hydrocarbons is actually

* Part of this chapter is reprinted with permission from [1] T. Sikes, O. Mathieu, W. Kulatilaka, M.S. Mannan, E.L. Petersen, Laminar Flame Speeds of DEMP, DMMP, and TEP Added to H_2 - and CH_4 -Air Mixtures, Proc. Combust. Inst. (accepted) by Elsevier.

increased by the addition of DMMP for lean flames due to the hydrocarbon moiety of DMMP. Thus the more complex molecules cannot technically be called fire suppressants although they have been shown to have significant suppression effects under most conditions.

The inhibition mechanism from P-containing fire suppressants can be summarized as follows from the work of Twarowski [8-10]:



As can be seen, the phosphorus-inhibiting chemistry acts catalytically on the important combustion radicals H and OH through the following species: PO₂, HOPO, and HOPO₂. Because of this catalytic mechanism, as stated in Korobeinichev et al. [11], the only distinction between different organophosphate inhibitors appears to be how rapidly these catalytic cycles are established. However, it is important to mention that this mechanism is based on reactions that have been estimated only, using simplified RRKM calculations [8], and subsequent experimental validation was not direct since it consisted of measuring the recombination of H and OH radicals from the photolysis of water vapor in the presence of phosphine (PH₃) [9, 10, 12]. This mechanism was later modified, notably by using quantum chemical methods to improve the thermochemistry of the phosphorous compounds [11, 13]. The thermochemistry was also improved in more recent

studies, such as in the computational work on organophosphorus combustion chemistry by Sullivan et al. [14] or in the work of Khalfa et al. [15] where the thermochemistry of DMMP was re-estimated by using both the CBS-QB3 composite method and the group contribution method. The new thermodynamic data proposed in the two latest studies significantly impact the predictions of ignition delay time from DMMP-based mixtures, as can be seen in Mathieu et al. [16]. Recently, Babushok et al. [7] added a few reactions to the kinetics scheme:



On the experimental side, studies of P-containing fire suppressants either did not measure any species containing phosphorus [6, 13, 17, 18] or did so for very-low-pressure flames (less than 50 Torr), which are far from practical conditions [19, 20]. The only studies where the chemical species responsible for the fire suppression mechanism (PO_2 , HOPO , and HOPO_2) were followed at atmospheric pressure were in the more recent work from Korobeinichev et al. [11, 21]. In these studies, PO_2 , HOPO , and HOPO_2 were sampled in premixed laminar flames at various heights above the burner using a quartz probe. However, this type of method can typically induce uncertainties in the temperature (measured by thermocouples), while the probe can disturb the flame. For instance, Korobeinichev et al. [11] reported some interactions between phosphorus and the probe to form phosphate glass.

For laminar flame speed experiments, literature data are also sparse. There was a study by Rybitskaya et al. [22] in which the heat flux method was applied to studying TMP in methane- and propane-air mixtures at 35°C, 1 atm, but was limited to only a single OPC. Other studies include the previously mentioned study by Korobeinichev et al. [11], in which a brief excursion into various OPC laminar flame speeds in stoichiometric propane/air were measured using the Bunsen burner method. This study, while being more comprehensive in the number of compounds studied, only looked at a single fuel at a single equivalence ratio. A more comprehensive study that takes the middle ground of choosing a few OPCs to investigate with multiple fuels and over a wide range of equivalence ratios could therefore begin to fill in gaps in our understanding of OPCs.

Interestingly, TEP and other OPCs are also common surrogates for Sarin gas ($\text{C}_4\text{H}_{10}\text{FO}_2\text{P}$), a deadly nerve agent classified as a chemical weapon of mass destruction [23]. There is historical literature [11, 19, 20, 24-27] that focuses on simulating the controlled destruction of Sarin stockpiles, most often by using surrogates. Given the danger that Sarin gas poses, it is of interest to develop countermeasures that would be effective in uncontrolled settings; however, simulating such a countermeasure also requires more-detailed kinetic data than currently exists. It is fortuitous that the kinetic information acquired by investigating organophosphorus compounds can also be used to investigate Sarin countermeasures.

One can therefore conclude from this review that experimental data are critically needed to validate detailed kinetics mechanisms for P-containing fire suppressants and that current kinetics mechanisms are probably not mature enough to conduct numerical

studies on the fire-suppressant effectiveness of these agents over a large range of conditions. Such a well-validated mechanism could also be used to develop Sarin countermeasures. The aim of the present study was therefore to provide well-characterized data on the fire suppressing properties of phosphorus-containing liquid agents, as well as to improve upon existing OPC mechanisms. The two most prominent models are from Jayaweera et al. [13], the LLNL model, and Korobeinichev et al. [28], the NIST model. Of these two models, the NIST model is based heavily upon the LLNL model. The molecules of interest in the current study are shown in Figure 1.

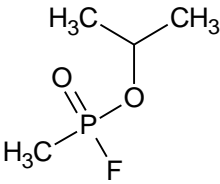
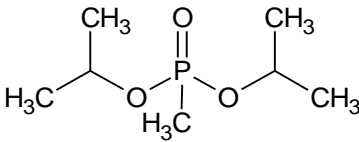
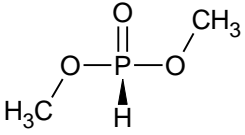
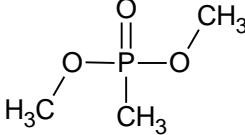
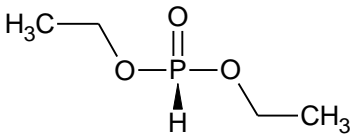
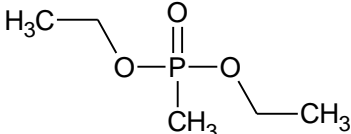
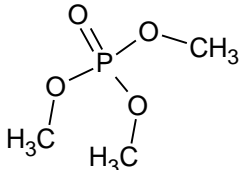
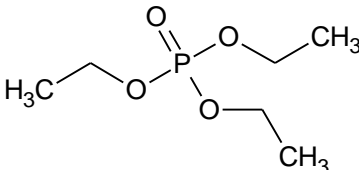
 <p>Sarin</p>	 <p>Diisopropyl methylphosphonate (DIMP)</p>
 <p>Dimethyl phosphite (DMP)</p>	 <p>Dimethyl methylphosphonate (DMMP)</p>
 <p>Diethyl phosphite (DEP)</p>	 <p>Diethyl methylphosphonate (DEMP)</p>
 <p>Trimethyl phosphate (TMP)</p>	 <p>Triethyl phosphate (TEP)</p>

Figure 1. Molecular diagrams of OPCs of interest.

All of the molecules in Figure 1 include methyl and methoxy groups connected to a central phosphorus atom double bonded to an oxygen atom. The Sarin surrogates, DMMP, DEMP, DIMP, and TEP, share very similar structures to Sarin with the exception

of not including a fluorine atom. The Sarin surrogates may not all be ideal; however, they were already predefined by the community at large and served as a convenient starting point for this project. Ignition delay time experiments have already been performed by Mathieu et al. for DMMP [29], DEMP (under review), DIMP (unpublished), and TEP [30]. Additionally, DMP, DEP, and TMP have been identified as useful molecules from which a mechanism can be built around and then extended to the more complex molecules. This extrapolation to other molecules is because DMP, DEP and TMP share similar structures to DMMP, DEMP, and TEP, respectively. These molecules are investigated in ignition delay time experiments, performed at ICARE-CNRS and described in this thesis, as well as through quantum chemical calculations, performed at ENSTA ParisTech, to improve upon existing chemical kinetics mechanisms.

A comprehensive explanation of the TAMU spherically expanding flame methodology follows in Chapter II. Chapter III contains the laminar flame speeds of DMMP, DEMP, DIMP and TEP in hydrogen/air and methane/air mixtures. Chapter IV gives a brief description of the shock-tube facility and procedure at ICARE-CNRS followed by the ignition delay time measurements involving DMP, DEP, and TMP. This material culminates in Chapter V, where the process and results of using quantum chemical calculations to create a chemical kinetics mechanism for DMP and TMP are discussed. Finally, a brief conclusion and recommendation for future studies is given in Chapter VI.

I.1 References

- [1] T. Sikes, O. Mathieu, W. Kulatilaka, M.S. Mannan, E.L. Petersen, Laminar Flame Speeds of DEMP, DMMP, and TEP Added to H₂- and CH₄-Air Mixtures, *Proc. Combust. Inst.* (accepted).
- [2] S.A. Montzka, J.H. Butler, R.C. Myers, T.M. Thompson, T.H. Swanson, A.D. Clarke, L.T. Lock, J.W. Elkins, Decline in the tropospheric abundance of halogen from halocarbons: Implications for stratospheric ozone depletion, *Science* 272 (1996) 1318-1322.
- [3] U.S.C.S.C.o.F. Relations, Montreal Protocol on Substances That Deplete the Ozone Layer, Message from the President.
- [4] A. Hamins, D. Trees, K. Seshadri, H.K. Chelliah, Extinction of nonpremixed flames with halogenated fire suppressants, *Combust. Flame* 99 (1994) 221-230.
- [5] M.A. MacDonald, T.M. Jayaweera, E.M. Fisher, F.C. Gouldin, Inhibition of nonpremixed flames by phosphorus-containing compounds, *Combust. Flame* 116 (1999) 166-176.
- [6] N. Bouvet, G.T. Linteris, V.I. Babushok, F. Takahashi, V.R. Katta, R. Krämer, A comparison of the gas-phase fire retardant action of DMMP and Br₂ in co-flow diffusion flame extinguishment, *Combust. Flame* 169 (2016) 340-348.
- [7] V.I. Babushok, G.T. Linteris, V.R. Katta, F. Takahashi, Influence of hydrocarbon moiety of DMMP on flame propagation in lean mixtures, *Combust. Flame* 171 (2016) 168-172.
- [8] A. Twarowski, The influence of phosphorus oxides and acids on the rate of H + OH recombination, *Combust. Flame* 94 (1993) 91-107.
- [9] A. Twarowski, Photometric determination of the rate of H₂O formation from H and OH in the presence of phosphine combustion products, *Combust. Flame* 94 (1993) 341-348.
- [10] A. Twarowski, Reduction of a phosphorus oxide and acid reaction set, *Combust. Flame* 102 (1995) 41-54.
- [11] O.P. Korobeinichev, V.M. Shvartsberg, A.G. Shmakov, T.A. Bolshova, T.M. Jayaweera, C.F. Melius, W.J. Pitz, C.K. Westbrook, H. Curran, Flame inhibition by phosphorus-containing compounds in lean and rich propane flames, *Proc. Combust. Inst.* 30 (2005) 2353-2360.

- [12] A. Twarowski, The temperature dependence of $H + OH$ recombination in phosphorus oxide containing post-combustion gases, *Combust. Flame* 105 (1996) 407-413.
- [13] T.M. Jayaweera, C.F. Melius, W.J. Pitz, C.K. Westbrook, O.P. Korobeinichev, V.M. Shvartsberg, A.G. Shmakov, I.V. Rybitskaya, H.J. Curran, Flame inhibition by phosphorus-containing compounds over a range of equivalence ratios, *Combust. Flame* 140 (2005) 103-115.
- [14] P.A. Sullivan, R. Sumathi, W.H. Green, J.W. Tester, Ab initio modeling of organophosphorus combustion chemistry, *Phys. Chem. Chem. Phys.* 6 (2004) 4296-4309.
- [15] A. Khalfa, M. Ferrari, R. Fournet, B. Sirjean, L. Verdier, P.A. Glaude, Quantum chemical study of the thermochemical properties of organophosphorous compounds, *J. Phys. Chem. A* 119 (2015) 10527-10539.
- [16] O. Mathieu, W.D. Kulatilaka, E.L. Petersen, Experimental and Modeling Study on the Effects of Dimethyl Methylphosphonate (DMMP) Addition on H_2 , CH_4 , and C_2H_4 Ignition, *Combust. Flame* (submitted).
- [17] M.F.M. Nogueira, E.M. Fisher, Effects of dimethyl methylphosphonate on premixed methane flames, *Combust. Flame* 132 (2003) 352-363.
- [18] J.E. Siow, N.M. Laurendeau, Flame inhibition activity of phosphorus-containing compounds using laser-induced fluorescence measurements of hydroxyl, *Combust. Flame* 136 (2004) 16-24.
- [19] O.P. Korobeinichev, S.B. Ilyin, T.A. Bolshova, V.M. Shvartsberg, A.A. Chernov, The chemistry of the destruction of organophosphorus compounds in flames—III: the destruction of DMMP and TMP in a flame of hydrogen and oxygen, *Combust. Flame* 121 (2000) 593-609.
- [20] O.P. Korobeinichev, S.B. Ilyin, V.M. Shvartsberg, A.A. Chernov, The destruction chemistry of organophosphorus compounds in flames—I: quantitative determination of final phosphorus-containing species in hydrogen-oxygen flames, *Combust. Flame* 118 (1999) 718-726.
- [21] O.P. Korobeinichev, V.M. Shvartsberg, A.G. Shmakov, D.A. Knyazkov, I.V. Rybitskaya, Inhibition of atmospheric lean and rich $CH_4/O_2/Ar$ flames by phosphorus-containing compound, *Proc. Combust. Inst.* 31 (2007) 2741-2748.

- [22] I.V. Rybitskaya, A.G. Shmakov, O.P. Korobeinichev, Propagation velocity of hydrocarbon-air flames containing organophosphorus compounds at atmospheric pressure, *Combust. Explos. Shock Waves* 43 (2007) 253-257.
- [23] P.A. Glaude, C. Melius, W.J. Pitz, C.K. Westbrook, Detailed chemical kinetic reaction mechanisms for incineration of organophosphorus and fluoroorganophosphorus compounds, *Proc. Combust. Inst.* 29 (2002) 2469-2476.
- [24] T.N. Obee, S. Satyapal, Photocatalytic decomposition of DMMP on titania, *J. Photochem. Photobiol., A* 118 (1998) 45-51.
- [25] J.H. Werner, T.A. Cool, Kinetic model for the decomposition of DMMP in a hydrogen/oxygen flame, *Combust. Flame* 117 (1999) 78-98.
- [26] B. Veriansyah, J.-D. Kim, J.-C. Lee, Destruction of chemical agent simulants in a supercritical water oxidation bench-scale reactor, *J. Hazard. Mater.* 147 (2007) 8-14.
- [27] A. Mattsson, C. Lejon, V. Štengl, S. Bakardjieva, F. Opluštil, P.O. Andersson, L. Österlund, Photodegradation of DMMP and CEES on zirconium doped titania nanoparticles, *Appl. Catal., B* 92 (2009) 401-410.
- [28] O.P. Korobeinichev, V.M. Shvartsberg, A.G. Shmakov, The chemistry of combustion of organophosphorus compounds, *Russ. Chem. Rev.* 76 (2007) 1094.
- [29] O. Mathieu, W.D. Kulatilaka, E.L. Petersen, Experimental and modeling study on the effects of dimethyl methylphosphonate (DMMP) addition on H₂, CH₄, and C₂H₄ ignition, *Combust. Flame* 191 (2018) 320-334.
- [30] O.E. Mathieu, W.D. Kulatilaka, E.L. Petersen, Shock-tube studies of tri-ethyl-phosphate (TEP) kinetics at high temperatures in: 55th AIAA Aerospace Sciences Meeting, American Institute of Aeronautics and Astronautics, 2017.

CHAPTER II

LAMINAR FLAME SPEED METHODOLOGY*

The measurement of the laminar flame speed of a fuel-oxidizer mixture provides a fundamental property of the mixture that depends on the chemical kinetics and the transport properties of the species therein. It also provides one of the few laboratory measurements wherein the full chemical kinetics can be solved along with the 1-D fluid mechanics to arrive at a calculated solution that can be compared directly to the 1-D data. A spherically expanding flame is one of the standard methods for determining the laminar flame speed of a mixture in the laboratory. A review of the methodology for measuring laminar flame speeds in the author's laboratory is provided in this chapter.

II.1 TAMU Spherically Expanding Flame Facility

The laminar flame speed facility at Texas A&M University (TAMU) has been integral in studies for over a decade [2-6]. In the present study, the high-temperature, high-pressure (HTHP) laminar flame speed vessel, Figure 2, was utilized. This vessel is capable of initial pressures of 10 atm, limited by the structural integrity of the large optical windows, and temperatures of 475 K, limited by the life of the sealing O-rings. These experiments are performed at 120 °C and 1 atm. Heating the vessel is performed by a heating jacket which can be seen in Figure 2.

* Part of this chapter is reprinted with permission from [1] T. Sikes, M.S. Mannan, E.L. Petersen, An experimental study: Laminar flame speed sensitivity from spherical flames in stoichiometric CH₄–air mixtures, Combust. Sci. Technol. (2018) 1-20 by Taylor & Francis.

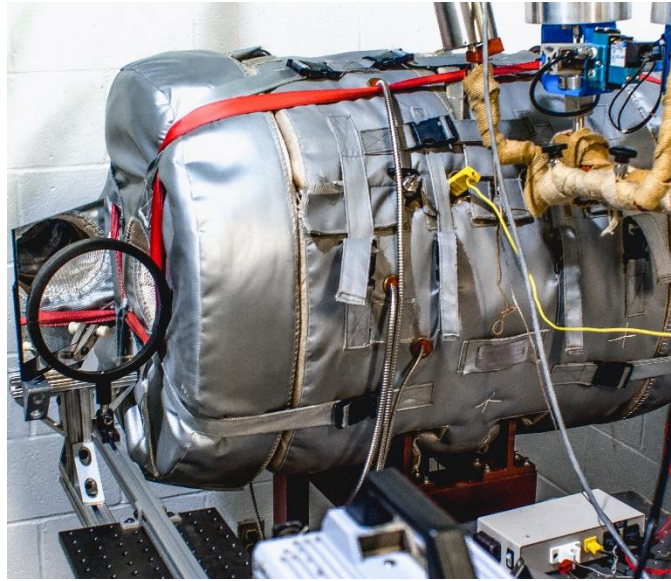


Figure 2. High-temperature, high-pressure (HTHP) laminar flame speed vessel at Texas A&M University

Additionally, the camera section of the current lens-based schlieren system can be seen on the left side of Figure 2. A schlieren system is possible because the vessel is optically accessible via opposed windows that allow the transmission of collimated light from a mercury arc lamp (not shown). The schlieren setup was modified from a previous mirror-based, modified Z-type schlieren system, Figure 3a, to the current lens-based schlieren system, Figure 3b, to accommodate a new flame speed vessel in the same test cell.

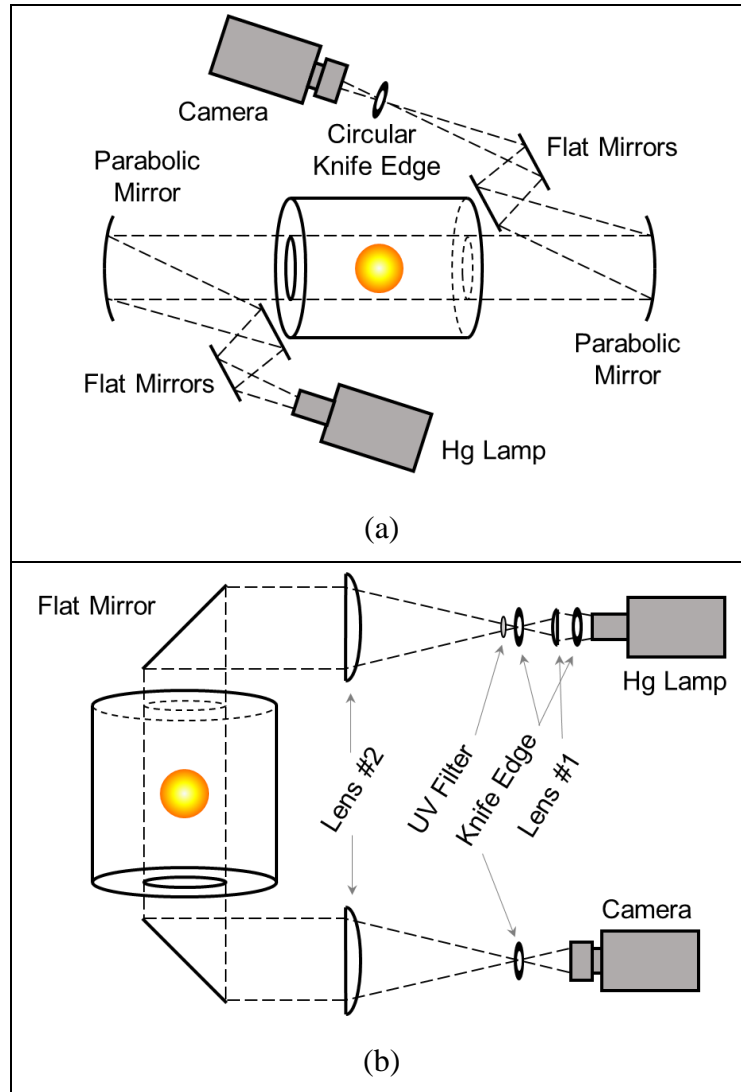


Figure 3. (a) Modified Z-type schlieren schematic and (b) Lens-based schlieren schematic used on the HTHP vessel. Lenses are plano-convex. Lens #1 is Ø50.8 mm, $f = 100$ mm and lens #2 is Ø200 mm, $f = 800$ mm.

A schlieren system works under the premise that a point light source can be put at the focal length of either a mirror or lens and collimated through an area of interest. This process is then reversed to focus the collimated beam into a camera with a circular knife

edge at the focal length of the decollimating mirror or lens to amplify density gradients. Additional information about this phenomenon can be found in Settles [7].

The issue that occurs with Z-type schlieren systems is that the angle between the point source (lamp) and parabolic mirror must be kept small to avoid aberrations (the same is true for decollimation). This angle limitation can be slightly remedied by using pairs of flat mirrors to alter the beam path if the angle between the lamp and parabolic mirror becomes too great, but even this solution has its limits. This modified schlieren system is also quite difficult to align properly. The origin of the problem is the inherent coupling, caused by the parabolic mirror, between altering the beam angle and focusing the beam. Another way to fix the problem is to decouple the beam angle from the component that focuses the beam. This decoupling can be done using lenses to collimate the beam and flat mirrors to redirect the collimated beam.

For either method, the end result is that the beam is focused into a high-speed camera and is used to obtain the time history of the growth of the spherical, laminar flame. Typical single-frame images of the resulting flame for different mixtures are shown in Figure 4 with contrast adjustment for visual clarity.

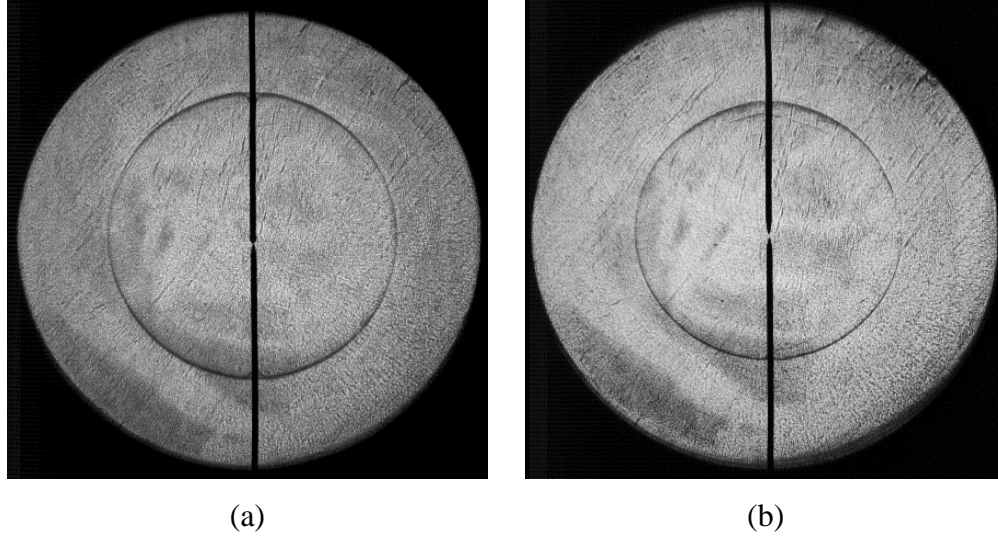


Figure 4. Contrast-adjusted images of $\sim 120^\circ\text{C}$, 1 atm flames for (a) Methane/ 0.1% DEMP, $\phi = 1.1$ and (b) Hydrogen/ 0.1% TEP, $\phi = 1.9$.

The minimum spatial resolution in this setup is at least less than 1 mm because the spark gap distance in Figure 3a can be resolved and is less than that distance. The camera is often used with the resolution of 448×464 to maximize the frame rate for hydrogen flames. With this resolution and knowing that the window diameter is 12.7 cm, the minimum spatial resolution is calculated to be approximately 0.6 mm. This resolution is calculated knowing that the minimum spatial resolution is when two pixels can distinguish a feature and thus $Res_{spatial} = 2 \times (Field\ of\ View)/Res_{cam}$. Here the field of view is assumed to be the size of the window, and Res_{cam} is the smallest value of the camera resolution.

II.2 Experimental Analysis

Images collected during the experiment, Figure 4, are processed using a Matlab-based edge-detection program developed in-house. To calculate a conversion between pixels and known physical dimensions, the edge-detection program must first find the viewing port edge by changing the contrast and using the Canny method, a robust edge detection method [8, 9]. The viewing port edge is simplified by fitting the perimeter with an ellipse using the algebraic Taubin method [10]. Images can be slightly corrected by computing an affine transformation from the fit ellipse, the viewing port edge, to a circle. Generally, the images are altered very little by this process, but it is done nonetheless as a correction to make certain that the viewing port is circular because the schlieren setup can slightly skew it. The pixels-to-cm conversion is calculated from the viewing port edge and is later applied to the detected flame edges to calculate the radii. The flame edge detection is performed by first either subtracting each frame from the previous flame or from an initial reference frame. If the flame is subtracted from the reference frame, the later images can become lighter because of the light emitted from the combustion event. For this reason, the author chose to subtract each frame from the previous. The edge is detected in the same fashion as previously described for the viewing port edge with the exception that a circle is best fit instead of an ellipse.

The raw flame speed data, measured from the Z-type schlieren system, are in a stretched, burned state and must be processed to extrapolate it to an unstretched, burned state. In the literature, the linear extrapolation method (LM), Eq. 2.1, has been used frequently. However, while LM can be accurate when the Lewis number is close to unity,

non-linear methods are much more capable of providing accurate flame speed measurements when the Lewis number deviates from unity [11, 12]. One such nonlinear method, Eq. 2.2, first suggested by Markstein [13] and later by Frankel and Sivashinsky [14] attempts to account for nonlinear effects in the extrapolation. Equation 2.3, referred to herein as NM II, was first proposed by Kelley et al. [15] and is based on the works of Ronney and Sivashinsky [16] and Bechtold et al. [17]. A numerical study performed by Chen [12] found that NM I is accurate when $Le > 1$ (positive Markstein lengths), NM II is accurate when $Le < 1$ (negative Markstein lengths), and both are sufficient near unity. Once S_b^0 is determined, it is multiplied by the burned-to-unburned density ratio (derived from conservation of mass across the flame front), calculated using an equilibrium solver such as Chemkin or COSILAB, for the final unburned, unstretched flame speed, S_L^0 .

$$\text{LM: } S_b = S_b^0 - L_b(2/r_f S_b) \quad (2.1)$$

$$\text{NM I: } S_b = S_b^0 - S_b^0 L_{m,b}(2/r_f) \quad (2.2)$$

$$\text{NM II: } \ln S_b = \ln S_b^0 - S_b^0 L_{m,b}(2/r_f S_b) \quad (2.3)$$

In the above equations, the undefined variables $L_{m,b}$ and r_f are the burned Markstein length and flame radius, respectively. Historically, the linear extrapolation method was solved by either best-fitting the derivative of the experimental radius time history to LM or integrating LM and then best-fitting the data.

Both of these solution methods are sensitive to smoothing and the cutoff locations. Solving extrapolation methods by derivative involves smoothing (optional),

differentiating the data, determining the cutoff locations, and finding the parameters that best fit the data. When differentiating the data, first-order finite difference schemes are used. The integral approach is conceptually easier and has no uncertainties associated with numerically differentiating the data, but is otherwise similar in that smoothing can be performed, cutoff locations determined, and the parameters are best-fit after numerically integrating the extrapolation equation. The integration solution should be slightly more accurate because the numerical integration has no predetermined time step, whereas the numerical differentiation is limited to the data time step. These two general schematics for solving the extrapolation equations are conceptualized in Figure 5. NM I and NM II were integrated using MATLAB's ODE45 and ODE15i, respectively. The best-fit was performed by MATLAB's nlinfit function when possible or a combination of fminsearch and fminunc (to properly calculate the hessian for uncertainty) if nlinfit fails to converge.

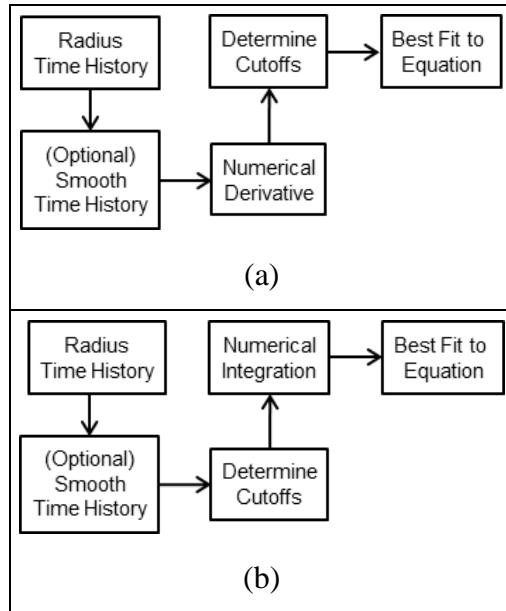


Figure 5. Conceptual solution paths for laminar flame speed extrapolation by (a) differentiating experimental data and (b) the integrating extrapolation model.

From the author's experience, changing the span of the second-order local regression smoothing filter used on the radius data so the dr/dt is also smooth can result in large differences in the flame speed depending on size of the smoothing span. Figure 6 provides an example of this effect with CH_4 , C_2H_4 [5], and C_2H_6 [5].

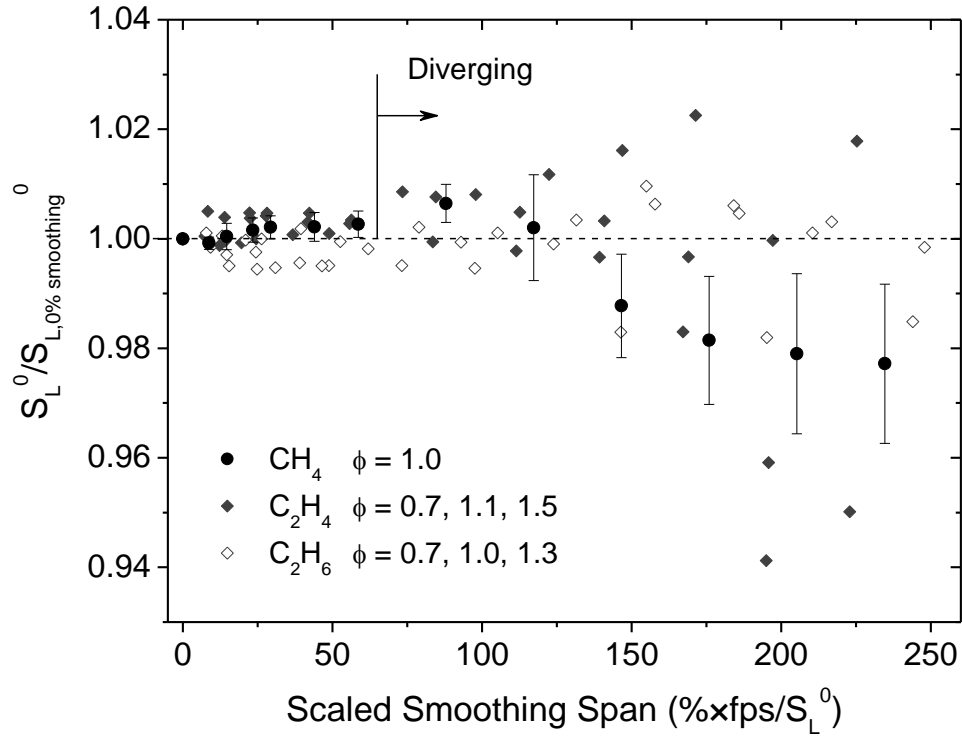


Figure 6. The effect of local 2nd-order polynomial smoothing on laminar flame speed data based on smoothing span % of data.

For these methane-air mixtures, the divergence in Figure 6 occurs when the smoothing spans greater than 20% of the data. This percentage is not universal because the smoothing amount depends on the data acquisition rate, FPS, and the flame speed. This plot should not be used as a guide but instead as a cautionary example to future researchers, and great care must be taken to not accidentally smooth away useful information. The difficulty of analysis lies in the coupling of the smoothing, numerical differentiation, and cutoff determination. These factors and their various interactions make determining the cutoffs very difficult and in many cases nothing more than a guess based on prior experience. To ensure that the laminar flame speed and Markstein lengths are not

arbitrarily biased, it is recommended that the final results be based on the unsmoothed data as described below.

As the resultant flame speed is quite sensitive to cutoff locations, a method in which both the dr/dt -versus-stretch plot and radius residuals are used. For reference, a sample dr/dt -versus-stretch plot is shown in Figure 7(a). In the present context, the cutoff locations refer to the lower (ignition-affected) and upper (confinement-affected) limits of the flame radius that delineate the region where useful flame speed measurements can be obtained. In the dr/dt plot from a given flame experiment, data that are ignition or confinement affected are not used. To identify these regions, the amount of smoothing is progressively increased, to identify the general trends, and then gradually decreased to zero smoothing while roughly positioning the cutoffs, which designate the ignition- and confinement-affected limits, at the ends of the healthy region. The cutoffs are then varied while looking at the residuals so that there are no leading or trailing disturbances and the data residuals are as normally and randomly distributed around zero as possible, to ensure that the model fit is as good as possible, although in practice the residuals usually take on a slight oscillatory pattern. Figure 7(a) shows an example of how the limits would be roughly defined by the Set cutoff and Used data.

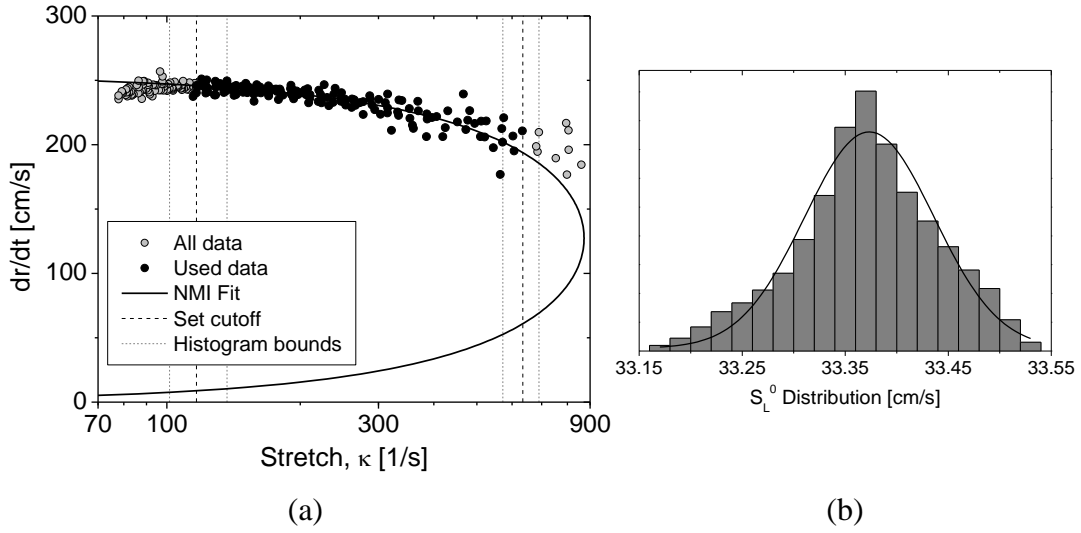


Figure 7. (a) Sample dr/dt -versus-stretch plot and (b) accompanying histogram of possible flame speed values within bounds (gray dashed lines) of CH_4/air mixture at $\phi = 1$, 1 atm, and 294.4 K.

An idea to solve the cutoff issue for both methods is to perturb their cutoff locations in areas that could be valid and create a histogram such that the mean or median value is the experimental flame speed, Figure 7(b). That is, while the areas where ignition and confinement effects are occurring can be easy to locate at their extremes, the areas where the flame speed begins to deviate from the model can be difficult to see and do affect the resultant flame speed.

In using either solution method, the quality of the radius edge detection is extremely important. Many literature sources, including earlier papers from the author's group, describe using a best-fit circle of some number of points on the detected edge, for example six. In the recent paper by Xiouris et al. [18], it was found that 16 to 32 points were the minimum required for the area error to converge. In this thesis, the semi-

automated MATLAB program is already detecting the entire perimeter of the flame edge so, in the interest of convenience and experimental accuracy, every pixel in the detected perimeter is used in the circle-fitting process. To exclude the electrode disturbance at small radii, which results in an artificial flame acceleration near the electrodes for the conditions of this study, the MATLAB code employs a method to remove electrode-disturbed areas based on the angle derived from the box that encompasses the detected flame edge. The angle is variable to properly remove electrode-disturbed areas as the flame propagates.

II.3 References

- [1] T. Sikes, M.S. Mannan, E.L. Petersen, An experimental study: Laminar flame speed sensitivity from spherical flames in stoichiometric CH₄-air mixtures, *Combust. Sci. Technol.* (2018) 1-20.
- [2] J. de Vries, W.B. Lowry, Z. Serinyel, H.J. Curran, E.L. Petersen, Laminar flame speed measurements of dimethyl ether in air at pressures up to 10 atm, *Fuel* 90 (2011) 331-338.
- [3] W. Lowry, J. de Vries, M. Krejci, E. Petersen, Z. Serinyel, W. Metcalfe, H. Curran, G. Bourque, Laminar flame speed measurements and modeling of pure alkanes and alkane blends at elevated pressures, *J. Eng. Gas. Turb. Power.* 133 (2011) 091501-091501.
- [4] M.C. Krejci, O. Mathieu, A.J. Vissotski, S. Ravi, T.G. Sikes, E.L. Petersen, A. Kérmonès, W. Metcalfe, H.J. Curran, Laminar flame speed and ignition delay time data for the kinetic modeling of hydrogen and syngas fuel blends, *J. Eng. Gas. Turb. Power.* 135 (2013) 021503-021503.
- [5] S. Ravi, T.G. Sikes, A. Morones, C.L. Keese, E.L. Petersen, Comparative study on the laminar flame speed enhancement of methane with ethane and ethylene addition, *Proc. Combust. Inst.* 35 (2015) 679-686.
- [6] T. Sikes, M.S. Mannan, E.L. Petersen, Laminar flame speeds of nano-aluminum/methane hybrid mixtures, *Combust. Flame* 166 (2016) 284-294.

- [7] G. Settles, *Schlieren and shadowgraph techniques: Visualizing phenomena in transparent media*, Springer Science & Business Media, 2001.
- [8] J. Canny, A computational approach to edge detection, *IEEE Trans. Pattern Anal. PAMI-8* (1986) 679-698.
- [9] M.D. Heath, S. Sarkar, T. Sanocki, K.W. Bowyer, A robust visual method for assessing the relative performance of edge-detection algorithms, *IEEE Trans. Pattern Anal.* 19 (1997) 1338-1359.
- [10] G. Taubin, Estimation of planar curves, surfaces, and nonplanar space curves defined by implicit equations with applications to edge and range image segmentation, *IEEE Trans. Pattern Anal.* 13 (1991) 1115-1138.
- [11] P. Clavin, Dynamic behavior of premixed flame fronts in laminar and turbulent flows, *Prog. Energy Combust. Sci.* 11 (1985) 1-59.
- [12] Z. Chen, On the extraction of laminar flame speed and Markstein length from outwardly propagating spherical flames, *Combust. Flame* 158 (2011) 291-300.
- [13] G.H. Markstein, Experimental and theoretical studies of flame-front stability, *J. Aeronaut. Sci.* 18 (1951) 199-209.
- [14] M.L. Frankel, G.I. Sivashinsky, On effects due to thermal expansion and Lewis number in spherical flame propagation, *Combust. Sci. Technol.* 31 (1983) 131-138.
- [15] A.P. Kelley, G. Jomaas, C.K. Law, Critical radius for sustained propagation of spark-ignited spherical flames, *Combust. Flame* 156 (2009) 1006-1013.
- [16] P.D. Ronney, G.I. Sivashinsky, A theoretical study of propagation and extinction of nonsteady spherical flame fronts, *SIAM J. Appl. Math.* 49 (1989) 1029-1046.
- [17] J.K. Bechtold, C. Cui, M. Matalon, The role of radiative losses in self-extinguishing and self-wrinkling flames, *Proc. Combust. Inst.* 30 (2005) 177-184.
- [18] C. Xiouris, T. Ye, J. Jayachandran, F.N. Egolfopoulos, Laminar flame speeds under engine-relevant conditions: Uncertainty quantification and minimization in spherically expanding flame experiments, *Combust. Flame* 163 (2016) 270-283.

CHAPTER III

LAMINAR FLAME SPEED MEASUREMENTS*

In these experiments, the HTHP laminar flame speed vessel was heated to 120 °C using the heating jacket shown in Figure 2. The temperature variation within the vessel was checked with an array of thermocouples, all of which agreed to within 1 °C. The fill and exhaust lines were also heated to 120 °C using heating tape to prevent condensation of the OPCs from occurring. The mixtures were prepared using the partial pressure method in order of ascending partial pressure. The liquid OPCs were injected directly into the vessel via syringe and its pressure measured using a heated 0-100 torr MKS manometer. In other words, the OPCs are tested in the gas phase. The normal gas-phase components were measured using a 0-1000 torr manometer.

In previous fire suppressant laminar flame speed experiments, it has been customary to add the fire suppressant to a parent mixture as a percentage of the total system pressure [2-4], thus for these experiments, equivalence ratio is based on the gas-phase components. That is to say, the OPCs were added as a percentage of the total pressure and treated as additives. The reasons that the OPCs were introduced in this manner (rather than studying them as the only fuel in a fuel-air mixture) were threefold: 1) to investigate the fire suppressing aspect of the OPCs; 2) the OPCs are very low vapor

* Part of this chapter is reprinted with permission from [1] T. Sikes, O. Mathieu, W. Kulatilaka, M.S. Mannan, E.L. Petersen, Laminar Flame Speeds of DEMP, DMMP, and TEP Added to H₂- and CH₄-Air Mixtures, Proc. Combust. Inst. (accepted) by Elsevier.

pressure making it difficult to vaporize higher levels of OPC; and 3) OPCs are known to have very low flame speeds and may not produce a self-sustaining flame in a spherically expanding flame experiment. Methane and hydrogen are both very well-studied fuels making them ideal candidates to investigate the effects of the OPCs on parent fuel/air mixtures.

Experiments were performed with the OPCs on both hydrogen/air and methane/air mixtures to study the relative effects of the OPCs on fuels of various carbon content. Such information will serve to further improve any kinetics models that use these measurements as these simple fuels are important even for more complicated fuels, which break down and then follow the simple fuels' kinetic path. These tests were particularly difficult because they required facility heating and because the OPCs left behind a residue that necessitated that the vessel be cleaned about every 10 experiments. This process was time consuming due to needing to cool down the vessel to near room temperature and heat it back up in each cleaning cycle. The residue was a brownish, somewhat sticky liquid that must have a very low vapor pressure because it did not evaporate even under extended vacuum. Many of these experiments are the first time laminar flame speed has been measured on the target OPCs. Markstein length plots and a table of all data obtained in this study are provided in the Appendix.

Radiation effects were taken into account using the Yu et al. [5] correlation, Eq. 3.1, to obtain a laminar flame speed value corrected for radiation:

$$S_{u,RC}^0 = S_L^0 + 0.82 S_L^0 \left(\frac{S_L^0}{1 [cm/s]} \right)^{-1.14} \left(\frac{T}{298 [K]} \right) \left(\frac{P}{1 [atm]} \right)^{-0.3} \quad (3.1)$$

In Eqn. 3.1, S_L^0 is the uncorrected laminar flame speed value extrapolated from either NM I or NM II, T is the initial temperature of the experiment, and P is the initial pressure. The difference that this correction makes was negligible but nevertheless has been included for the sake of completeness. This correction does not account for phosphorus species; however, it is expected that the uncertainty caused by radiation is within the conservative uncertainty estimates since only a small amount of an OPC is used in any given test.

Laminar flame speed model predictions were calculated using Cosilab. The general process was to first calculate the flame speed at $\phi = 1.0$ and to then use the profiles (such as species, temperature, velocity, heat release, etc.) as an initial guess to calculate a nearby equivalence ratio's laminar flame speed while allowing for a change in grid points so the software could converge to a result. To ensure that grid independence was indeed reached, the output profiles of the converged solution were used as an initial guess for a repeated calculation. This process was repeated in an iterative fashion to obtain the full curve of laminar flame speed versus equivalence ratio for a given mixture. To calculate the laminar flame speed at $\phi = 1.0$, a very rough initial guess was used with only a few number of grid points. The location of the points within the x domain was optimized and then additional points were added until grid convergence was obtained. After the location of points was optimized, the domain of x was increased to ensure that the first and last few points of the flame speed simulation showed no change in temperature, within 0.001 K.

For all points, this ΔT was checked before finishing a calculation. Another criterion was to inspect the heat release and velocity profiles to make sure that they are continuous and contained no other irregularities.

III.1 Methane

The laminar flame speeds were measured from $\phi = 0.8 - 1.3$ with OPCs being 0%, 0.1%, and 0.3% of the total mixture by volume. Note that the 0.3% DMMP was unable to be ignited at $\phi = 1.2$ (based on the methane-air mixture) and beyond. In general, the equivalence ratios were pushed to the limits of the experimental apparatus. The laminar flame speeds are shown in Figure 8. The data are not temperature corrected as there is no reliable mechanism to date. Typically, if a mechanism were available for all species, the calculated flame speed would be multiplied by the ratio of calculated flame speed at the correct temperature over the calculated flame speed at the actual temperature. This procedure corrects the flame speeds to be at a common temperature if the mechanism can closely replicate the temperature dependence. The radiation corrections increase these methane-based flame speeds by ~ 0.7 cm/s. The points in Figure 8 are experimental measurements, the solid line is a model, and the dashed lines are experimental fits. The experimental fits are meant to only aid the eye in understanding the general trend. The uncertainties are ± 1.75 cm/s.

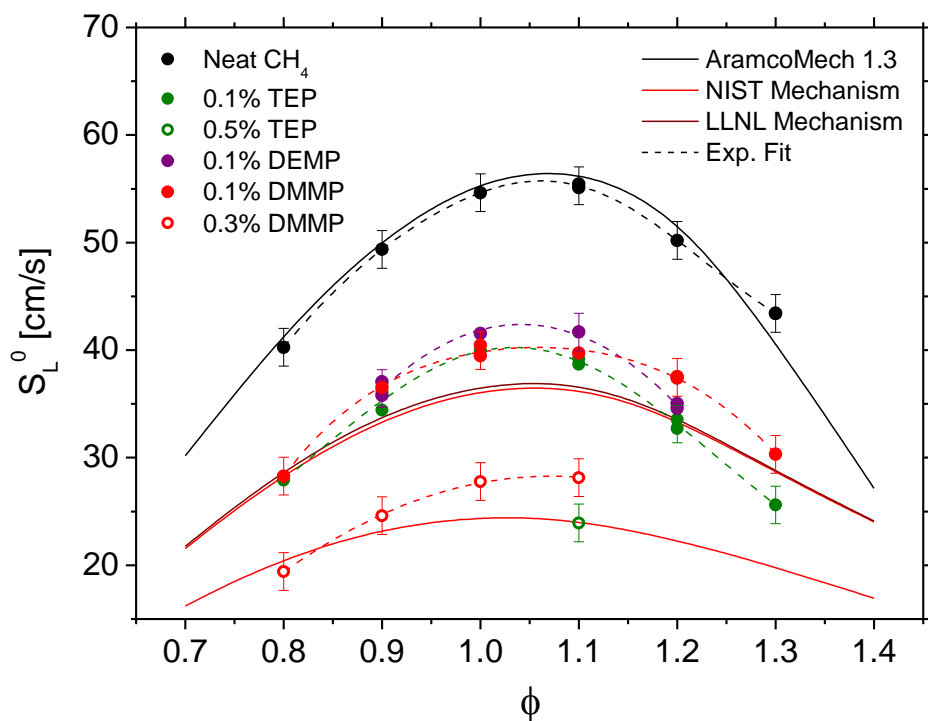


Figure 8. Laminar flame speeds of OPCs in methane/air mixtures at 1 atm, 120 °C.

In Figure 8, the laminar flame speed reductions caused to the methane/air mixture by 0.1% DMMP, DEMP, and TEP are all fairly similar, about 30%. The percent reduction tends to take a non-monotonic, parabolic shape with the least-effective reduction being near the peak. This trend near the peak has the effect of broadening the flame speed curve at lower and higher ϕ . The richest, neat methane point does lie above the model, but it is not uncommon to have a discrepancy from the model at rich conditions. The predictions of the NIST [6] and LLNL [7] mechanisms are nearly identical at 0.1% DMMP. They both predict a decrease in laminar flame speed that is fairly accurate at 0.1% DMMP, but there are some deficiencies as the model curves are broader than the experiments. At 0.3%

DMMP, the NIST model performs even worse at predicting the correct shape. The increased reduction in adding additional DMMP from 0%, 0.1%, and 0.3% (50% S_L^0 reduction) of the mixture shows a diminishing, non-linear effect. The addition of the OPCs also has the kinetic effect of pushing the peak flame speeds leaner than the neat mixtures. This shift is not an artifact of how the equivalence ratio is defined however, because even if it is taken into account, it shifts the curve by only about 0.01 for the small levels of OPC utilized herein. The repeatability is shown to be good, having a maximum deviation of 1 cm/s between points. The reduction seen in these experiments is not in disagreement with Babushok et al. [8] because the enhancement effect is not expected until ultra-lean mixtures ($\phi < 0.5$) and higher volume fractions of DMMP. Further testing in the ultra-lean region would be of interest but would be particularly difficult for a spherically expanding flame type experiment at these conditions. Unfortunately, for the other molecules in Figure 8, there are no mechanisms available in the literature.

There is however an existing model for DIMP. The DIMP model is from Glaude et al. [9], which is itself the mechanism on which both the NIST and LLNL models are built upon. In the subsequent models, DIMP reactions were removed in favor of improving DMMP and TMP reactions and reaction pathways. Both the model and the laminar flame speed measurements in the current study are given in Figure 9. For continuity with Figure 8, the TEP and neat methane data have been included as well.

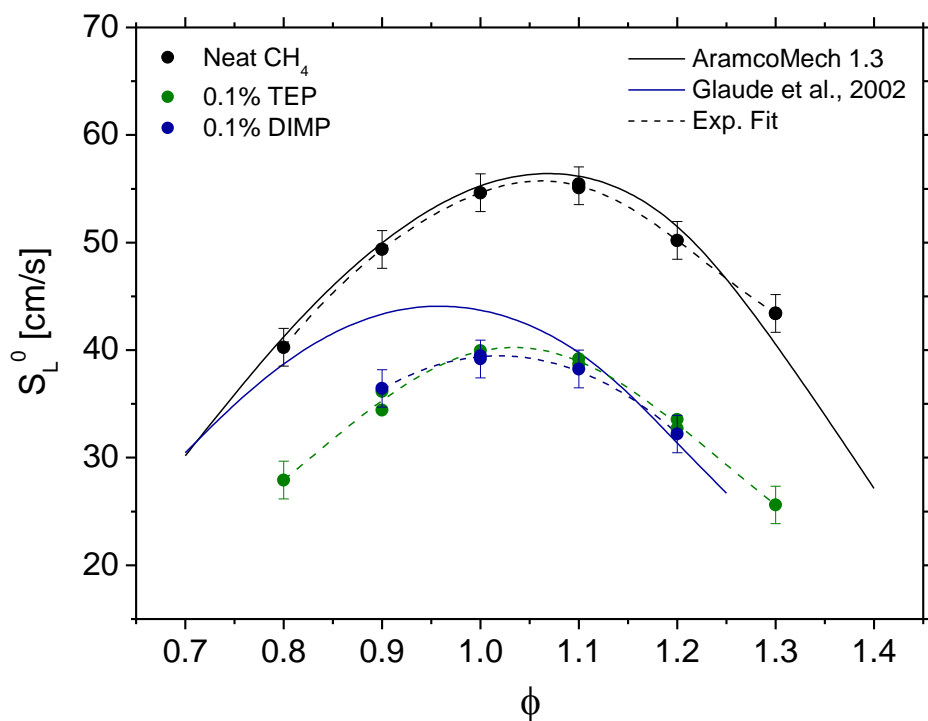


Figure 9. Laminar flame speeds of DIMP in methane/air mixtures at 1 atm, 120 °C. The DIMP model curve is calculated using the Glaude et al. [9] mechanism, which is the precursor to the LLNL model.

The DIMP data are very comparable to the TEP data. There is roughly a 30% decrease in flame speed compared to the neat methane flame speed. The shape that can be inferred from the DIMP data points is also quite similar to the neat methane curve. The Glaude et al. [9] model has some deficiencies in modeling both overpredicting the lean side laminar flame speed, ~5 cm/s too fast, and the entire curve is shifted to the left, ~0.6, compared to the data. However, the general shape is captured very well if the model prediction is superimposed onto the data. Again in this plot the uncertainties are stated to be ± 1.75 cm/s.

III.2 Hydrogen

The hydrogen experiments were performed from $\phi = 0.6 - 1.3$. All OPCs were measured to the limits of either not igniting on the rich side or becoming increasingly unstable on the lean side. The instability manifested itself as the rapid development of cellularity in the flame. Any images that exhibit such cellularity cannot be used to determine laminar flame speed, as they are no longer laminar. Figure 10 shows the laminar flame speeds with the various OPCs and concentrations. The uncertainties are stated to be 7 cm/s. The radiation corrections increase these hydrogen-based flame speeds by ~ 0.5 cm/s.

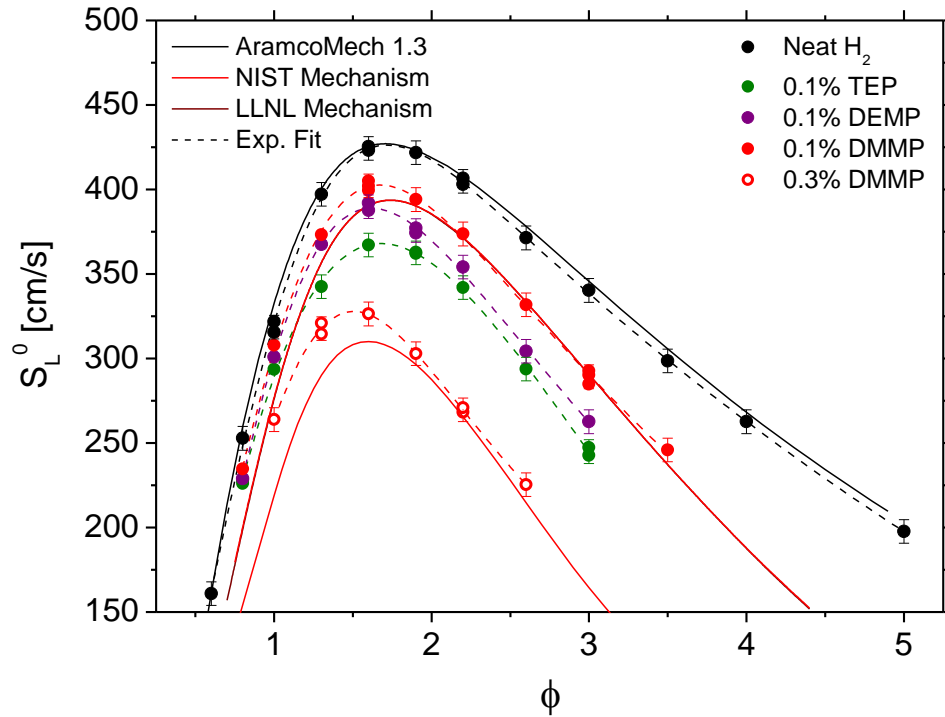


Figure 10. Laminar flame speeds of OPCs in hydrogen/air mixtures at 1 atm, 120 °C.

Unlike the OPC-doped laminar flame speeds for methane-air in Figure 8, there is a clear difference between TEP, DEMP, and DMMP in Figure 10 for the hydrogen-air mixtures. There is an increasing flame speed suppression effect that corresponds to the increasing complexity of the molecules, i.e., TEP (15% overall reduction) > DEMP (13%) > DMMP (9%). The predictions of the NIST and LLNL mechanisms are almost exactly the same. They both do a good job of describing the rich-side 0.1% DMMP effect, but they underpredict the peak and lean-side effects by ~5% and 15%, respectively. The NIST mechanism performs slightly worse at 0.3% DMMP. In general, the net effect of the OPCs is to decrease the flame speed, although unlike the methane/air results, in an increasingly effective manner. That is to say the flame speed reduction is larger on the rich side than on the lean side. This ϕ effect manifests itself in the graph by compressing the OPC curves along the equivalence ratio axis. The higher-concentration DMMP results display a linear increase in flame speed reduction when combined with the 0.1% and neat H₂/air flame speeds. The effects seen in the lower-concentration OPC results are shown to extend to the higher-concentration DMMP. The laminar flame speed values are further reduced and compressed.

DIMP has again been separated from the other OPCs in the interest of clarity. DIMP laminar flame speed is compared to TEP and neat hydrogen laminar flame speed values in Figure 11. The uncertainty is estimated to be ± 7 cm/s.

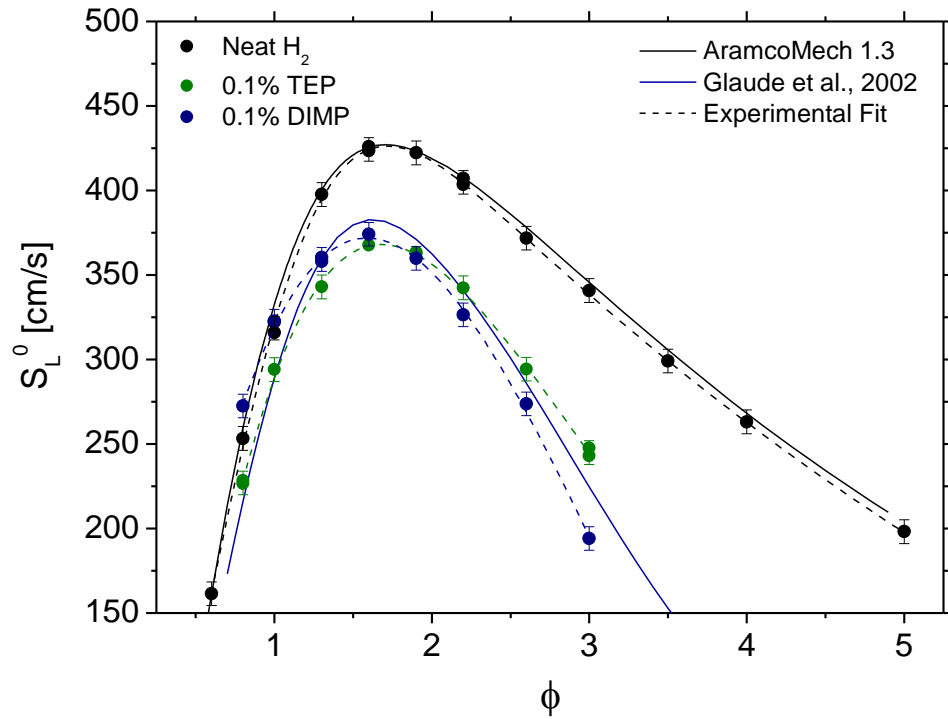


Figure 11. Laminar flame speeds of DIMP in hydrogen/air mixtures at 1 atm, 120 °C. The DIMP model curve is calculated using the Glaude et al. [9] mechanism.

DIMP-influenced flame speeds in Figure 11 are lower than the TEP-based results on the rich side but higher on the lean side. Unlike the methane plot in Figure 9, there is a clear difference between the two OPCs. As a whole, DIMP roughly reduces the flame speed by about 20%. The model does a good job of predicting the general shape of the experimental data, but there still are some deficiencies in capturing the DIMP/H₂ combustion behavior. On the lean side, the Glaude et al. [9] mechanism underpredicts the laminar flame speed compared to the experimental data. The mechanism shows that the laminar flame speed decrease to be approximately the same for DMMP, Figure 10, and

DIMP at fuel lean conditions, but the data do not support this conclusion. This lean side discrepancy is a critical area on which to improve future OPC models.

To be able to test future mechanisms in another manner, DIMP was used in a concentration study with a hydrogen/air mixture at $\phi = 1.6$, 1 atm, 120 °C. The results of this brief study are shown in Figure 12.

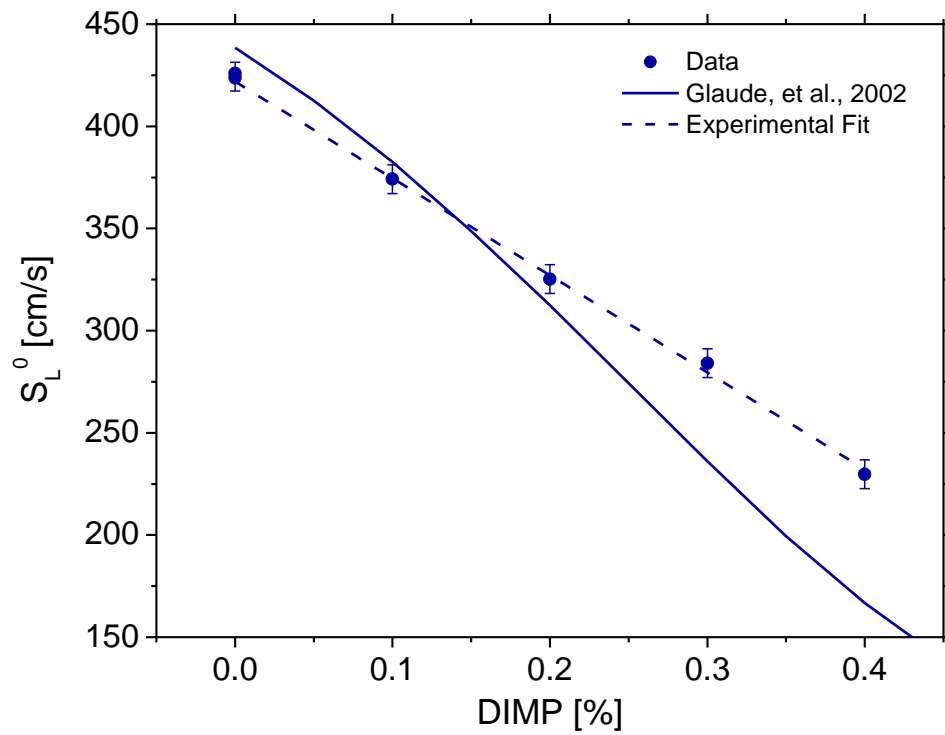


Figure 12. Laminar flame speeds of DIMP in hydrogen/air mixtures at $\phi = 1.6$, 1 atm, 120 °C. The DIMP model curve is calculated using the Glaude et al. [9] mechanism.

The amount of DIMP was varied from 0.0 – 0.4% in Figure 12. As with previous experiments, it is possible to increase the OPC concentration further than this, but difficulties arise with the amount of time it takes to run a set of experiments due to the

cleaning procedure necessary with these compounds. Nevertheless, with the given experiments it is already evident that there is a difference between the Glaude et al. [9] mechanism and the data obtained herein. Below $\sim 0.13\%$ DIMP the model overpredicts the experimental results by 13 cm/s (or 3%). This overprediction is actually not an issue with the OPC submechanism but is instead due to the outdated hydrocarbon base that the OPC submechanism is built upon. Hydrocarbon mechanisms are continuously being updated, with one of the latest being AramcoMech 2.0 [10-16]. As seen in Figure 10 and Figure 11, the newer AramcoMech 1.3 does an excellent job at modeling the neat laminar flame speed of hydrogen/air. Above $\sim 0.13\%$ DIMP, the model begins to underpredict the measured laminar flame speed and grows progressively worse as the equivalence ratio increases up to a maximum difference of 40% at 0.4% DIMP. This flame speed disagreement at varying amounts of DIMP is another key point in which a future model could improve upon for future applications, such as a fire suppressant.

III.3 Fire Suppressant Comparison

The organophosphorus compounds are quite effective at suppressing the overall reactivity as indicated by the decrease in laminar flame speed. In previous studies in the author's laboratory by Osorio et al. [2, 17], fire suppressants have been used as 1% of the mixture or more; however, in the present study the first experiment with 0.5% TEP/methane/air had a flame speed which was too low to even continue at that concentration since moving toward leaner or richer mixtures would not produce

sustainable flames. Instead, the concentration had to be further reduced to only 0.1% of the mixture. To qualitatively show the effectiveness of OPCs, Figure 13 shows a comparison between previous fire suppressants studied at TAMU and the current OPCs by temperature correcting the previous fire suppressants to 393 K.

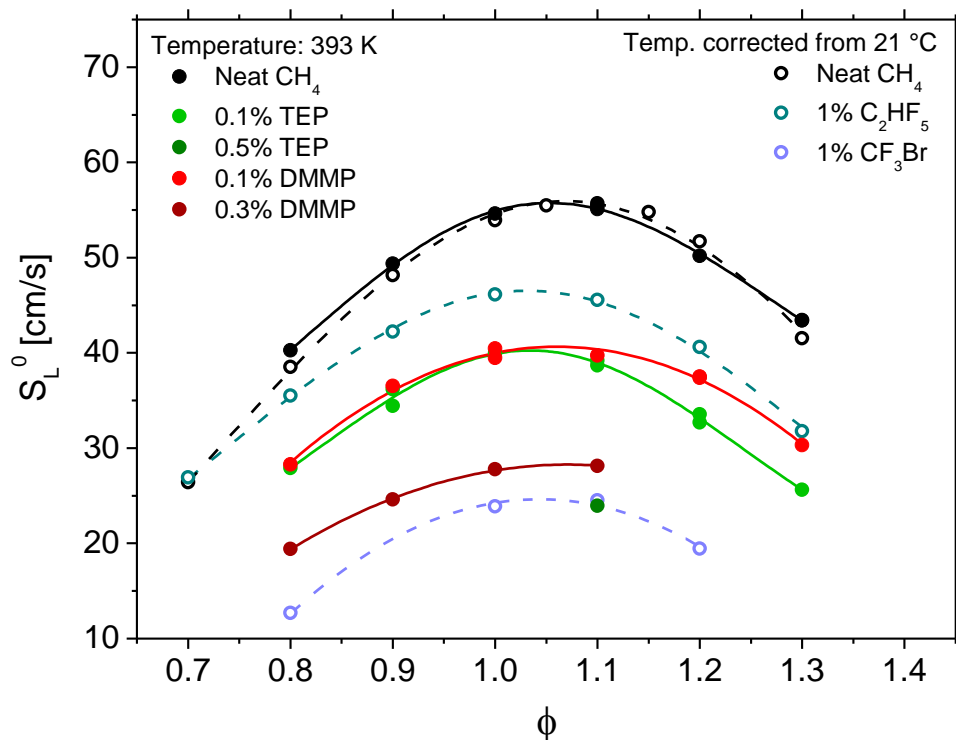


Figure 13. Qualitative comparison of fire suppressant effect of OPCs (1 atm, 120 °C) to more-established fire suppressants: Halon 1301 (CF_3Br) [2] and C_2HF_5 [17] (1 atm, 21 °C). The 21 °C data are temperature corrected to 393 K. Filled circles are the current data and the solid lines are their experimental fits. Open circles are previous fire suppressant studies at TAMU with dashed lines as their experimental fits.

Halon 1301 has historically been the golden standard for fire suppressants [18-20]. In Figure 13, the level of reduction by 1% Halon 1301 is matched by 0.5% TEP and nearly matched by 0.3% DMMP. The 0.1% OPCs in the current study are shown to be more

effective than C_2HF_5 by about 15%. While this difference in flame speed reduction is not a perfect comparison because of the initial temperature differences between these studies, it is nevertheless a demonstration on the powerful flame-suppression capabilities of these OPCs. Understanding the laminar flame speed reduction caused by these compounds requires investigating the chemical kinetics that govern their behavior.

III.4 Flame Speed Sensitivity Analysis

A flame speed sensitivity analysis has been performed to determine the reactions which are most important for laminar flame speed and could provide starting points for further improvement of the OPC mechanisms. The sensitivity analysis provides a method of determining how altering rate constants would affect flame speed and thus provides an estimate of the relative importance of each reaction for laminar flame speed. For comparison purposes, a flame speed sensitivity analysis of 0.1% DMMP/ CH_4 /air at 1 atm, 120 °C is summarized in Figure 14 for the reactions which contain phosphorus. The relative sensitivity is defined as $S_{S_L}^\alpha \equiv \frac{k_\alpha}{S_L} \frac{\partial S_L}{\partial k_\alpha}$. In this equation k_α is the rate constant of a given reaction, and S_L is the calculated laminar flame speed. This equation is normalized so that the sensitivities can be easily compared to one another.

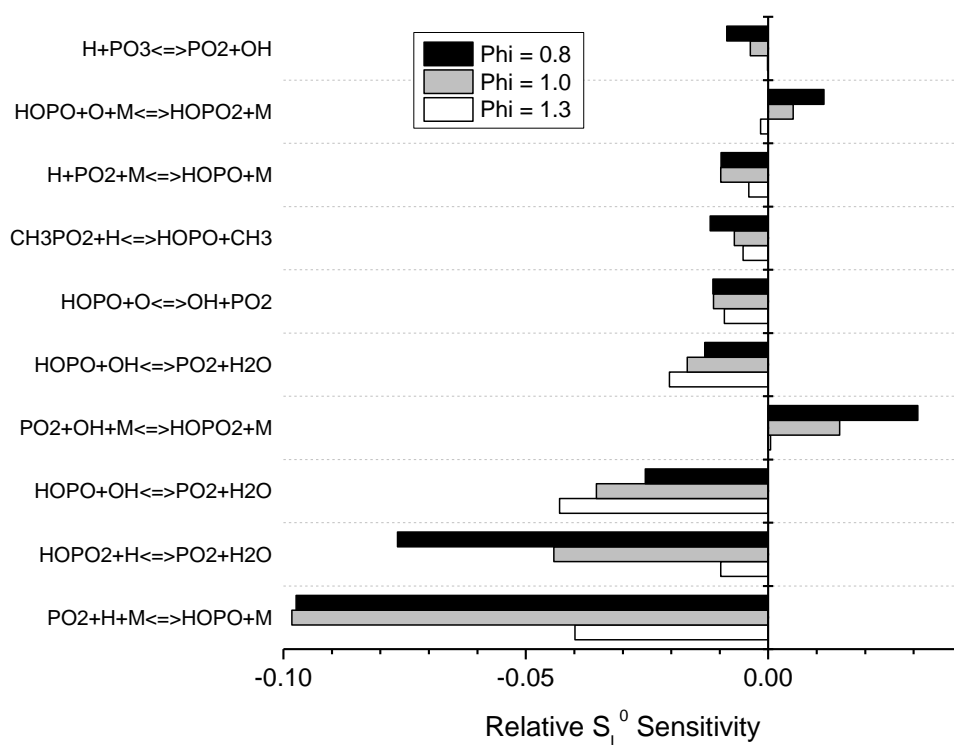


Figure 14. Top 10 OPC reactions containing phosphorous of 0.1% DMMP/CH₄/air relative laminar flame speed sensitivity at 1 atm, 120 °C.

Unsurprisingly, many of the top OPC reactions in Figure 14 match those of the primary inhibition mechanism as stated by Twarowski [21-23]. Almost all of the reactions that inhibit laminar flame speed involve either HOPO or HOPO₂ intermediates. The inhibition effect, as expected, seems to come from the radical recombination reactions that lead to PO₂.

To summarize the sensitivity plot provided here and in the Appendix, the top reactions in all sensitivity analyses have been restated in Table 1 in order of most important to least. Note that for the DMMP/CH₄ data there are only eight reactions because there are two duplicate reactions in the sensitivity analysis.

Table 1. Top reactions ranked from most important to least (1 – 10) for each set of sensitivity analyses performed.

Reaction Number	Reaction	DMMP NIST Mech.		DIMP Glaude 2002	
		CH ₄	H ₂	CH ₄	H ₂
(R1)	PO ₂ + H + M ⇌ HOPO + M	1	5	1	
(R3)	HOPO + OH ⇌ H ₂ O + PO ₂	3	9	2	9
	POMe[Ome] ₂ + H ⇌ POMe[Ome][OCH ₂] + H ₂		1		
(R5)	HOPO ₂ + H ⇌ H ₂ O + PO ₂	2	4		
(R2)	HOPO + H ⇌ H ₂ + PO ₂		7	3	1
	POMe[Ome][OCH ₂] ⇌ POMe[Ome] + CH ₂ O		2		
	HOPO ₂ + H ⇌ PO[OH] ₂			4	2
	POMe[Ome][OCH ₂] + H ⇌ POMe[Ome] ₂		3		
(R4)	PO ₂ + OH + M ⇌ HOPO ₂ + M	4		5	
	HOPO + O ⇌ OH + PO ₂	5	6	6	
	HOPO + O + M ⇌ HOPO ₂ + M	7	8	9	5
	POMe[OiPr] ₂ + H ⇌ POMeOiPr[OPC ₃ H ₆] + H ₂				3
	POMe[OiPr] ₂ + H ⇌ POMeOiPr[OtC ₃ H ₆] + H ₂				4
	HOPO + OH ⇌ PO[OH] ₂			7	
	POMe[Ome] ₂ + OH ⇌ POMe[Ome][OCH ₂] + H ₂ O		10		
	POMe[OiPr] ₂ + OH ⇌ POMeOiPr[OPC ₃ H ₆] + H ₂ O				6
	PO[OH]me[OiPr] ⇌ CH ₃ PO ₂ + iC ₃ H ₇ OH				7
	CH ₃ PO ₂ + H ⇌ HOPO + CH ₃	6			
	CH ₃ PO ₂ + H ⇌ PO[OH]me				8
	POMe[OiPr] ₂ + OH ⇌ POMeOiPr[OtC ₃ H ₆] + H ₂ O				10
	PO ₂ + H + M ⇌ HPO ₂ + M			8	
	PO ₃ + H ⇌ PO ₂ + OH	8			
	PO ₂ + OH ⇌ H + PO ₃			10	

A similar trend to the reactions in Figure 14 is found for 0.1% DMMP/H₂/air with the notable exceptions that it includes DMMP initiation reactions and generation of formaldehyde from a closely related DMMP intermediate species. Both of these trends extend to the DIMP sensitivity analyses. The DIMP/CH₄ laminar flame speed is highly

sensitive to reactions involving PO_2 , HOPO , and HOPO_2 . In the above table, PO_2 shows up 9 times and is involved in the number 1 ranked reaction twice ($\text{PO}_2 + \text{H} + \text{M} \rightleftharpoons \text{HOPO} + \text{M}$). In the future, detecting this species, without disturbing the combustion process, would go a long way toward experimentally testing the existing OPC mechanisms. The DIMP/ H_2 laminar flame speeds are influenced by the DIMP initiation reactions within the first few steps of the DIMP breakdown. The key reactions for the methane parent fuel cases seem to primarily be basic phosphorus oxidation reactions and would be the foundation for any OPC kinetics mechanism. The breakdown of the OPC compounds themselves are the driving factor for the laminar flame speeds that are based in a hydrogen fuel. Thus to improve an OPC chemical kinetics mechanism, these reactions should be focused on and their error minimized.

III.5 References

- [1] T. Sikes, O. Mathieu, W. Kulatilaka, M.S. Mannan, E.L. Petersen, Laminar Flame Speeds of DEMP, DMMP, and TEP Added to H_2 - and CH_4 -Air Mixtures, *Proc. Combust. Inst.* (accepted).
- [2] C.H. Osorio, A.J. Vissotski, E.L. Petersen, M.S. Mannan, Effect of CF_3Br on C1–C3 ignition and laminar flame speed: Numerical and experimental evaluation, *Combust. Flame* 160 (2013) 1044-1059.
- [3] O. Mathieu, C. Keese, C. Gregoire, E.L. Petersen, Experimental and chemical kinetics study of the effects of Halon 1211 (CF_2BrCl) on the laminar flame speed and ignition of light hydrocarbons, *J. Phys. Chem. A* 119 (2015) 7611-7626.
- [4] O. Mathieu, J. Goulier, F. Gourmel, M.S. Mannan, N. Chaumeix, E.L. Petersen, Experimental study of the effect of CF_3I addition on the ignition delay time and laminar flame speed of methane, ethylene, and propane, *Proc. Combust. Inst.* 35 (2015) 2731-2739.

- [5] H. Yu, W. Han, J. Santner, X. Gou, C.H. Sohn, Y. Ju, Z. Chen, Radiation-induced uncertainty in laminar flame speed measured from propagating spherical flames, *Combust. Flame* 161 (2014) 2815-2824.
- [6] O.P. Korobeinichev, V.M. Shvartsberg, A.G. Shmakov, The chemistry of combustion of organophosphorus compounds, *Russ. Chem. Rev.* 76 (2007) 1094.
- [7] T.M. Jayaweera, C.F. Melius, W.J. Pitz, C.K. Westbrook, O.P. Korobeinichev, V.M. Shvartsberg, A.G. Shmakov, I.V. Rybitskaya, H.J. Curran, Flame inhibition by phosphorus-containing compounds over a range of equivalence ratios, *Combust. Flame* 140 (2005) 103-115.
- [8] V.I. Babushok, G.T. Linteris, V.R. Katta, F. Takahashi, Influence of hydrocarbon moiety of DMMP on flame propagation in lean mixtures, *Combust. Flame* 171 (2016) 168-172.
- [9] P.A. Glaude, C. Melius, W.J. Pitz, C.K. Westbrook, Detailed chemical kinetic reaction mechanisms for incineration of organophosphorus and fluoroorganophosphorus compounds, *Proc. Combust. Inst.* 29 (2002) 2469-2476.
- [10] A. K  romn  s, W.K. Metcalfe, K.A. Heufer, N. Donohoe, A.K. Das, C.-J. Sung, J. Herzler, C. Naumann, P. Griebel, O. Mathieu, M.C. Krejci, E.L. Petersen, W.J. Pitz, H.J. Curran, An experimental and detailed chemical kinetic modeling study of hydrogen and syngas mixture oxidation at elevated pressures, *Combust. Flame* 160 (2013) 995-1011.
- [11] W.K. Metcalfe, S.M. Burke, S.S. Ahmed, H.J. Curran, A hierarchical and comparative kinetic modeling study of C1 – C2 hydrocarbon and oxygenated fuels, *Int. J. Chem. Kinet.* 45 (2013) 638-675.
- [12] S.M. Burke, W. Metcalfe, O. Herbinet, F. Battin-Leclerc, F.M. Haas, J. Santner, F.L. Dryer, H.J. Curran, An experimental and modeling study of propene oxidation. Part 1: Speciation measurements in jet-stirred and flow reactors, *Combust. Flame* 161 (2014) 2765-2784.
- [13] S.M. Burke, U. Burke, R. Mc Donagh, O. Mathieu, I. Osorio, C. Keesee, A. Morones, E.L. Petersen, W. Wang, T.A. DeVerter, M.A. Oehlschlaeger, B. Rhodes, R.K. Hanson, D.F. Davidson, B.W. Weber, C.-J. Sung, J. Santner, Y. Ju, F.M. Haas, F.L. Dryer, E.N. Volkov, E.J.K. Nilsson, A.A. Konnov, M. Alrefae, F. Khaled, A. Farooq, P. Dirrenberger, P.-A. Glaude, F. Battin-Leclerc, H.J. Curran, An experimental and modeling study of propene oxidation. Part 2: Ignition delay time and flame speed measurements, *Combust. Flame* 162 (2015) 296-314.

- [14] U. Burke, W.K. Metcalfe, S.M. Burke, K.A. Heufer, P. Dagaut, H.J. Curran, A detailed chemical kinetic modeling, ignition delay time and jet-stirred reactor study of methanol oxidation, *Combust. Flame* 165 (2016) 125-136.
- [15] C.-W. Zhou, Y. Li, E. O'Connor, K.P. Somers, S. Thion, C. Keese, O. Mathieu, E.L. Petersen, T.A. DeVerter, M.A. Oehlschlaeger, G. Kukkadapu, C.-J. Sung, M. Alrefae, F. Khaled, A. Farooq, P. Dirrenberger, P.-A. Glaude, F. Battin-Leclerc, J. Santner, Y. Ju, T. Held, F.M. Haas, F.L. Dryer, H.J. Curran, A comprehensive experimental and modeling study of isobutene oxidation, *Combust. Flame* 167 (2016) 353-379.
- [16] Y. Li, C.-W. Zhou, K.P. Somers, K. Zhang, H.J. Curran, The oxidation of 2-butene: A high pressure ignition delay, kinetic modeling study and reactivity comparison with isobutene and 1-butene, *Proc. Combust. Inst.* 36 (2017) 403-411.
- [17] C. Osorio, A. Morones, J.W. Hargis, E.L. Petersen, M.S. Mannan, Effect of C₂H₅F and C₃H₇F on methane and propane ignition and laminar flame speed: Experimental and numerical evaluation, *J. Loss Prevent. Proc.* 48 (2017) 21-31.
- [18] C.L. Ford, An Overview of Halon 1301 Systems in: *Halogenated Fire Suppressants*, American Chemical Society, 1975, Vol. 16, pp. 1-63.
- [19] R.S. Sheinson, J.E. Penner-Hahn, D. Indritz, The physical and chemical action of fire suppressants, *Fire Saf. J.* 15 (1989) 437-450.
- [20] M.R. Nyden, G.T. Linteris, D.R. Burgess Jr, P.R. Westmoreland, W. Tsang, M.R. Zachariah, Flame inhibition chemistry and the search for additional fire fighting chemicals (NIST SP 861), 1994, 1-9.
- [21] A. Twarowski, The influence of phosphorus oxides and acids on the rate of H + OH recombination, *Combust. Flame* 94 (1993) 91-107.
- [22] A. Twarowski, Photometric determination of the rate of H₂O formation from H and OH in the presence of phosphine combustion products, *Combust. Flame* 94 (1993) 341-348.
- [23] A. Twarowski, Reduction of a phosphorus oxide and acid reaction set, *Combust. Flame* 102 (1995) 41-54.

CHAPTER IV

IGNITION DELAY TIME MEASUREMENTS

A shock tube provides a nearly ideal experiment in which high-temperature and high-pressure combustion chemistry can be studied. Pressure and temperature ranges can vary widely among facilities but are within 0.1 – 1000 atm and 700 – 3000 K. There have been extensive studies that take advantage of shock tubes dating back to the invention of shock tubes in 1899 [1, 2]. A generic shock tube is based on compressible fluid dynamics and can be seen in Figure 15.

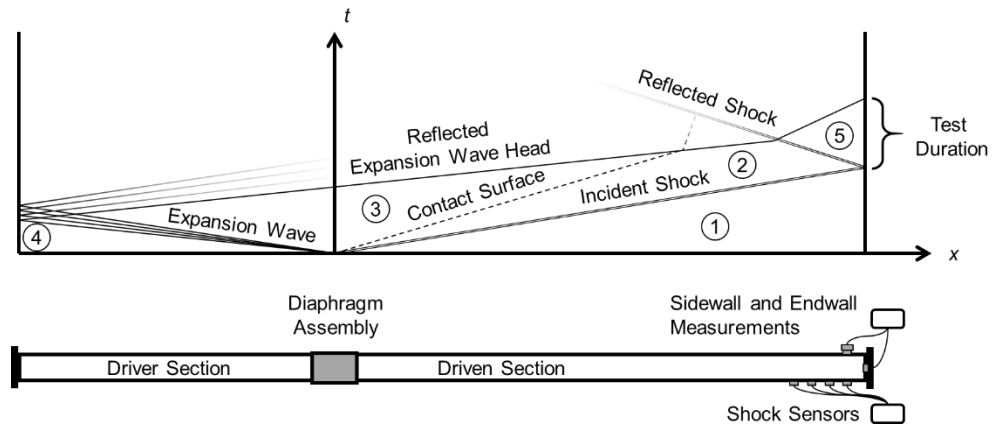


Figure 15. Shock-tube schematic and x-t diagram.

The concept of a shock tube is to separate two regions of gas: the driver gas, region 4, and the driven gas, region 1 in Figure 15. Region 4 contains a highly pressurized volume of gas compared to the lower pressure gas in region 1. Typical gases used are helium,

argon, and nitrogen. The choice of driver gas strongly affects the shock because the governing equations are a function of specific heat ratios and molecular weights. Changing the driver gas is called tailoring and is done in some combustion experiments to extend testing time. Region 1 contains the lower pressure gas that is meant to be shocked to higher pressure and temperature. These sections are initially separated by a diaphragm.

Upon breaking of the diaphragm, an expansion wave travels through region 4, and pressure waves coalesce into a shock wave that travels through region 1. The shock wave increases the temperature and pressure of region 1 instantaneously compared to the order of time in which chemical reactions take place. Behind this shock wave is region 2; however, while this region has been shocked to higher temperature and pressure, it has also been given a forward velocity in the direction of the shockwave. Upon hitting the endwall, the shock wave reflects and travels back down the shock tube. Travelling back down the tube again double shocks the gas, creating region 5, but it also cancels out the previously induced velocity. This process allows researchers a repeatable and controlled method of increasing temperature and pressure to study chemical reactions.

The test time to study chemical reactions is limited by either the time it takes the contact surface, wave reflections from the contact surface, or the main expansion waves to reach region 5. When the contact surface interacts with the reflected shock, then a rarefaction wave and pressure/shock wave may be formed, similar to breaking a diaphragm. These phenomena can cause changes in region 5 conditions (temperature, pressure, composition) that signify the end of an experiment. The equations that describe such an experiment are given as a simplified system of equations in Eqn. 4.1.

$$\begin{bmatrix} \frac{P_2}{P_1} + \frac{u_1^2}{RT_1} \left(\frac{T_2}{P_2} \frac{P_1}{T_1} - 1 \right) - 1 \\ \frac{(h_2 - h_1)}{u_1^2/2} + \left(\frac{T_2}{P_2} \frac{P_1}{T_1} \right)^2 - 1 \\ \frac{P_5}{P_2} + \frac{u_1^2}{RT_1} \left(\frac{T_2}{P_2} \frac{P_1}{T_1} - 1 \right) \left(\frac{P_5}{P_2} \right) \left(\frac{P_1 T_2 - P_2 T_1}{P_2 T_5 - P_5 T_2} \right) - 1 \\ \frac{(h_5 - h_2)}{\frac{u_1^2}{2} \left(\frac{T_2}{P_2} \frac{P_1}{T_1} - 1 \right)^2} + \left(\frac{T_5}{P_5} + \frac{T_2}{P_2} \right) \left(\frac{P_5}{T_5} - \frac{P_2}{T_2} \right) \end{bmatrix} = \begin{bmatrix} 0 \\ 0 \\ 0 \\ 0 \end{bmatrix} \quad (4.1)$$

In Eqn. 4.1, P is pressure, T is temperature, R the specific universal gas constant, and h the enthalpy. The subscripts of the aforementioned variables represent their respective regions. Additionally, u_1 is the incident shock speed (typically measured with timers). The equations from top to bottom are the conservation of momentum (MoM) and conservation of energy (CoE) of the incident shock, followed by the MoM and CoE of the reflected shock. This system of equations is structured in a way that could numerically be solved with the unknown variables being T_2, P_2, T_5 , and P_5 [3].

IV.1 Experimental Facility and Procedure

In the current study, the glass shock tube at ICARE – CNRS was utilized to investigate the OPCs dimethyl phosphite (DMP), diethyl phosphite (DEP), and trimethyl phosphate (TMP) and their effects on hydrogen and ethylene [4, 5]. The glass shock tube has a 2-m long, \varnothing 50-mm stainless steel driver section and a 9-m long, \varnothing 50-mm unheated Pyrex driven section. The primary advantage of a Pyrex driven section is that glass adsorbs and outgases less than steel. This lower rate of adsorption means that the test mixture will

be more certain. A marginal benefit is that the pyrex is smoother than steel which may slightly increase potential testing times due to lower wall friction. Another benefit with this shock tube is that it uses a piston-driven cutter to break the diaphragm which allows P_4 to be precisely controlled for repeatable reflected-shock conditions.

The measurement devices include four CHIMIE METAL A25L05B shock sensors spaced 150 mm apart to determine the shock wave velocity. These sensors are extremely responsive due to having a sensor diameter of 1 mm; however, they also are extremely susceptible to drift caused by heat transfer, making them suitable only as shock timers. The error introduced by these sensors on the incident shock velocity is 1% and subsequently the error propagated to T_5 and P_5 is 1% and 1.5%, respectively. A standard timer plot is shown in Figure 16. With the shock velocity known, post-shock conditions could be obtained through solving Eq. 4.1 in conjunction with known thermochemistry of the mixture species.

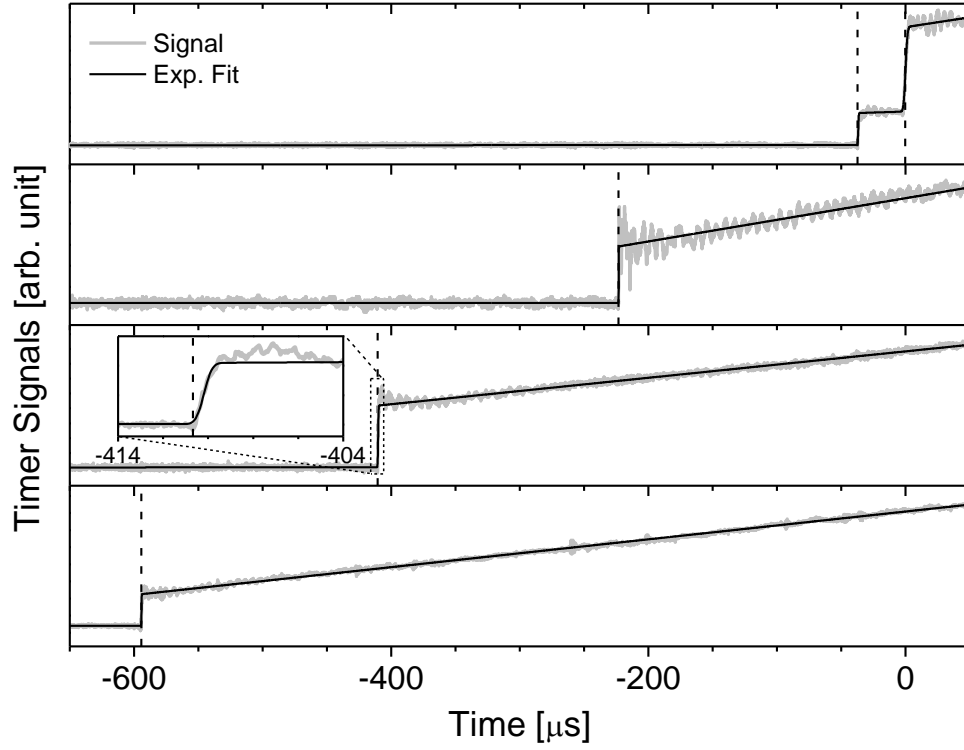


Figure 16. Characteristic timer signals in the glass shock tube. Timers are spaced by 150 mm and are numbered 1 – 4 from bottom to top.

In Figure 16, the raw signals are shown in blue and a fit to the pressure signals is shown in black. Note that the slope after the shock wave is not indicative of the real dP/dt in the bulk gas mixture but is instead due to heat transfer effects with the sensor itself, as mentioned previously. These signals are only used to determine the shock speed. The fits used are least squares fit equations of the general form shown in Eq. 4.2.

$$(1 - \Phi_{\mu_1, \sigma_1^2})g_1(t) + \left(\sum_{k=2}^n (1 - \Phi_{\mu_n, \sigma_n^2}) (\Phi_{\mu_{n-1}, \sigma_{n-1}^2}) g_n(t) \right) + \Phi_{\mu_n, \sigma_n^2} g_n(t) \quad (4.2)$$

Here, Φ_{μ,σ^2} is the normal cumulative distribution function (CDF), although any logistic function that can be made to vary between 0 – 1 would suffice, and $g(t)$ are additional fit functions. Essentially, the CDF acts as a switch between n number of piecewise functions. μ and σ^2 are included in the optimized variable list along with any variables in the piecewise functions. In this way, the switch between functions is continuous, as is its derivative, while maintaining the ability to capture the near discrete nature of shock waves. The first three timers are fit with two linear functions, and the fourth timer is fit with three linear functions. This fitting eliminates any noise in the signal and allows for an accurate determination of the time that the shock wave passes to within uncertainty of the fit. For the purposes of this study, the shock wave is said to be at the timer location when the fit signal has increased 5% above the baseline compared to the post-shock signal. Performing the calculation in this way makes the shock time determination procedure independent of the magnitude of the signal.

The shock wave velocity is calculated with a 2nd-order polynomial through the four timers. A 2nd order polynomial is necessary to account for the attenuation of the shock wave. Attenuation is defined as the normalized slope of velocity extrapolated to the endwall [6]. The attenuation in this study is typically on the order of 3 – 4.5% per meter. The representative plots that depict this process are shown in Figure 17. Figure 17(left) shows characteristic timer data that are fit with a 2nd-order polynomial to determine the velocity. The velocity can then be plotted versus distance and extrapolated to the endwall, Figure 17(right).

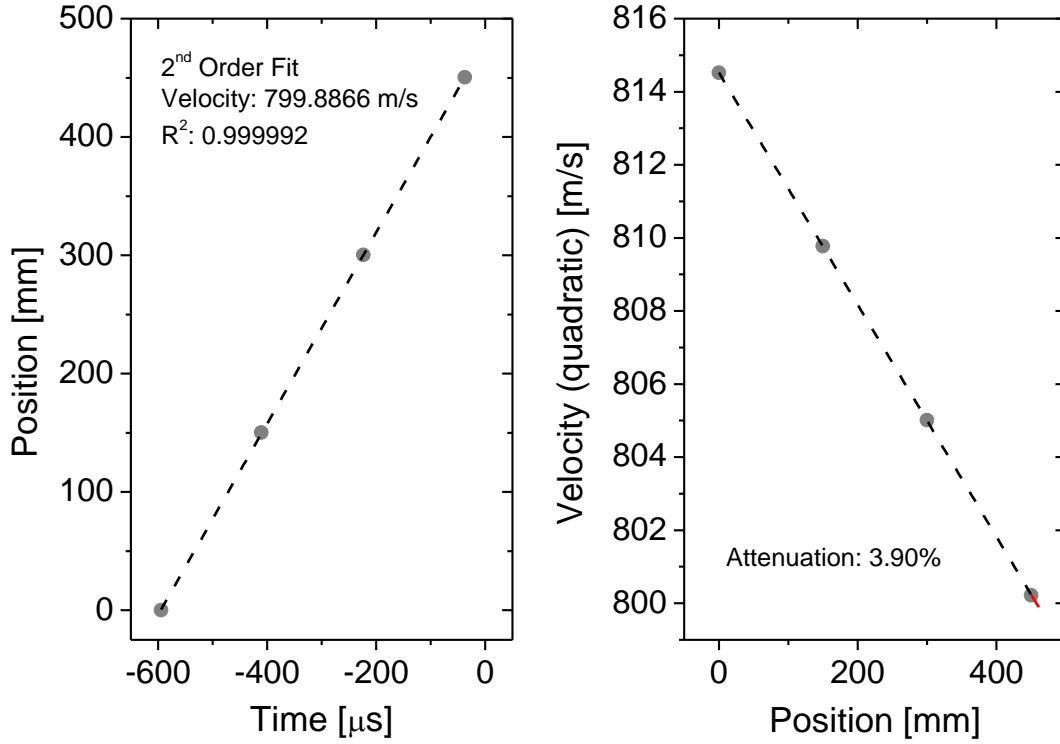


Figure 17. Representative velocity fitting (left) and attenuation (right) plot based on timer data from Figure 16. The dashed lines are experimental fits and the red line is the fit extrapolated to the endwall.

With these quantities known, the attenuation is determined by $\frac{-1}{u_{1,endwall}} \frac{du_1}{dx}$.

Alternatively, assuming a fit of the form $x = at^2 + bt + c$ for the shock timers, where a , b , and c are fit constants, the attenuation can be written as Eq. 4.3. To match the previous definition of attenuation (extrapolated to the endwall), x must be the distance from the first timer to the endwall.

$$-\frac{d \ln \dot{x}}{dx} = \frac{-2a}{\sqrt{4a(x-c) + b^2}} \quad (4.3)$$

Accurate endwall pressure is measured with a PCB 102A06 mounted flush on the endwall with a layer of RTV silicone to help mitigate heat transfer. To obtain ignition delay time, a 306 nm bandpass filter and a HAMAMATSU R928 photomultiplier are used to measure OH* emission profiles at a sidewall location 10.7 mm from the endwall (aligned with the fourth timer). For the purposes of this study, the ignition delay time is defined as the steepest slope of the OH* emission profile extrapolated backwards to the intersection with the zero minus the time at which the reflected shock reaches the fourth timer. The ignition delay time uncertainty is around 8% derived from the uncertainty of the steepest slope. A simultaneous CH* diagnostic is performed with a second photomultiplier and 431-nm bandpass filter. The CH* diagnostics were used to verify ignition measurements based on the OH* profiles. An example of the endwall and sidewall signals is shown in Figure 18.

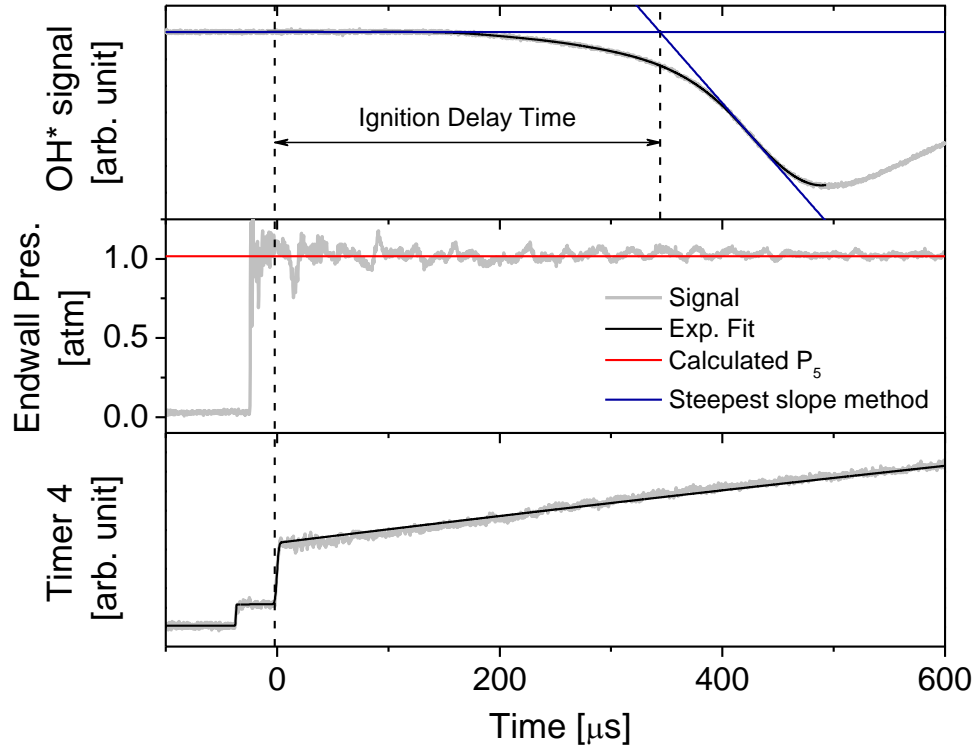


Figure 18. Sample signals from shock-tube experiments. From top to bottom: OH* emission profile, endwall pressure, and timer 4 signal. P_5 is calculated from normal shock relations, Eq. 1.

Figure 18 shows an example of an endwall pressure trace obtained in this study. There is a long-term pressure rise; however, in the experimental timespan, about 350 μs in this case, there is almost no pressure rise. This minimal pressure rise was the case for all experiments performed herein. As a check, calculated P_5 's are often plotted with the endwall pressure profiles, and they should fall on top of the pressure profiles, as they do here. In the other two plots in Figure 18, the OH* profile and timer 4 signals are shown. The fit on timer 4 is unimportant after the reflected shock and is only needed to find a reference time to base the ignition delay on. A Savitzky–Golay filter is applied to the OH* profile to more easily obtain the tangent line to the steepest slope. The window applied to

the signal is variable and must be carefully chosen to properly smooth out noise without smoothing any real features. The entire signal processing procedure has been simplified into a semi-automated Python program that takes mere minutes to fully analyze an experiment.

IV.2 Mixtures and Preparation

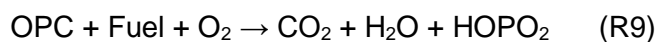
All mixtures were prepared in ~11-L glass bulbs to mitigate the potential of any surface reactions that could alter the composition of the prepared mixtures. They were also constantly stirred with a magnetically coupled stirring rod contained within the bulbs. This stirring kept all mixtures homogenous and well-mixed throughout the experimental process. The mixtures were initially created using the partial pressure method. A 0 – 10 torr MKS 122 BA manometer was used for the OPC, fuel, and oxygen, while a 0 – 1000 torr MKS 122 BA manometer was used to dilute the mixture with argon up to 500 torr (in most cases). The uncertainties on the two MKS manometers were 0.5% of the reading. Once made, the mixtures were allowed to mix for at least 30 minutes before testing. Helium was used as the driver gas and measured to an accuracy of 0.25 bar. The driven section was measured using a 0 – 1000 torr Edwards 600 AB manometer with an uncertainty of 0.15%. Prior to beginning experiments, all manometers were recalibrated.

The OPCs of interest for this study were DMP, DEP, and TMP. These are some of the simpler organophosphorus compounds that are still liquid at room temperature and thus are expected to have a reasonable vapor pressure with which to study gas phase kinetics. In the same fashion as the laminar flame speed experiments, the interest was not

only the OPCs, but also how they interact with hydrocarbons during combustion. The two primary fuels chosen were hydrogen and ethylene. Both of these fuels are well-studied and their chemical kinetics are relatively well-known. Argon (99.9999%), hydrogen (99.9999%), oxygen (99.9995%), and ethylene (>99.5%) were purchased from AIR LIQUIDE. All three OPCs were purchased from Sigma-Aldrich. The DMP and DEP were 98% purity and the TMP was >99% purity.

To ensure purity of the OPCs vapor, they were repeatedly degassed through vacuuming the test vials repeatedly until their vapor pressure remained constant. Initially, they were going to be degassed using liquid nitrogen, but the first vial on which this procedure was performed shattered. Other complications were the corrosive nature of DMP and DEP. The safety data sheet warned that DEP was corrosive to metal and could be a possible reason for a small shift, 0.004 torr, in manometer calibration during the study. DMP was more difficult to deal with because it dissolved the silicone O-ring used to seal the vial in which it was contained.

During mixture preparation, the lines were flushed three times, from 10 torr down to 10 mtorr or less, to dilute any previous residual vapor to a minimum. The equivalence ratios for these experiments were based on R9.



Between experiments, argon was introduced into the shock tube and then vented out. In this way, extra precaution could be taken to minimize any additional oxygen

introduced to the test mixture. This procedure also allowed for a rapid rate of experiments, approximately three shocks per hour at best.

IV.3 OPC Ignition Delay Times in Hydrogen Mixtures

As these experiments were meant to supplement similar experiments performed at TAMU on other larger OPCs (DMMP [7], DEMP (under review), DIMP (unpublished), and TEP [8]), it was important to show that the same level of uncertainty and general trends could be attained at ICARE – CNRS. To this end, a comparison set was performed with hydrogen/oxygen diluted in 98% argon to compare against previous data from Krejci et al. [9] and Kéromnès et al. [10]. The results from these experiments can be seen in Figure 19.

To generate the model curves, the closed, homogeneous reactor in Chemkin-Pro was used under constant volume and energy constraints. The time was set to run sufficiently long, typically on the order of milliseconds, with a time step set to 1 μ s or less. This time resolution allowed the output OH* profiles to be used in the same manner as experimental OH* profiles. As with the experimental profiles, the simulation profiles' ignition delay times were obtained through extrapolating the steepest slope of OH* to zero.

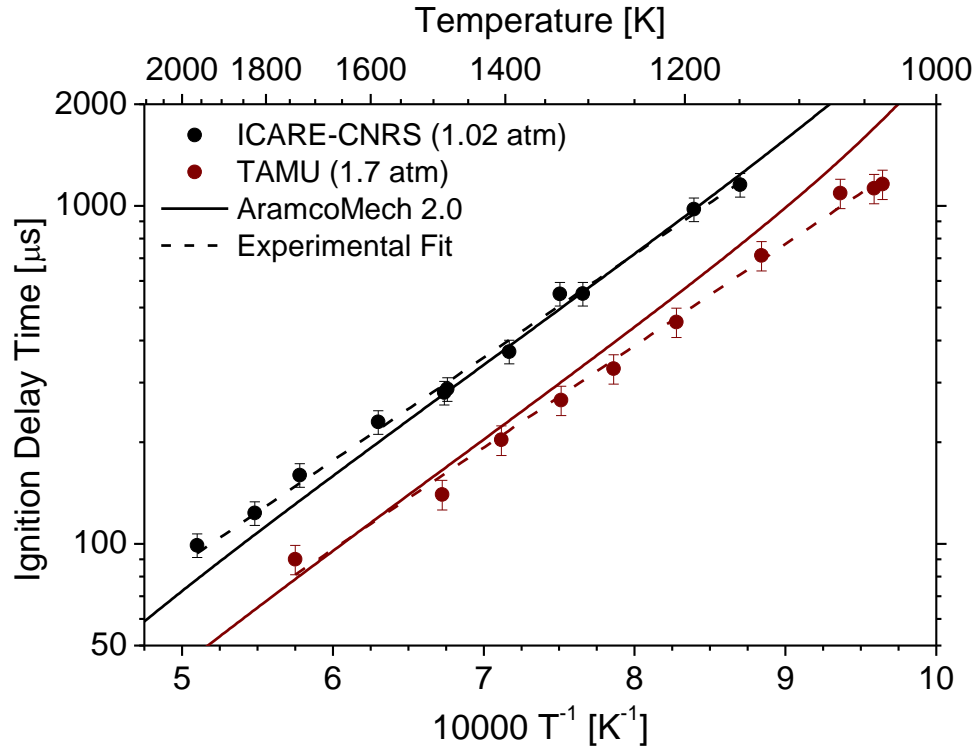


Figure 19. Hydrogen ignition delay times at $\phi = 1.0$, diluted with 98% argon. TAMU data are from Krejci et al. [9] and K  romn  s et al. [10]. ICARE T_5 uncertainty is estimated to be 1%.

In Figure 19, the CNRS data are slower than those from the earlier TAMU data, but have the same slope. One important difference though is that these data were run at slightly different pressures. The TAMU data are 1.7 ± 0.3 atm and the CNRS data are 1.02 ± 0.06 atm. The pressure dependence is best illustrated by comparing the difference between the model curves, run at the average pressure of each set, and the data. Knowing the pressure effect based on the models, if the data were simply shifted by the difference of the models then they would be the same. Thus, the difference in the curves in Figure 19 is almost entirely a pressure effect. The scatter in both sets of data are roughly the same. With the knowledge that a quality experiment could be performed, the next set of

experiments included the additional complexity of adding the OPCs to a new mixture, Figure 20.

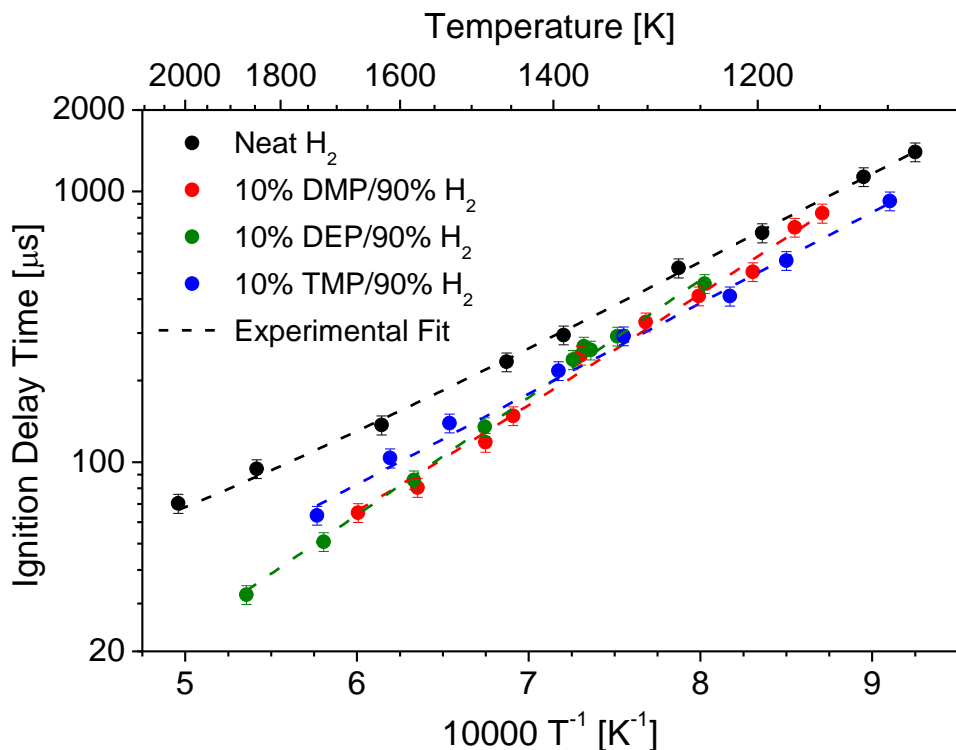


Figure 20. Hydrogen-based ignition delay times ($\phi = 0.5$, 1 atm, diluted with 98% argon). ICARE T₅ uncertainty is estimated to be 1%.

The OPCs all decrease the ignition delay time in Figure 20. It is also nearly impossible to distinguish DMP from DEP. Both of these have slopes that are slightly steeper than those of the TMP/hydrogen or hydrogen curves. The TMP curve has a slope that is more similar to that of the neat hydrogen. A useful comparison for modeling the OPCs is to look at the chemicals as concentrations rather than as ϕ in Figure 21.

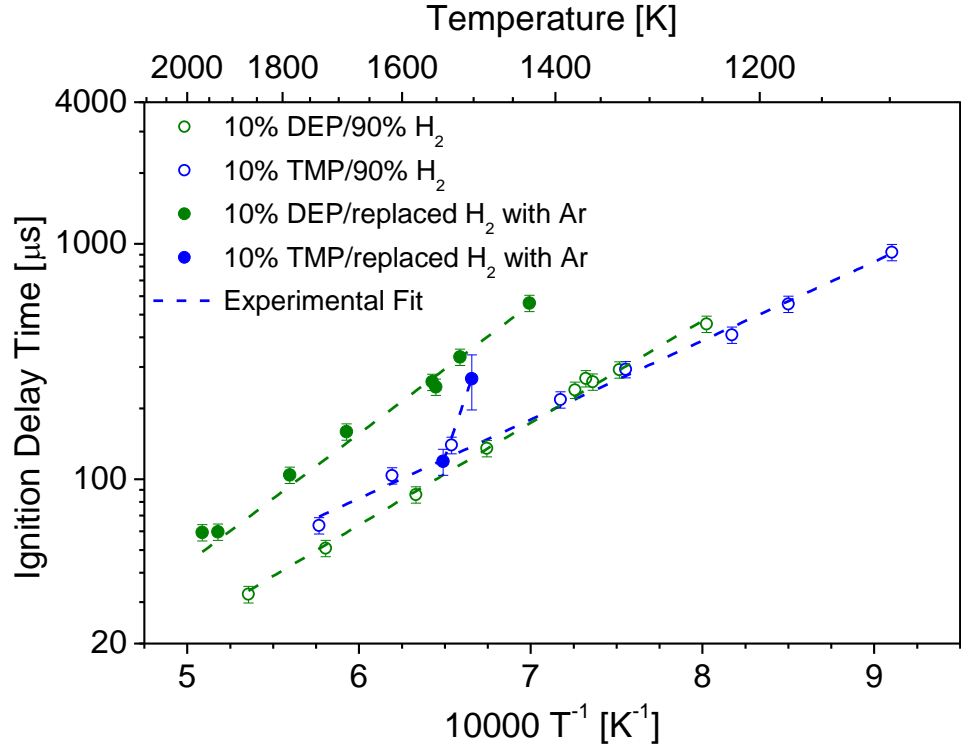


Figure 21. Concentration-varying experiments. The base OPC/H₂ are $\phi = 0.5$ and the concentrations are modified by replacing H₂ with Ar. ICARE T₅ uncertainty is estimated to be 1%.

A correlation for ignition delay times can be written as Eqn. 4.3, and therefore ignition delay time of a mixture can be understood as proportional to the concentrations of the constituent gases, Eqn. 4.4 [11]. In changing equivalence ratio, the concentrations of H₂, the OPC, and O₂ all vary. For modeling, it is simpler for only a single component to change.

$$\tau = A[H_2]^a[OPC]^b[O_2]^c[Ar]^d \exp\left(\frac{E_a}{RT}\right) \quad (4.3)$$

$$\tau \propto [H_2]^a[OPC]^b[O_2]^c[Ar]^d \quad (4.4)$$

The replaced mixtures in Figure 21 are the mixtures from Figure 20 with the hydrogen replaced with argon. This keeps the concentrations for the OPC and O₂ the same, and although the concentration of argon changes, because this is a highly dilute mixture (98% Ar) the difference is minimal. This allows the curves to be directly comparable to one another. In this case, it is seen that the addition of hydrogen to DEP decreases the ignition delay. TMP is an interesting case. The slope for TMP is extremely high. The OH* emission at lower temperatures for TMP were very small and thus the uncertainty is higher for these two points than most other points. It was not possible to go any lower in temperature than shown. On the other end, a higher temperature was also not possible to reach because the mixture began to react after the incident shock wave and before the reflected shock wave. Basically, TMP reacts very fast if the necessary temperature is reached, but if it is below that temperature, the time it takes to react quickly increases.

IV.4 OPC Ignition Delay Times in Ethylene Mixtures

Chemical kinetics models are typically built up in stages from hydrogen to increasingly complex molecules. To investigate the interactions between hydrocarbon chemistry and OPC chemistry, ethylene was used as the primary fuel with the OPCs in additional ignition delay time experiments. Figure 22 shows ethylene mixtures with the three OPCs.

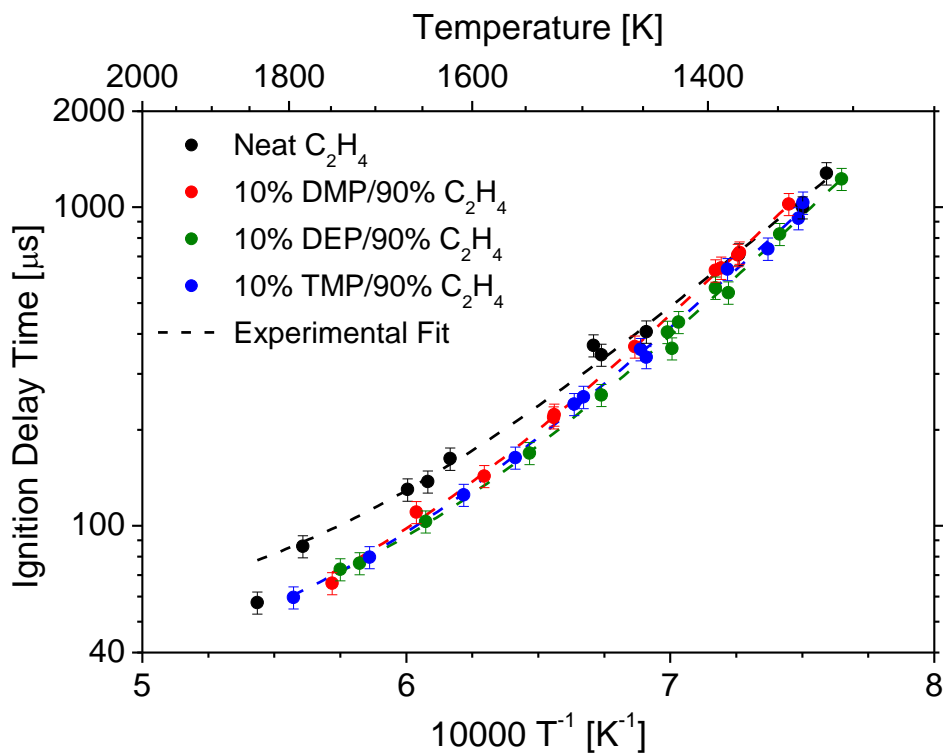


Figure 22. Ethylene-based ignition delay times ($\phi = 1.0$, 1 atm, diluted with 98% argon). ICARE T_5 uncertainty is estimated to be 1%.

The neat ethylene curve at $\phi = 1.0$, Figure 22, is generally slower than the OPC data. Since the scatter is low for these data sets, the comparison of the experimental fits is a useful metric to compare the OPCs to each other by how they differ from the neat mixture. At 1800 K, all of the OPCs decrease the ignition delay time by 30%. The DEP and TEP remain close to each other and end up decreasing the ignition delay time by about 15% at 1400 K. DMP approaches the neat ignition delay time as temperature decreases and even begins to increase it below 1400 K. This temperature effect indicates that at high temperature the OPCs must be driving the ignition delay time, and at lower temperatures, reactions involving ethylene become more important. Because the potential applications

of these experiments are related to fire suppression and to destroying Sarin, the primary interest is in the fuel lean behavior up to stoichiometric conditions. The fuel lean ethylene experiments, Figure 23, show similar behavior to the $\phi = 1.0$ case.

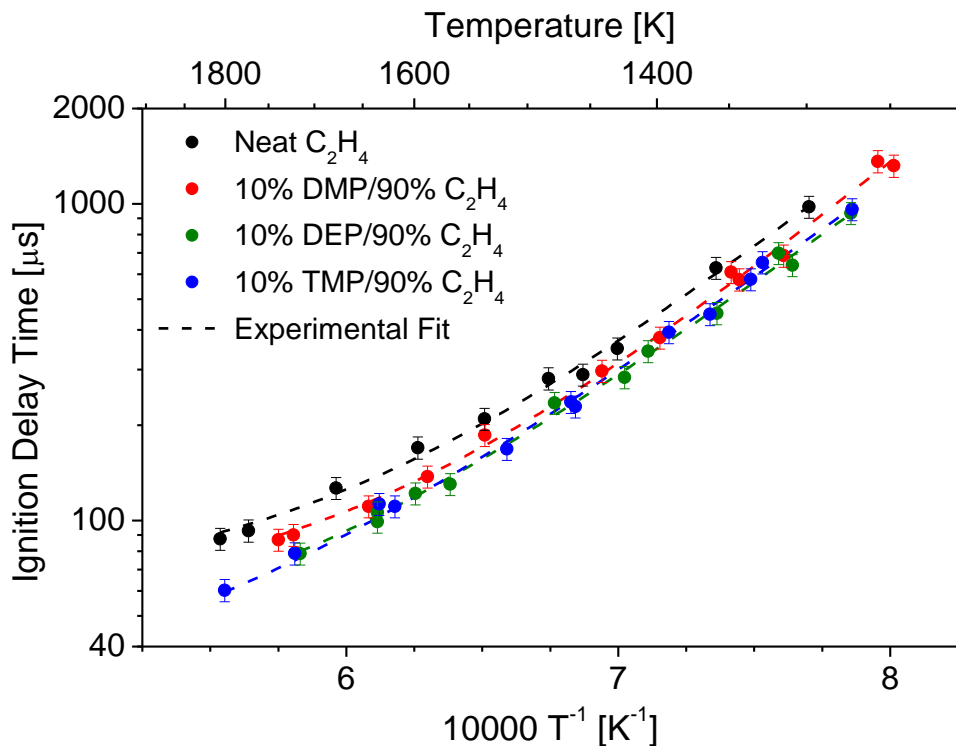


Figure 23. Ethylene-based ignition delay times ($\phi = 0.5$, 1 atm, diluted with 98% argon). ICARE T_5 uncertainty is estimated to be 1%.

The OPCs seem to have more of an effect within the entire range in Figure 23 than with the stoichiometric experiments in Figure 22. At around 1700 K, DEP and TMP, which are indistinguishable from one another in their impact on the ignition delay time, have a large 30% decrease on the ignition delay time compared to the neat mixture. They then begin to approach the neat mixture ignition delay time and around 1400 K, they level

off to within 20% of the neat mixture. DMP is again different than the others in that it stays at roughly a 15% decrease throughout the entire range studied. This result is different from the fuel lean case where it had a crossover point.

An interesting feature in the OH* profiles is a pre-ignition event found in ethylene mixtures. This feature reveals itself below temperatures of 1500 K in both the $\phi = 0.5$ and $\phi = 1.0$ experiments. It can be found in all of the ethylene mixtures regardless of the OPC used or even in the absence of an OPC. Experimental OH* profiles are shown in Figure 24.

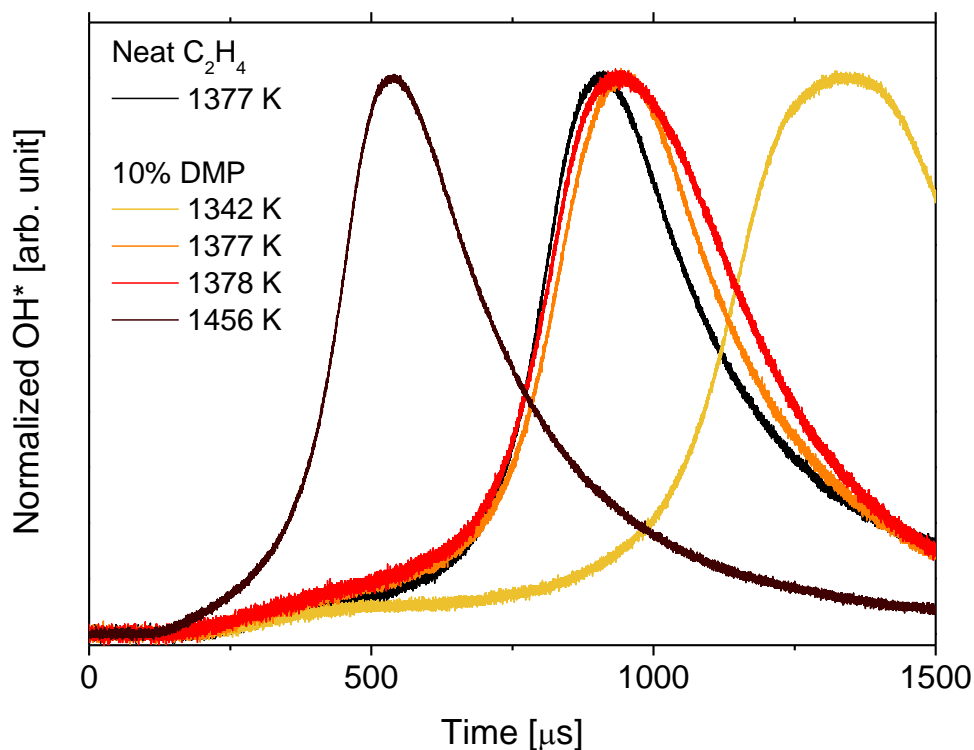


Figure 24. Normalized ethylene OH* sidewall profiles ($\phi = 1.0$, 1 atm, diluted with 98% argon). Temperature uncertainty is 1%.

Figure 24 shows that at high temperatures the pre-ignition event starts to become lost due to the speed at which ignition is occurring, but at lower temperatures the ignition can become very pronounced, such as the 1342-K profile shown. To demonstrate that this result is both a very repeatable event and that it is due to ethylene, three other curves are shown for ~ 1377 K. The two DMP experiments shown are very close to one another and overlap during the pre-ignition event. This coincidence in results indicates that this is indeed a repeatable event. Likewise, the neat ethylene curve closely matches the two DMP experiments at ~ 1377 K. Thus, the logical conclusion is that the pre-ignition is likely due to the ethylene, and this is also supported by other ethylene experiments not shown.

IV.5 References

- [1] P. Vieille, Sur les discontinuités produites par la détente brusque de gaz comprimés, *Comptes Rendus* 129 (1899) 68.
- [2] N.A. Fomin, 110 years of experiments on shock tubes, *J. Eng. Phys. Thermophys.* 83 (2010) 1118-1135.
- [3] M.F. Campbell, *Studies of biodiesel surrogates using novel shock tube techniques*, Stanford University, 2014.
- [4] M. Yahyaoui, N. Djebaïli-Chaumeix, C.E. Paillard, S. Touchard, R. Fournet, P.A. Glaude, F. Battin-Leclerc, Experimental and modeling study of 1-hexene oxidation behind reflected shock waves, *Proc. Combust. Inst.* 30 (2005) 1137-1145.
- [5] A. Comandini, G. Pengloan, S. Abid, N. Chaumeix, Experimental and modeling study of styrene oxidation in spherical reactor and shock tube, *Combust. Flame* 173 (2016) 425-440.
- [6] E.L. Petersen, R.K. Hanson, Nonideal effects behind reflected shock waves in a high-pressure shock tube, *Shock Waves* 10 (2001) 405-420.

- [7] O. Mathieu, W.D. Kulatilaka, E.L. Petersen, Experimental and modeling study on the effects of dimethyl methylphosphonate (DMMP) addition on H₂, CH₄, and C₂H₄ ignition, *Combust. Flame* 191 (2018) 320-334.
- [8] O.E. Mathieu, W.D. Kulatilaka, E.L. Petersen, Shock-tube studies of tri-ethyl-phosphate (TEP) kinetics at high temperatures in: 55th AIAA Aerospace Sciences Meeting, American Institute of Aeronautics and Astronautics, 2017.
- [9] M.C. Krejci, O. Mathieu, A.J. Vissotski, S. Ravi, T.G. Sikes, E.L. Petersen, A. Kérmonès, W. Metcalfe, H.J. Curran, Laminar flame speed and ignition delay time data for the kinetic modeling of hydrogen and syngas fuel blends, *J. Eng. Gas. Turb. Power.* 135 (2013) 021503-021503.
- [10] A. Kéromnès, W.K. Metcalfe, K.A. Heufer, N. Donohoe, A.K. Das, C.-J. Sung, J. Herzler, C. Naumann, P. Griebel, O. Mathieu, M.C. Krejci, E.L. Petersen, W.J. Pitz, H.J. Curran, An experimental and detailed chemical kinetic modeling study of hydrogen and syngas mixture oxidation at elevated pressures, *Combust. Flame* 160 (2013) 995-1011.
- [11] G. Ben-Dor, O. Igra, T. Elperin, A. Lifshitz, Ignition Delay Times in: *Handbook of Shock Waves*, Academic Press, San Diego, 2001, Vol. 3 3.

CHAPTER V

QUANTUM CHEMISTRY MODELING

Rather than attempting to modify an existing organophosphorus compound chemical kinetics mechanism, it was decided to create a model from first principles both to gain the conceptual knowledge of how such a mechanism is created and to avoid any biases that may occur when starting from an existing model. That is to say that the new model's species and Arrhenius parameters will eventually be completely recalculated, but that the existing LLNL model, Jayaweera et al. [1], will serve as the scaffolding upon which this new mechanism will be built. As such, the current model is created using ab initio methods with Gaussian 09.

When writing a kinetics mechanism, the starting place is determining the thermochemistry database of the likely reaction species. Quantities needed for this database include species structure, enthalpy of formation (h_f^0), as well as sensible enthalpy ($h_T^0 - h_{298\text{ K}}^0$), specific heat at constant pressure (C_p), and entropy (s) as a function of temperature. Here, 0 denotes normal pressure. Of these fundamental chemical properties, h_f^0 is the most critical and as such was the starting place to begin calculations.

V.1 Heat of Formation

Heats of formation are calculated by first determining the most stable conformer at 0 K. To save time, a low-accuracy method is typically used to get an initial guess of the correct geometry. The most stable configuration is used as the geometry input into a more-

accurate quantum chemistry method to calculate the Gaussian h_f^0 . Note that unless otherwise stated, properties herein are on a molar basis. The difference between the Gaussian h_f^0 and standard h_f^0 is the reference state of the constituent atoms. Gaussian calculates the heat of formation as if bonds were broken and the atoms completely disassociated. This definition of $h_{f,Gaus}^0$ is different from the standard macro-level h_f^0 , whose reference states are determined by arbitrarily defining some species to be zero ($C_{(s)}$, $H_{2(g)}$, $O_{2(g)}$, $P_{4,(s)}$ or white phosphorus, and N_2). Moreover, the Gaussian h_f^0 is not a unique property, but strongly depends on the quantum method employed. The link between these two definitions is to use the h_f^0 of individual atoms compared to the known h_f^0 of these atoms. In practice, this is done using Eq. 5.1.

$$h_f^0 = h_{f,Gaus}^0 - \sum n_i (h_{f,i,Exp}^0 - h_{f,i,Gaus}^0) \quad (5.1)$$

The variables in Eq. 5.1 are as follows: $h_{f,Gaus}^0$ is the species enthalpy of formation at 298 K, n_i is the number of a given element, and $h_{f,i,Exp}^0$, $h_{f,i,Gaus}^0$ are the atoms' experimental (literature) and Gaussian-derived enthalpies of formation, respectively. Because the Gaussian h_f^0 depends on the quantum method used, in Eq. 5.1, it is mandatory that the Gaussian enthalpies for the species and the atom be calculated with the same level of theory. One difficult task is thus to identify which level of theory, that is to say which combination of a quantum method and basis set would best model our given molecules.

In the interest of computational efficiency, it is often beneficial to use composite methods to calculate accurate heats of formation. Composite methods are efficient because they have been designed and validated to compute h_f^0 using sequences of high-level methods with small basis sets and low-level methods with large basis sets. A composite method solves the Schrödinger equation by applying various assumptions; whereas, a basis set describes the solution of the complex wave function by the linear combination of simple Gaussian functions. The accuracies of these basis sets are influenced by how many functions s are taken into account to describe each atomic orbital (s , p , d , f) that are then combined linearly to emulate the molecular orbitals. Higher-level methods will include more interactions.

There are a vast number of quantum chemistry composite methods dedicated to the calculations of heats of formation. The issue becomes one of computational efficiency versus accuracy. A literature review of OPCs reveals the use of G3B3 in Kan et al. [2], G3X in Dorofeeva and Moiseeva [3] and Haworth et al. [4], G3X-RAD in Hemelsoet et al. [5], and CSB-QB3 in Sullivan et al. [6] and Khalfa et al. [7]. G3B3 is a commonly used composite method that has shown to be highly successful; however, the CSB-QB3 is about as accurate and much faster [8, 9]. The G3X method is an improvement of the G3B3 method as it employs a larger basis set (6-31G(2df,p) versus 6-31G(d)) for the geometry optimization step and the harmonic vibration frequencies determination [10]. In both composite methods, B3LYP, a density functional theory, is used for these two steps. G3X-K is also used because its density function M06-2X, which is different than other methods, is needed to obtain many of the transition states, discussed later [11]. Of the methods

listed, G3X-RAD is expected to be the most accurate and the most computationally intensive. The G3X-RAD method is essentially the G3X method but designed to work well specifically with open shell systems (radicals) [12]. Finally, we included an additional method in this study, ROCBS-QB3, which like G3X-RAD, is also supposed to be particularly good at open shell systems [13]. The order of computational cost is roughly $\text{CBS-QB3} < \text{ROCBS-QB3} < \text{G3B3} < \text{G3X} < \text{G3X-K} \approx \text{G3X-RAD}$.

In all the G2-4 family of methods, it is assumed that the energy changes between various increasingly higher levels of theory are additive. For example, the energy calculated first is summed with the difference between it and the next higher level of theory with a single point calculation, etc. G3B3 and G3X use B3LYP level of theory followed by single point calculations at the QCISD(T,FC), MP4, and MP2 levels of theory. G3B3 stops here, but G3X has one additional computation, HF. G3X-K is a permutation of the G3X line of composite methods that uses the M06-2X density function for geometry and zero-point energies. G3X-RAD is similar to G3X in its sequence: B3LYP, ROCCSD, ROMP4 twice, ROMP2, and ROHF. In contrast to the additive approach, the CSB methods extrapolate using various orders of computational complexity to reach the final, calculated energies. Specifically, the CBS-QB3 method with a geometry calculation at the B3LYP level of theory, a frequency calculation and then finishes with single point calculations at the CCSD(T), MP4SDQ, and MP2 levels that it extrapolates to obtain the final energies.

Not all of these methods could be performed on all species due to the computation cost. The compromise is to pick a few key methods to use on molecules with known heats

of formation and then use the two best performing methods on all other molecules in the thermodynamic database. Because existing literature information exists on some C-H-O-P-N species, composite methods accuracy can be refined by performing bond additivity corrections (BAC) can be added to the various methods. A BAC is an empirical correction made to an individual bond to account for differences between computed values and experimental values. The BAC's are calculated by minimizing the weighted sum-of-squares errors between the experimental h_f^0 and the calculated h_f^0 for all known species. The weight is based on the relative uncertainty of each species. The relative uncertainty is a rough estimate, which for each species combines the uncertainty of each value with the uncertainty between the values by the root sum squared method and then normalizes by the group average. A table of computed and literature values is given as Table 2.

Note that there are discrepancies in the NIST database for PH, PH₃, and PN [14]. For example, in Chase [15] the table and quick reference value for PH is 55.8 kcal/mol, but the paragraph value is 60.6 kcal/mol. Chase cites Jordan [16] as the source of the bond dissociation energy used to calculate the heat of formation, 70.44 kcal/mol. Based on assumptions about the *d* orbital, Jordan [16] gives the PH bond energy as 70.44 – 70.99 kcal/mol. A quick calculation with the given disassociation energy results in a PH heat of formation between -57.3 – -56.8 kcal/mol. Lodders [14] states that this is because of an incorrect phosphorus reference state and gives 56.4 kcal/mol as the correct heat of formation.

Table 2. Heats of formation of various methods with BAC for known literature species. Units are kcal/mol. Literature references: ^aChase [15], ^bGurvich et al. [17], ^cCox et al. [18], ^dLuo [19], ^eBerkowitz et al. [20], ^fGunn and Green [21], ^gGingerich [22], ^hPotter and DiStefano [23], ⁱGaydon [24], ^jHildenbrand and Lau [25], ^kHartley [26], ^lDorofeeva and Moiseeva [3], ^mRabinovich et al. [27], ⁿAl-Maydama et al. [28], ^oDavies et al. [29], ^pLuo and Benson [30], ^qLodders [14]

Molecule	CBS-QB3	ROCBS-QB3	G3B3	G3X-K	G3X-RAD	Literature	SSE Weight
PH	56.7	56.3	55.2	56.6	55.3	56.4±8.0 ^q 55.2±3.1 ^b	0.90
PH ₂	31.5	31.3	31.3	31.4	31.2	28.6±1.5 ^b 34.0±0.6 ^{d,e}	0.91
PH ₃	0.8	1.0	1.2	0.7	1.3	1.3±0.4 ^f 1.1 ^q	0.65
PO	-7.8	-7.6	-17.0	-7.6	-8.5	-5.6±1.0 ^a -6.7±0.8 ^b	0.83
PO ₂	-70.2	-69.9	-70.6	-70.1	-69.7	-75.2 ^a -67.3±2.4 ^b	0.94
PN	43.3	43.0	41.9	43.9	42.2	41.1±3.5 ^{b,g} 20.9±1.2 ^{q,h} 53.0±19.0 ^{a,i}	0.68
HPO	-22.4	-22.5	-23.2	-22.4	-23.0	-13.6±9.6 ^b -34.2±4.0 ^j	0.48
HOPO	-111.5	-111.7	-111.3	-110.6	-111.2	-110.6±3.0 ^j	0.97
HOPO ₂	-169.0	-169.3	-169.3	-169.6	-169.2	-168.8±4.0 ^j	0.98
P(CH ₃) ₃	-25.2	-25.1	-23.3	-24.7	-24.1	-24.2±1.2 ^k -22.9±1.0 ^{l,m}	0.95
P(OCH ₃) ₃	-167.5	-167.3	-167.5	-167.6	-167.5	-167.1±1.9 ^{l,m} -168.6±1.5 ^k	0.99
P(CN) ₃	114.7	114.6	112.6	113.4	113.1	108.0±6.0 ^{l,m} 107.2±1.8 ^{l,n} 135.9±6.0 ^{l,o}	0.91
CH ₃ PH ₂	-5.4	-5.2	-4.5	-5.1	-4.6	-4.6±1.5 ^{l,p}	0.67
(CH ₃) ₂ NP(CN) ₂	63.3	63.2	63.2	64.2	63.6	59.5±3.8 ^{l,m} 54.7±1.3 ^{l,n}	0.94

Table 2 lists the methods used for calculation of the species with literature values in order from least computational cost, CBS-QB3, to the most, G3X-RAD. CBS-QB3 and

G3B3 are chosen due to their widespread use in the literature. ROCBS-QB3 and G3X-RAD are chosen because they are methods well equipped to handle open shell systems. In comparing the computed h_f^0 to the literature value, it can be seen that G3B3 is significantly different from the literature value for PO and because of this G3B3 is deemed unreliable for use on the rest of the thermodynamic calculations. Additionally, CBS-QB3 is eliminated because although it is close to ROCBS-QB3, it is expected to do worse with future unknown radicals. This result leaves ROCBS-QB3 and G3X-RAD as the two choices for the remainder of the thermochemistry database. In the future, the intent is that both will be used and if there is a discrepancy, the problematic species will be further investigated; however, for the purposes of this dissertation, only ROCBS-QB3 was used.

V.2 *Sensible Enthalpy, Specific Heat, and Entropy*

Once the minimum energy geometry and heats of formation are known, the rest of the properties are relatively easy to compute. Essentially, Gaussian determines the electronic, translational, rotational, and vibrational partition functions. Once these partition functions are obtained, the macro state properties are obtained from the micro state properties using Eq. 5.2-5.4 [31, 32].

$$U = Nk_b T^2 \left. \frac{\partial \ln Z}{\partial T} \right|_{V,N} \quad (5.2)$$

$$S = Nk_b \ln Z + \frac{U}{T} \quad (5.3)$$

$$C_P = T \left. \frac{dS}{dT} \right|_{P,N} \quad (5.4)$$

Where k_b is the Boltzmann constant, N is the number of particles, and Z is the canonical partition function containing all contributing partition functions ($Z = \prod q_i$). While the electronic, translational, external rotational partition functions are straightforward to calculate from the geometry, the vibrational partition function requires knowledge of the harmonic vibration frequencies. However, among the vibrational modes identified by Gaussian, some of them are actually hindered rotors. To properly handle these modes in the calculation of the partition function, it is required to identify their associated vibration frequency and to compute their potential energy surface (PES). Only then are the final calculations performed using CanTherm [33, 34].

CanTherm is a Python script, developed at MIT, which includes a Pitzer-Gwinn formalism to deal with the hindered rotor modes. From the atom Cartesian coordinates, force constant matrix, and hindered rotors PES (at the B3LYP/6-311g(2d,d,p) level of theory in this study), CanTherm returns the individual contributions (translation, vibration, external and internal rotors, electronic) to the sensible enthalpy, the entropy and the constant pressure heat capacities along with the individual partition functions. Combined with the standard heat of formation, the thermoproperties are fitted with the standard

NASA polynomial form for use in chemical kinetic software. The basic NASA polynomials are shown in Eqs. 5.5 – 5.7.

$$\frac{C_p}{R} = a_1 + a_2 T + a_3 T^2 + a_4 T^3 + a_5 T^4 \quad (5.5)$$

$$\frac{H}{RT} = a_1 + a_2 \frac{T}{2} + a_3 \frac{T^2}{3} + a_4 \frac{T^3}{4} + a_5 \frac{T^4}{5} + \frac{a_6}{T} \quad (5.6)$$

$$\frac{S}{R} = a_1 \ln T + a_2 T + a_3 \frac{T^2}{2} + a_4 \frac{T^3}{3} + a_5 \frac{T^4}{4} + a_7 \quad (5.7)$$

In Eqs. 5.5 – 5.7, a_i are all constants that need be fit to known thermodynamic properties. A custom routine created for this purpose uses Matlab's `lsqlin` function with an active set algorithm to solve the constrained least squares regression problem. The solution is to rewrite Eqs. 5.5 – 5.7 in the form of $Ax = b$, Eqs. 5.8 – 5.10. The NASA polynomials are broken into two fits, a high-temperature and a low-temperature region. Next, constraints are assigned such that H , C_p , $\frac{dC_p}{dT}$, and S are all continuous at the breakpoint temperature, T_{bp} , and that $\Delta H_{f,fit}^0 = \Delta H_{f,known}^0$ at 298 K. These constraints also imply other constraints, $\frac{dH}{dT}$, $\frac{d^2H}{dT^2}$, and $\frac{dS}{dT}$, are continuous at T_{bp} due to the thermodynamics relations: $C_p = \left(\frac{\partial H}{\partial T}\right)_p$ and $C_p = T \left(\frac{\partial S}{\partial T}\right)_p$. The constraints are written in matrix notation $Cx = d$, Eqs. 5.11 – 5.12. Attempting to use the second-order derivative constraints $\frac{d^2C_p}{dT^2}$ and $\frac{d^2S}{dT^2}$ results in dependences in the equality constraints.

$$A = \begin{bmatrix} 1 & T_1 & T_1^2 & T_1^3 & T_1^4 & 0 & 0 & 0 & \dots & 0 \\ \vdots & \vdots & \vdots & \vdots & \vdots & \vdots & \vdots & \vdots & \ddots & \vdots \\ 1 & T_{bp-1} & T_{bp-1}^2 & T_{bp-1}^3 & T_{bp-1}^4 & 0 & 0 & 0 & \dots & 0 \\ & & 0 & \dots & 0 & & 1 & T_{bp} & T_{bp}^2 & T_{bp}^3 & T_{bp}^4 & 0 & 0 \\ & & \vdots & \ddots & \vdots & & \vdots & \vdots & \vdots & \vdots & \vdots & \vdots & \vdots \\ & & 0 & \dots & 0 & & 1 & T_n & T_n^2 & T_n^3 & T_n^4 & 0 & 0 \\ 1 & \frac{T_1}{2} & \frac{T_1^2}{3} & \frac{T_1^3}{4} & \frac{T_1^4}{5} & \frac{1}{T_1} & 0 & 0 & \dots & 0 \\ \vdots & \vdots & \vdots & \vdots & \vdots & \vdots & \vdots & \vdots & \ddots & \vdots \\ 1 & \frac{T_{bp-1}}{2} & \frac{T_{bp-1}^2}{3} & \frac{T_{bp-1}^3}{4} & \frac{T_{bp-1}^4}{5} & \frac{1}{T_{bp-1}} & 0 & 0 & \dots & 0 \\ & & 0 & \dots & 0 & & 1 & \frac{T_{bp}}{2} & \frac{T_{bp}^2}{3} & \frac{T_{bp}^3}{4} & \frac{T_{bp}^4}{5} & \frac{1}{T_{bp}} & 0 \\ & & \vdots & \ddots & \vdots & & \vdots & \vdots & \vdots & \vdots & \vdots & \vdots & \vdots \\ & & 0 & \dots & 0 & & 1 & \frac{T_n}{2} & \frac{T_n^2}{3} & \frac{T_n^3}{4} & \frac{T_n^4}{5} & \frac{1}{T_n} & 0 \\ \ln T_1 & T_1 & \frac{T_1^2}{2} & \frac{T_1^3}{3} & \frac{T_1^4}{4} & 0 & 1 & 0 & \dots & 0 \\ \vdots & \vdots & \vdots & \vdots & \vdots & \vdots & \vdots & \vdots & \ddots & \vdots \\ \ln T_{bp-1} & T_{bp-1} & \frac{T_{bp-1}^2}{2} & \frac{T_{bp-1}^3}{3} & \frac{T_{bp-1}^4}{4} & 0 & 1 & 0 & \dots & 0 \\ & & 0 & \dots & 0 & & \ln T_{bp} & T_{bp} & \frac{T_{bp}^2}{2} & \frac{T_{bp}^3}{3} & \frac{T_{bp}^4}{4} & 0 & 1 \\ & & \vdots & \ddots & \vdots & & \vdots & \vdots & \vdots & \vdots & \vdots & \vdots & \vdots \\ & & 0 & \dots & 0 & & \ln T_n & T_n & \frac{T_n^2}{2} & \frac{T_n^3}{3} & \frac{T_n^4}{4} & 0 & 1 \end{bmatrix} \quad (5.8)$$

$$x^T = [a_{1,LT} \quad \dots \quad a_{7,LT} \quad a_{1,HT} \quad \dots \quad a_{7,HT}] \quad (5.9)$$

$$b^T = \frac{1}{R} \left[C_{p,1} \quad \dots \quad C_{p,n} \quad \frac{H_1}{T_1} \quad \dots \quad \frac{H_n}{T_n} \quad S_1 \quad \dots \quad S_n \right] \quad (5.10)$$

$$C_{left} = \begin{bmatrix} 1 & \frac{T_{bp}}{2} & \frac{T_{bp}^2}{3} & \frac{T_{bp}^3}{4} & \frac{T_{bp}^4}{5} & \frac{1}{T_{bp}} & 0 \\ 1 & T_{bp} & T_{bp}^2 & T_{bp}^3 & T_{bp}^4 & 0 & 0 \\ 0 & 1 & 2 T_{bp} & 3 T_{bp}^2 & 4 T_{bp}^3 & 0 & 0 \\ \ln T_{bp} & T_{bp} & \frac{T_{bp}^2}{2} & \frac{T_{bp}^3}{3} & \frac{T_{bp}^4}{4} & 0 & 1 \end{bmatrix} \quad (5.11)$$

$$C_{\Delta H_f^0} = \left[1 \quad \frac{298.15}{2} \quad \frac{298.15^2}{3} \quad \frac{298.15^3}{4} \quad \frac{298.15^4}{5} \quad \frac{1}{298.15} \quad 0 \right]$$

$$C = \begin{bmatrix} C_{left} & -C_{left} \\ C_{\Delta H_f^0} & 0 \quad \dots \quad 0 \end{bmatrix}$$

$$d^T = \begin{bmatrix} 0 & \dots & 0 & \frac{\Delta H_f^0}{298.15 R} \end{bmatrix} \quad (5.12)$$

In these equations, the subscripts LT and HT stand for low temperature and high temperature, respectively. The vectors x , b , and d are presented transposed to conserve space. In addition to the least squares fitting, T_{bp} is optimized via Matlab's patternsearch with variables randomly initialized 30 times to further reduce fitting error. The fitting error is defined to be $\|error\|$. The norm of the relative error was also tried, but it resulted in worse overall fits. During the optimization process, one option is to scale the enthalpies by an arbitrary number. This scaling does not affect the final fit value but instead alters the importance (or weighting) of enthalpy in the error calculation. To validate the fitting procedure, a comparison was made to the Burcat et al. [35] fit of O₂, Figure 25.

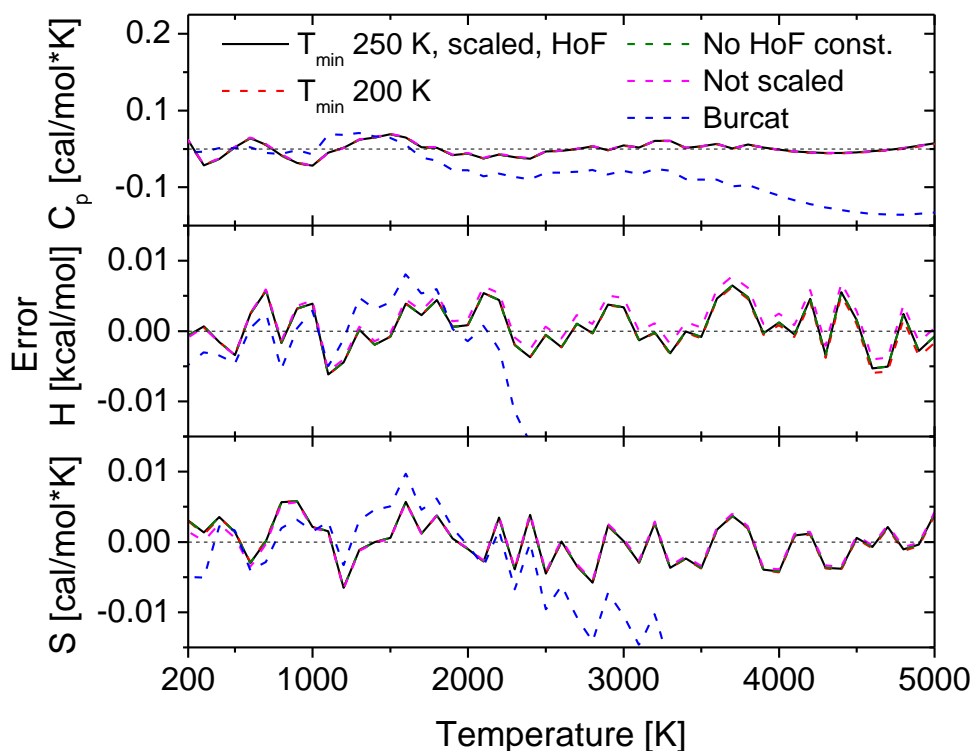


Figure 25. O₂ thermodynamic fitting error compared to NIST reference data [15]. The heat of formation constraint is $\Delta H_{f,O_2}^0 = 0$.

In Figure 25, all of the current study's fitting error is lower than that of the Burcat fit, whose error goes as high as 0.15 kcal/mol for enthalpy and 0.05 kcal/mol for entropy. These errors are not that significant in terms of typical fitting errors, but nevertheless this positive result does support the conclusion that the current study's fitting procedure is sufficient. There is not a major difference between the various versions of fitting performed. The biggest difference is that the unscaled procedure produces slightly more error after ~2000 K. The final choice was to include scaling, the heat of formation constraint, and set the minimum temperature at 250 K.

The species creating the mechanism were based on the primary species in the LLNL model. As this model is primarily for TMP and DMP, many of the species involving more-complex molecules such as those containing ethyl groups or those derived from DMMP were excluded. There are some additional molecules whose thermodynamic data were also calculated, as there will be some additional reactions that will likely be added to the mechanism which contain these species. Lastly, DEP was also calculated to provide the thermodynamic data necessary to calculate post-shock conditions for ignition delay time experiments. The fit thermodynamic data can be found in the Appendix. Two comparisons between the LLNL thermodynamic data and the thermodynamic data calculated herein are given in Figure 26 and Figure 27.

Figure 26 shows the current thermodynamic data of DMP (upper) and TMP (lower). The difference in enthalpy for DMP is as little as 4 kcal/mol and increases up to 15 kcal/mol. The difference is more pronounced in the enthalpy derivative, c_p after 1000 K. Overall the thermodynamic data for DMP are close to one another, but still might make a difference when implemented into a chemical kinetics mechanism. The TMP data are also close to one another but LLNL's C_p continues to increase beyond 3000 K and the calculated values tail off. Their issue is likely related to fitting as the infinity C_p is only related to the number of atoms. As for enthalpy, the differences are roughly the same as the DMP data. These two species were chosen to be shown as they exhibit the similarities between the two thermodynamic databases and because these primary species are particularly important for ignition delay time calculations. To show the other end of the spectrum PO[OH]Me and PO[OH]Me[Oet] data are given in Figure 27.

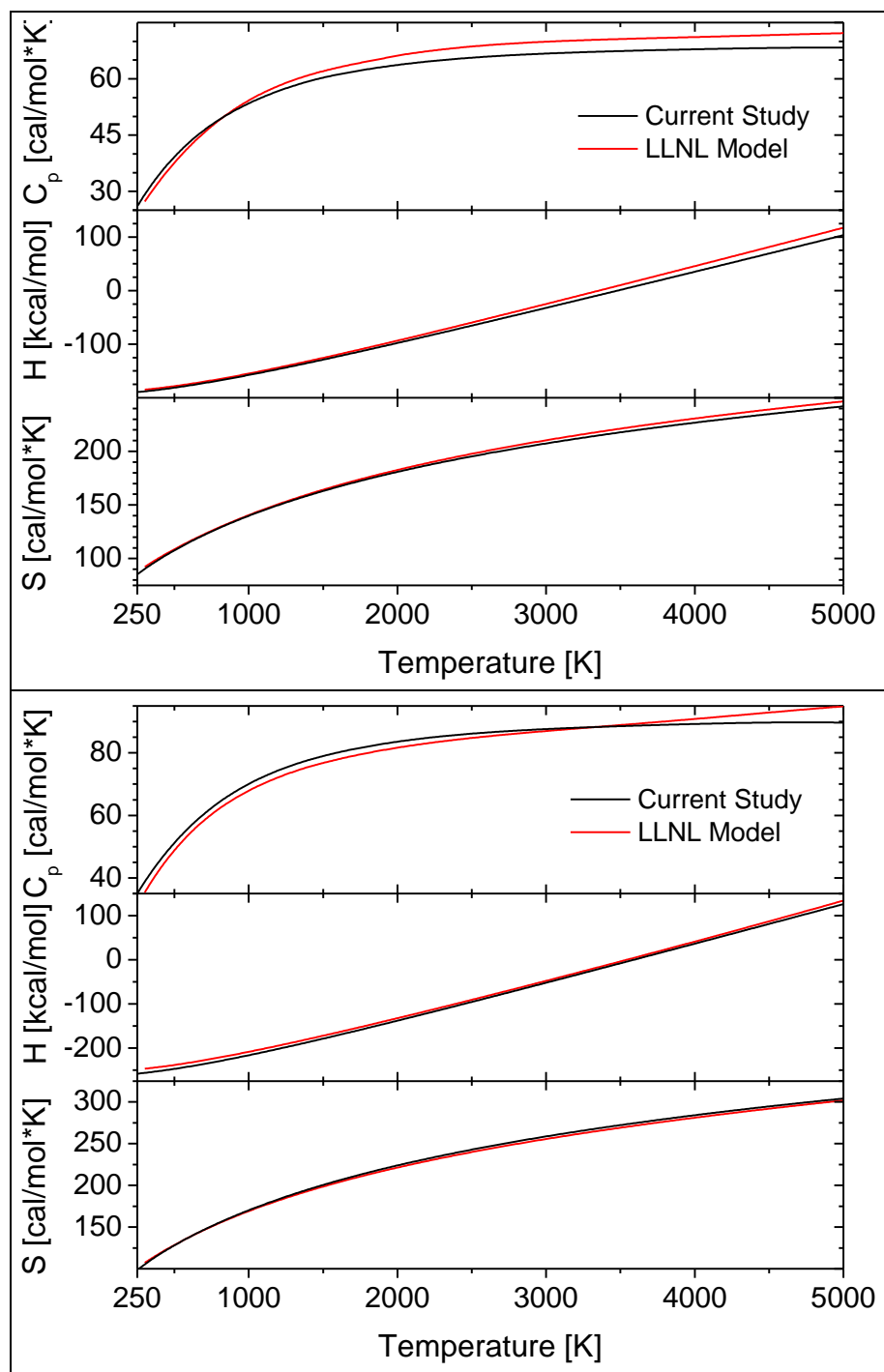


Figure 26. Thermodynamic data comparison for (upper) DMP and (lower) TMP.

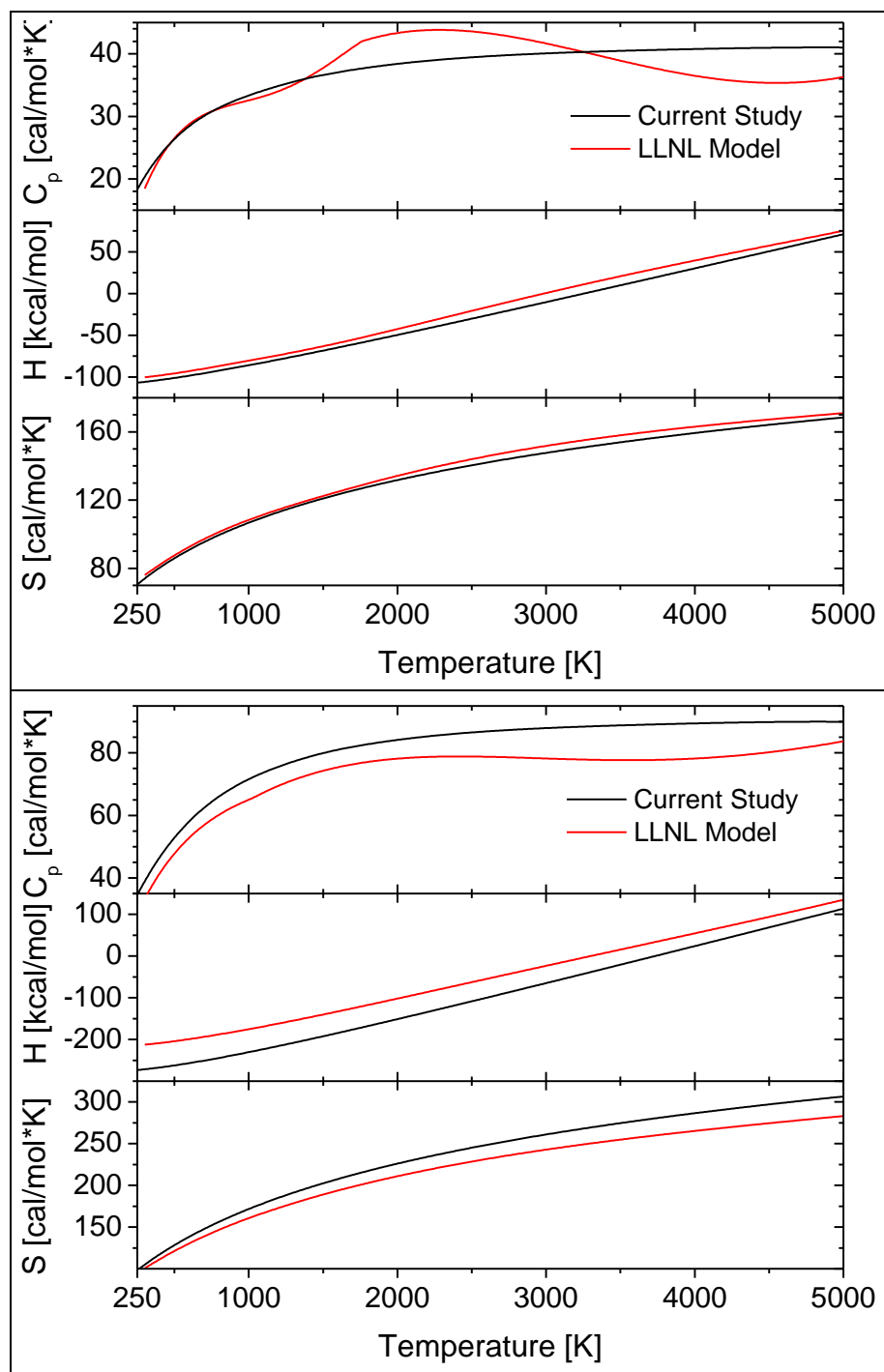


Figure 27. Thermodynamic data comparison for (upper) PO[OH]Me and (lower) PO[OH]Me[Oet].

The LLNL PO[OH]Me C_p data must be incorrect. Specific heats do not display the kind of behavior nor do they vary by the extreme amounts shown in Figure 27(upper). At first glance, the enthalpies are not too different, but upon further investigation the difference between the two enthalpies is as much as 10 kcal/mol when the order of magnitude is the same as this error. For this species, the current study's results are most likely more accurate than the literature value based on the irregular c_p .

Another species that varies dramatically is PO[OH]Me[Oet] in Figure 27(lower). The enthalpy differs by as much as 60 kcal/mol, entropy by 20 cal/mol K, and c_p by 35 cal/mol K. These differences are quite significant, and although most other species do not vary by this much, it does provide a good example of the differences that most species exhibit and that is in the heat of formation. Great care was taken in the current study to provide the highest quality heat of formations possible. A number of quantum chemistry composite methods were evaluated for known species and the one with the lowest error after a bond additivity correction was finally chosen as the method by which heats of formation would be taken. Thus, the heats of formation in the current study are semi-empirical, and the author feels they represent an accurate prediction as to what each species' heat of formation is. It is for this reason that the current study's thermodynamic data differ from those of the past and improves upon the existing foundation of OPC research.

V.3 Arrhenius Parameters

A chemical kinetics mechanism is much more than thermodynamics alone. Thermodynamics can be used to explain the movement of energy and heat, but it does not explain the process of how that happens and the time scale at which it does. Time-dependent reaction rates are necessary to describe how fast reactants are converted into products and, with many reactions defined, the interactions between various reactions. Transition State Theory, TST, is one way to theoretically calculate the coefficients that describe the oxidation/pyrolysis of fuels.

TST assumes that reactions occur on a path from reactants to products separated by an energy barrier between them, Figure 28. The transition state, AB^\ddagger or TS, is found at the maximum energy barrier between products and reactants and is a saddle point on the multidimensional potential energy surface. The reaction coordinate can be a bond length, an angle, a dihedral angle, or any combination of these geometric properties. It is assumed that only one reaction coordinate is important, but extensions of the theory can be derived to include higher-order dimensions. A representative bimolecular reaction would be $A + B \rightleftharpoons AB^\ddagger \rightarrow \text{Products}$. The key assumption in TST is that the reactants and AB^\ddagger are in quasi-equilibrium. Other assumptions include: the molecules obey classical mechanics (no quantum tunneling), and that Boltzmann distributions are applicable for all states (e.g., reaction rates are not extremely fast).

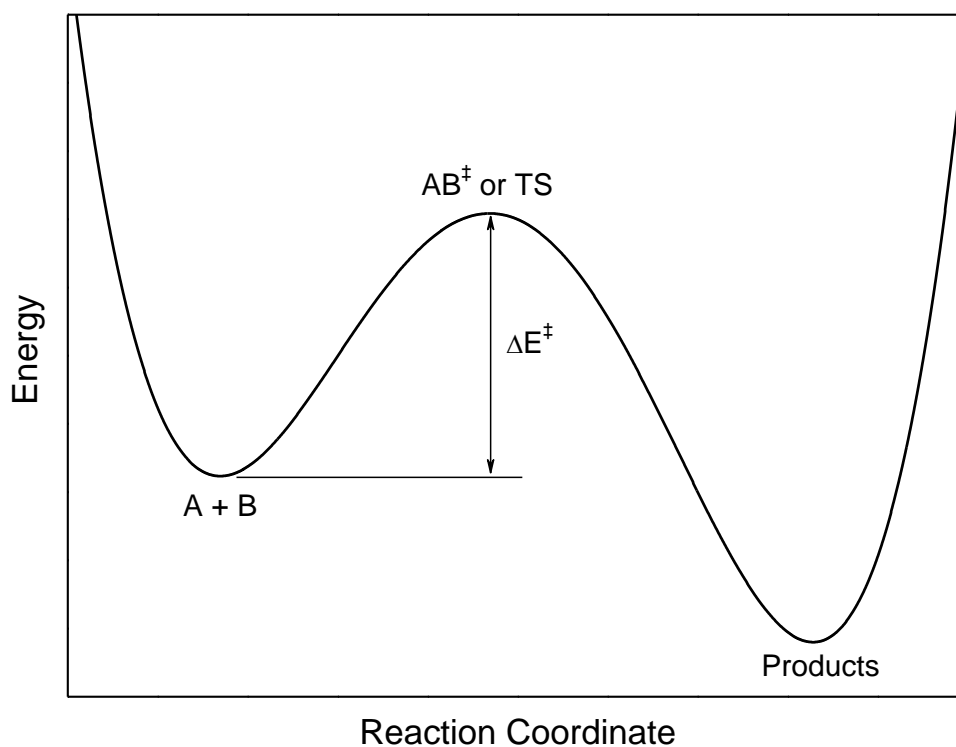


Figure 28. A potential energy surface of two reactants (A, B) into products along a reaction coordinate.

With the equilibrium assumption, the equilibrium condition can be written as Eq. 5.13, where superscript ‡ denotes the transition state, K_c is the equilibrium constant defined by molar concentrations, and brackets indicate concentration [36, 37].

$$K_c^\ddagger = \frac{[AB^\ddagger]}{[A][B]} \quad (5.13)$$

The rate of such a reaction, Eq. 5.14, can be written as the concentration of transition state molecules multiplied by the frequency of it overcoming the inhibiting

barrier, Figure 28. The substitution of Eq. 5.13 into this rate equation is also provided. The rate could also be written as a function of the reaction rate and concentrations of A and B as shown in Eq. 5.15.

$$\dot{\omega} = \nu[AB^\ddagger] = \nu[A][B]K_c^\ddagger \quad (5.14)$$

$$\dot{\omega} = k[A][B] \quad (5.15)$$

In these equations, $\dot{\omega}$ is the rate of production and ν is the TS frequency of vibration to overcome the barrier along the reaction coordinate. Through statistical thermodynamics, it can be shown that $\nu = k_B T/h$ [31]. In this equation, k_B is the Boltzmann constant and h is Planck's constant. Eqs. 5.14, 5.15 and the vibrational frequency definition can be combined to obtain Eq. 5.16 and then transformed into Eq. 5.17 by applying a logarithm to both sides.

$$k = \frac{k_B T}{h} K_P^\ddagger (RT)^{-\Delta n} \quad (5.16)$$

$$\ln k = \ln \frac{k_B}{h} + 2 \ln T + \ln K_P^\ddagger + \ln R \quad (5.17)$$

$(RT)^{-\Delta n}$ has been added to Eq. 5.16 to convert from unit concentration to unit partial pressure using $K_c^\ddagger = K_P^\ddagger (RT)^{-\Delta n}$ [37]. Since it is assumed that this reaction is a bimolecular one, $-\Delta n$ is equal to 1. By differentiating Eq. 5.17 with respect to temperature, Eq. 5.18 is obtained. This equation can be combined with the differentiated

Arrhenius equation, $k = A \exp(-E_a/RT)$, given as Eq. 5.19, to find a connection to activation energy, E_a , in Eq. 5.20.

$$\frac{d \ln k}{dT} = \frac{2}{T} + \frac{d \ln K_P^\ddagger}{dT} \quad (5.18)$$

$$\frac{d \ln k}{dT} = \frac{E_a}{RT^2} \quad (5.19)$$

$$E_a = 2RT + RT^2 \frac{d \ln K_P^\ddagger}{dT} \quad (5.20)$$

At equilibrium, the equilibrium constant defined by partial pressures can be related to the thermodynamic properties of the reactants and the TS. This relation is given as Eq. 5.21 and then combined with Eq. 5.16 into Eq. 5.22 which is also known as the Eyring equation [38].

$$K_P^\ddagger = \exp(-\Delta G^{\circ\ddagger}/RT) \quad (5.21)$$

$$k = \frac{k_B T}{h} RT \exp\left(-\frac{\Delta G^{\circ\ddagger}}{RT}\right) \quad (5.22)$$

Substituting Eq. 5.21 into Eq. 5.20 allows for the solution of E_a , Eq. 5.23, through application of the definition of Gibbs free energy ($G = H - TS$) and the Maxwell relation $C_p/T = (\partial S/\partial T)_P$.

$$E_a = \Delta H^{\circ\ddagger} + 2RT \quad (5.23)$$

Expanding Eq. 5.22 through the definition of Gibbs free energy and with substitution into Eq. 5.23 results in Eq. 5.24. Additionally, the pre-exponential factor of the Arrhenius equation can be identified and is explicitly stated in Eq. 5.25.

$$k = \frac{k_B T}{h} RT \exp\left(\frac{\Delta S^\ddagger}{R} + 2\right) \exp\left(-\frac{E_a}{RT}\right) \quad (5.24)$$

$$A = \frac{k_B T}{h} RT \exp\left(\frac{\Delta S^\ddagger}{R} + 2\right) \quad (5.25)$$

Through Eqs. 5.23 and 5.25, A and E_a can be determined from the TS entropy and enthalpy. Thus it is only necessary to repeat the previous thermodynamic calculations but using the transition state geometries to obtain the kinetic parameters. An example of a reaction, $\text{DMP} + \text{CH}_3 \rightleftharpoons \text{TS} \rightarrow \text{PO}[\text{Ome}]_2 + \text{CH}_4$, by TST is shown in Figure 29.

The H abstraction reaction $\text{DMP} + \text{CH}_3 \rightleftharpoons \text{TS} \rightarrow \text{PO}[\text{Ome}]_2 + \text{CH}_4$ can be looked at on Figure 29 as (a) \rightleftharpoons (b) \rightarrow (c). The reaction progresses by the methyl radical approaching the DMP molecule and attracting the H atom bonded to the central phosphorus atom. At some point, the energy will peak as the H atom is pulled from DMP to CH_3 . This process breaks DMP apart and results in a methane and $\text{PO}[\text{Ome}]_2$ molecules. With this TS calculated, MultiWell is used to directly calculate the rate coefficient as a function of temperature [39-41]. The results are then best fit to the Arrhenius equation to determine the kinetic coefficients. The process is based on the previously derived TST but

directly uses the partition functions instead of using the macrostate properties as intermediaries before fitting.

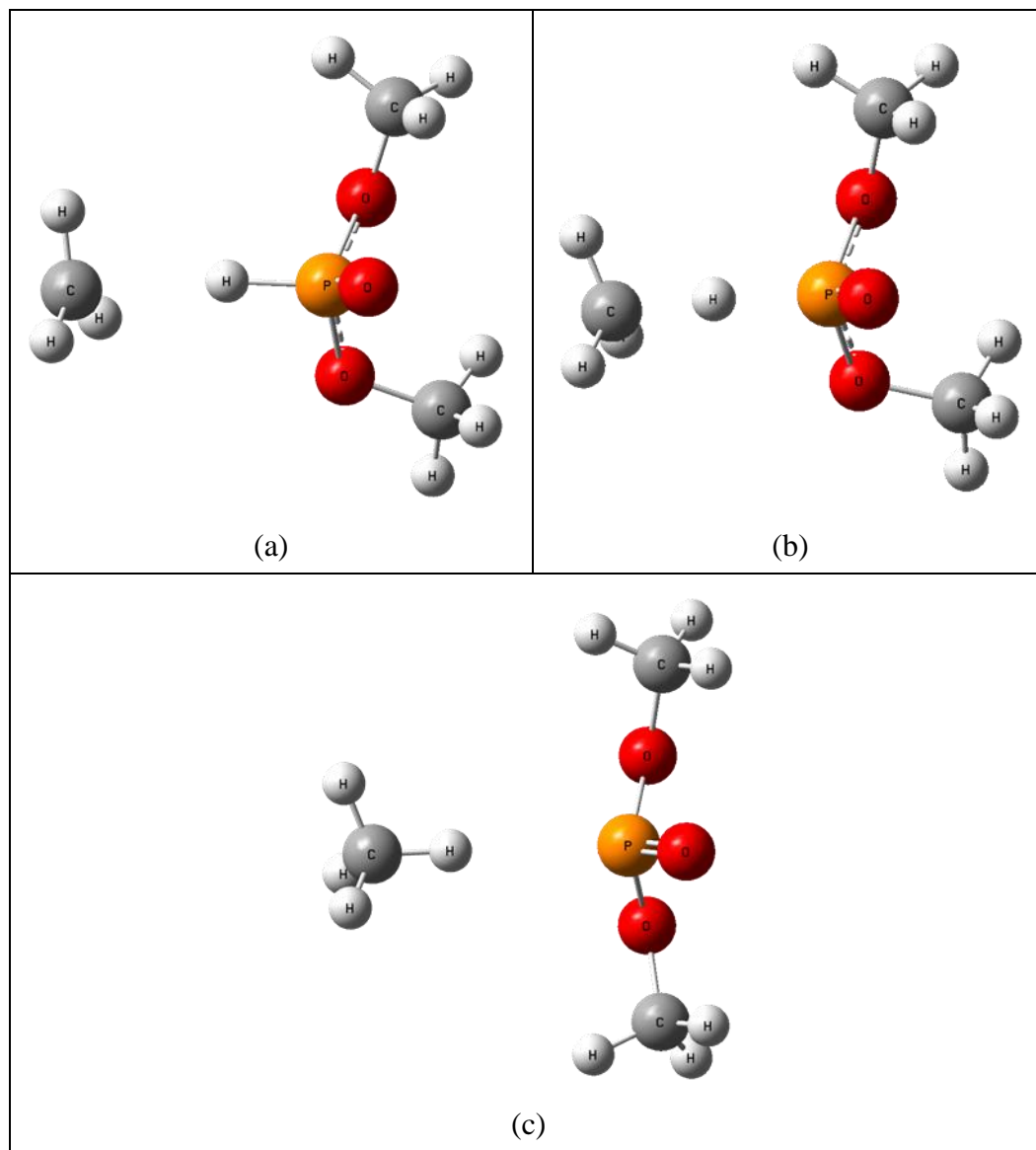


Figure 29. Optimized geometry at G3X-K level of theory of the reaction $\text{DMP} + \text{CH}_3 \rightleftharpoons \text{TS} \rightarrow \text{PO}[\text{Ome}]_2 + \text{CH}_4$. Optimized (a) reactants' geometries, (b) transition state geometry, and (c) products' geometries.

The above process is the basis for many of the calculations performed herein. The calculated kinetic parameters were performed at a G3X-K level of theory using a hindered rotor correction. It is necessary to use G3X-K rather than ROCBS-QB3 or G3X-RAD because the latter two rely on B3LYP which begins to show limits. This fact is particularly true when the reactions being modeled include P atoms. G3X-K uses the more recent method M06-2X, which does not exhibit these limits and allows for the calculation of more TS, such as H abstraction of OH. The master equation is solved with the MESMER software [42].

The master equation is a set of equations that describes the population and the transitions between the different vibrational states of the reactants, the TS, and the products. The transitions between different energy levels are governed by collisions with the bath gas, while the transitions between these energy levels and the products are governed by rate constants. A rate constant exists for each level, according to RRKM theory, but the final, apparent rate constant (used in the final model) is an eigenvalue of this set of equations [43].

The current mechanism, found in the Appendix, is not complete at the time of this writing; however, it is still an improvement on the existing LLNL model and worthy of discussion. Table 3 shows the mechanism additions focusing on CH₃OPO, which has previously been identified as an intermediate in DMMP combustion through laser photoionization of a premixed flame seeded with DMMP [44]. CH₃OPO is present in the LLNL model but is only considered in radical decomposition reactions; however, the addition of the species CH₂OPO and its reactions is entirely new.

Table 3. New CH₃OPO and CH₂OPO reactions valid at 1 atm and 500 – 2500 K.

Reaction	A [mol, cm, s, K]	b	E _a [cal/mol]
CH ₃ OPO ⇌ H+CH ₂ OPO	1.105×10 ³⁷	-7.840	107755.4
CH ₃ OPO ⇌ CH ₃ O+PO	4.186×10 ⁵²	-12.255	122309.3
CH ₃ OPO ⇌ CH ₃ +PO ₂	1.046×10 ⁴³	-8.599	82114.2
CH ₃ OPO ⇌ CH ₂ O+HPO	3.185×10 ³³	-6.184	67917.6
CH ₂ OPO+H ⇌ CH ₃ +PO ₂	8.382×10 ¹⁴	-0.452	701.2
CH ₂ OPO+H ⇌ CH ₂ O+HPO	5.773×10 ¹²	0.058	-299.9
CH ₃ OPO+H ⇌ CH ₂ OPO+H ₂	7.061×10 ⁵	2.616	7142.8
CH ₃ OPO+CH ₃ ⇌ CH ₂ OPO+CH ₄	3.832×10 ⁻¹	3.817	8673.2
CH ₃ OPO+OH ⇌ CH ₂ OPO+H ₂ O	2.453×10 ⁻¹	3.799	-1671.5
CH ₂ OPO ⇌ CH ₂ O+PO	3.532×10 ³²	-6.213	39043.7

In the LLNL mechanism, DMP was only important as an intermediate species; however, in the present study which is being compared to DMP and TMP data, the initial reactions of DMP are of particular interest because the unimolecular decomposition reactions and other reactions involving the parent molecule will greatly affect ignition delay times. Some of the reactions that fall into this category are given in Table 4.

Table 4. DMP unimolecular decomposition, H abstraction, and radical decomposition reactions valid at 1 atm and 500 – 2500 K.

Reaction	A [mol, cm, s, K]	b	E _a [cal/mol]
$\text{PO}[\text{H}][\text{OME}]_2 \rightleftharpoons \text{CH}_3 + \text{PO}[\text{H}][\text{OME}]\text{O}$	8.872×10^{51}	-10.573	111864.6
$\text{PO}[\text{H}][\text{OME}]_2 \rightleftharpoons \text{CH}_3\text{O} + \text{PO}[\text{H}][\text{OME}]$	1.414×10^{77}	-17.704	149735.0
$\text{PO}[\text{H}][\text{OME}]_2 \rightleftharpoons \text{H} + \text{PO}[\text{H}][\text{OME}][\text{OCH}_2]$	7.158×10^{69}	-15.526	138909.5
$\text{PO}[\text{H}][\text{OME}]_2 \rightleftharpoons \text{H} + \text{PO}[\text{OME}]_2$	1.067×10^{56}	-11.620	120083.4
$\text{PO}[\text{H}][\text{OME}]_2 \rightleftharpoons \text{CH}_3\text{OH} + \text{CH}_3\text{OPO}$	4.364×10^{33}	-5.949	84495.4
$\text{PO}[\text{H}][\text{OME}]_2 \rightarrow \text{CH}_2\text{O} + \text{H}_2 + \text{CH}_3\text{OPO}$	6.069×10^{37}	-7.204	95816.8
$\text{PO}[\text{H}][\text{OME}] \rightleftharpoons \text{CH}_3 + \text{HPO}_2$	4.059×10^{12}	0.450	36718.0
$\text{PO}[\text{H}][\text{OME}] \rightleftharpoons \text{H} + \text{CH}_3\text{OPO}$	8.854×10^{12}	0.590	28813.0
$\text{PO}[\text{H}][\text{OME}]\text{O} \rightleftharpoons \text{H} + \text{CH}_3\text{OPO}_2$	6.232×10^{12}	0.400	21083.0
$\text{PO}[\text{H}][\text{OME}]_2 + \text{H} \rightleftharpoons \text{PO}[\text{H}][\text{OME}][\text{OCH}_2] + \text{H}_2$	3.858×10^6	2.502	7179.9
$\text{PO}[\text{H}][\text{OME}]_2 + \text{H} \rightleftharpoons \text{PO}[\text{OME}]_2 + \text{H}_2$	2.447×10^7	1.972	4242.2
$\text{PO}[\text{H}][\text{OME}]_2 + \text{CH}_3 \rightleftharpoons \text{PO}[\text{H}][\text{OME}][\text{OCH}_2] + \text{CH}_4$	3.457×10^0	3.688	9820.2
$\text{PO}[\text{H}][\text{OME}]_2 + \text{CH}_3 \rightleftharpoons \text{PO}[\text{OME}]_2 + \text{CH}_4$	7.804×10^1	3.037	5237.0
$\text{PO}[\text{H}][\text{OME}]_2 + \text{OH} \rightleftharpoons \text{PO}[\text{H}][\text{OME}][\text{OCH}_2] + \text{H}_2\text{O}$	2.441×10^6	2.184	58.8
$\text{PO}[\text{H}][\text{OME}]_2 + \text{OH} \rightleftharpoons \text{PO}[\text{OME}]_2 + \text{H}_2\text{O}$	4.208×10^5	2.180	69.3
$\text{PO}[\text{H}][\text{OME}][\text{OCH}_2] \rightleftharpoons \text{PO}[\text{OME}]_2$	1.002×10^{43}	-9.534	41422.3
$\text{PO}[\text{H}][\text{OME}][\text{OCH}_2] \rightleftharpoons \text{CH}_2\text{O} + \text{PO}[\text{H}][\text{OME}]$	1.040×10^{36}	-7.132	46540.2
$\text{PO}[\text{OME}]_2 \rightleftharpoons \text{CH}_3 + \text{CH}_3\text{OPO}_2$	2.473×10^{44}	-9.328	54071.6
$\text{PO}[\text{OME}]_2 \rightleftharpoons \text{CH}_3\text{O} + \text{CH}_3\text{OPO}$	8.444×10^{44}	-9.629	55786.1
$\text{PO}[\text{OME}]_2 \rightleftharpoons \text{CH}_2\text{O} + \text{PO}[\text{H}][\text{OME}]$	4.345×10^{60}	-14.306	72892.3
$\text{PO}[\text{H}][\text{OME}][\text{OCH}_2] \rightleftharpoons \text{CH}_3 + \text{CH}_3\text{OPO}_2$	9.719×10^{50}	-11.223	58099.0
$\text{PO}[\text{H}][\text{OME}][\text{OCH}_2] \rightleftharpoons \text{CH}_3\text{O} + \text{CH}_3\text{OPO}$	2.050×10^{50}	-11.184	58691.1

Previously, DMP was only present in 5 reactions: 3 radical decomposition and 2 unimolecular decomposition reactions (one of which proceeds backwards). The activation energies vary tremendously for the reactions in common between the current study and

the LLNL mechanism. For example, $\text{PO}[\text{H}][\text{Ome}]_2 \rightleftharpoons \text{CH}_3\text{OH} + \text{CH}_3\text{OPO}$ has a new E_a of 84495 cal/mol, and its previous value was 46000 cal/mol. $\text{PO}[\text{H}][\text{Ome}]$, $\text{PO}[\text{H}][\text{Ome}]\text{O}$, and $\text{PO}[\text{H}][\text{Ome}][\text{OCH}_2]$ are all newly included species. Many of these missing reactions are important for the phosphorus family that contains both a hydrogen and an oxygen atom bonded directly to the central phosphorus atom (like DMP and DEP), but the more basic phosphorus-containing reactions are valuable for all OPCs.

The reaction rate coefficients given in Table 3 and Table 4 are specifically for 1 atm, but additional details for other pressures can be found in the mechanism, provided in the Appendix. Ignition delay time comparisons to the experimental data shown in Chapter IV and to the LLNL mechanism are provided in V.4 Model Comparisons.

V.4 Model Comparisons

All model predictions were calculated using Chemkin's closed homogeneous reactor with a problem type of "constrain volume and solve energy equation." This reactor solves the transient problem with time steps of 1 μs up to 2500 ms. To determine the ignition delay time, OH^* is set as an output and used in a Matlab script that calculates and extrapolates the steepest slope. This process is performed to match the experimental definition of ignition delay time.

The three models compared were the LLNL model, the LLNL OPC submechanism with the AramcoMech 2.0 hydrocarbon mechanism, and an expanded and modified version of the previous mechanism. The LLNL mechanism does not include an OH^* submechanism and therefore the Kathrotia et al. [45] OH^* submechanism was included to

obtain the OH* species. The OH* submechanism should have a negligible effect on the model as the OH* species are only present in extremely small concentrations, $x_{OH^*} \approx 10^{-11}$. The LLNL model with AramcoMech 2.0 is included as an attempt to more fairly compare any OPC modifications made to the original LLNL mechanism, while also using the most up-to-date version of AramcoMech in the updated mechanism. The ignition delay times were not calculated for the neat mixtures using the updated mechanism of the current study because they would be exactly the same as the LLNL model with AramcoMech 2.0 results. The hydrogen experiments of Chapter IV.3, modeled using the above procedure, are shown in Figure 30.

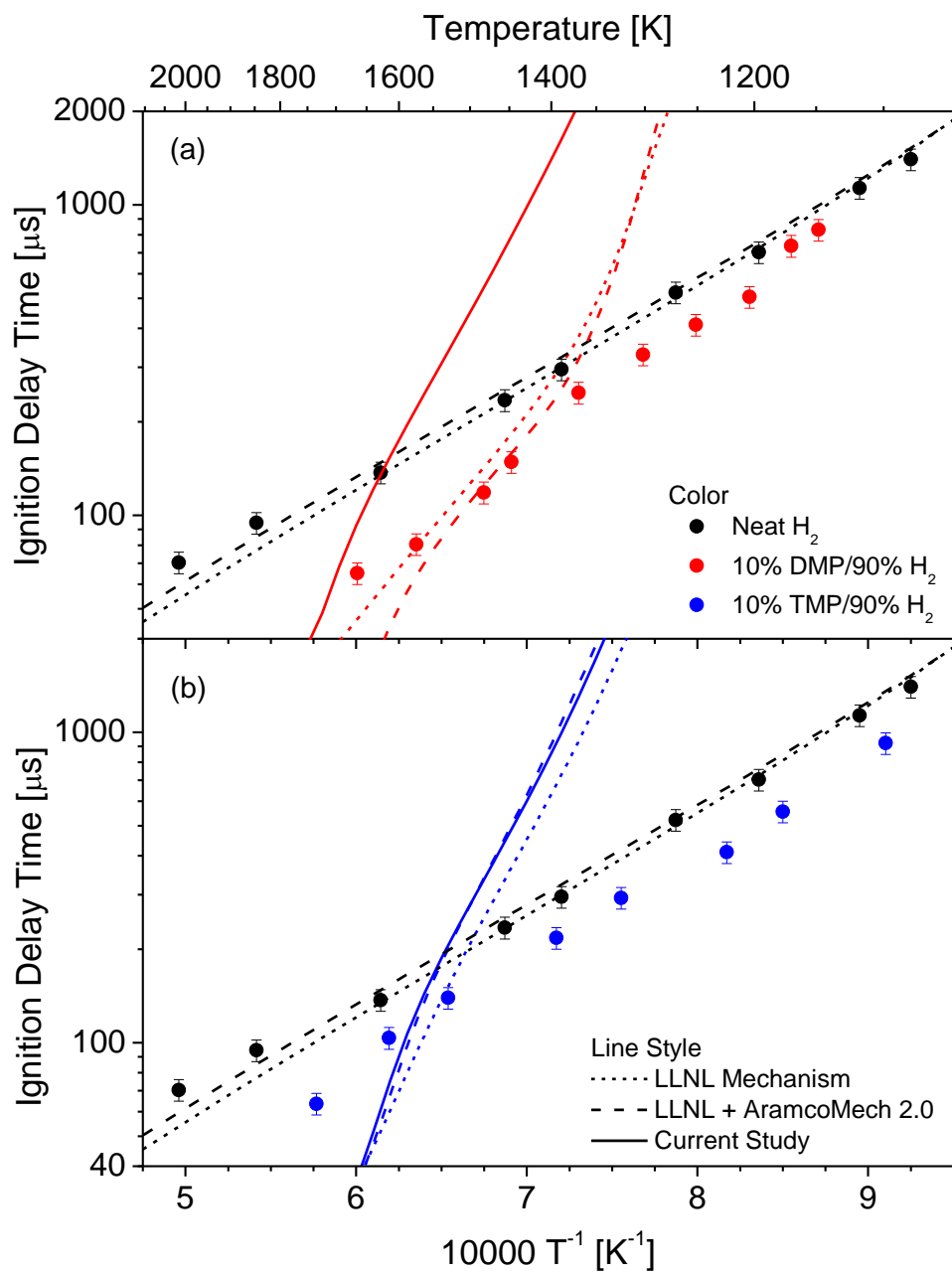


Figure 30. Hydrogen based ignition delay time modeling comparison ($\phi = 0.5$, 1 atm, diluted with 98% argon).

Both Figure 30a and Figure 30b contain the same neat hydrogen ignition delay times, and both versions of the LLNL and the LLNL + AramcoMech 2.0 do a good job of

predicting the ignition delay time experimental data. Unsurprisingly, the AramcoMech 2.0 version does a slightly better job of matching the experimental values. The OPC predictions, on the other hand, have some deficiencies. The TMP results, Figure 30(b), differ between the LLNL models, and this is purely an effect of the updated hydrocarbon data. The LLNL with AramcoMech 2.0 and the current study's mechanism are quite similar. This good agreement is entirely expected because other than the updated CH_3OPO reactions, all of the efforts have been put into DMP reactions. The reason for the emphasis on DMP reactions is that in the original model TMP was a targeted species, thus its decomposition reactions and other initiation and chain-branching reactions were modeled, but DMP was only an intermediate species and thus lacking for reactions that would be very important for ignition studies.

In Figure 30a, the LLNL DMP results differ from the LLNL with AramcoMech 2.0 significantly at higher temperatures, but approach one another at lower temperatures. The current mechanism is entirely different, primarily in the slope of the prediction. At first, one might think that the results of the current model are worse, but they are actually an improvement. The reason is that there is little difference in the experimental data between DMP and TMP, so one would expect the model predictions to be very similar to one another. In the LLNL mechanisms, the overall slope of the ignition delay time trends are very different from one another, but in the current mechanism, they are quite similar to one another. This aspect is further demonstrated by plotting just the DMP and TMP results together, Figure 31.

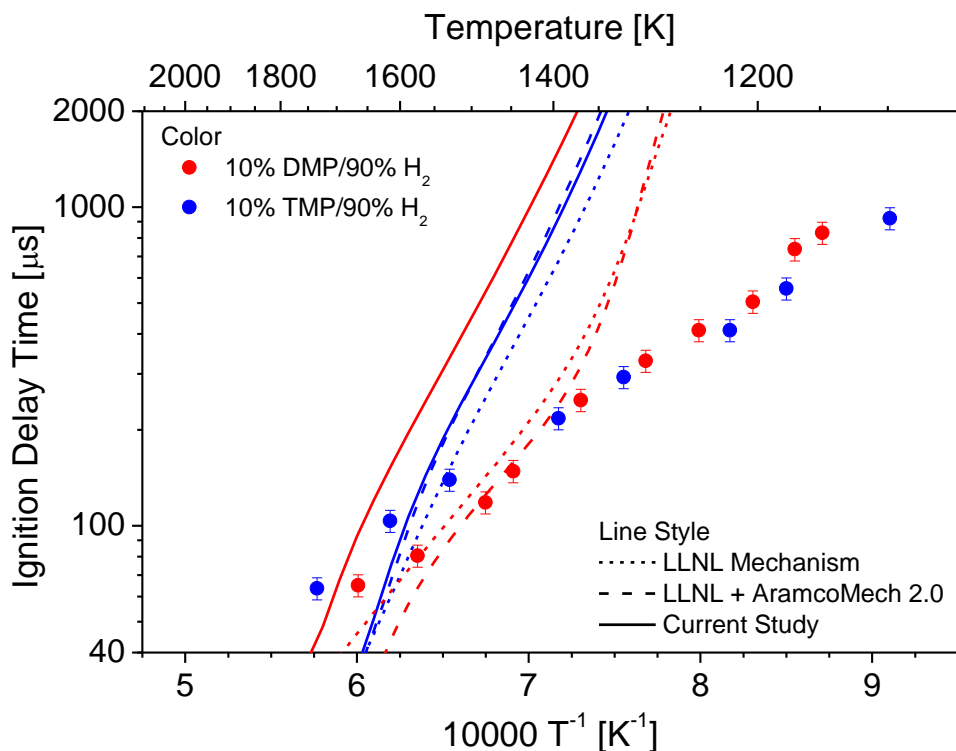


Figure 31. Direct comparison of hydrogen DMP and TMP ignition delay time modeling ($\phi = 0.5$, 1 atm, diluted with 98% argon).

In Figure 31, it becomes clearer that in the previous OPC mechanism, there are significant differences in the ignition-important reactions between the two OPCs. It is believed that since more effort is put into the initial initiation and chain-branching reactions of DMP that the current model is a better representation of the DMP ignition delay times. It shows progress that the two species' shapes are qualitatively similar to each other. There is obviously some additional work to be performed so that the two curves will better predict the experimental ignition delay times, but the current efforts do improve upon some of the deficiencies of the previous OPC model. The OPC/hydrocarbon chemistry interactions are explored in Figure 32 through the modeling of DMP with C_2H_4 .

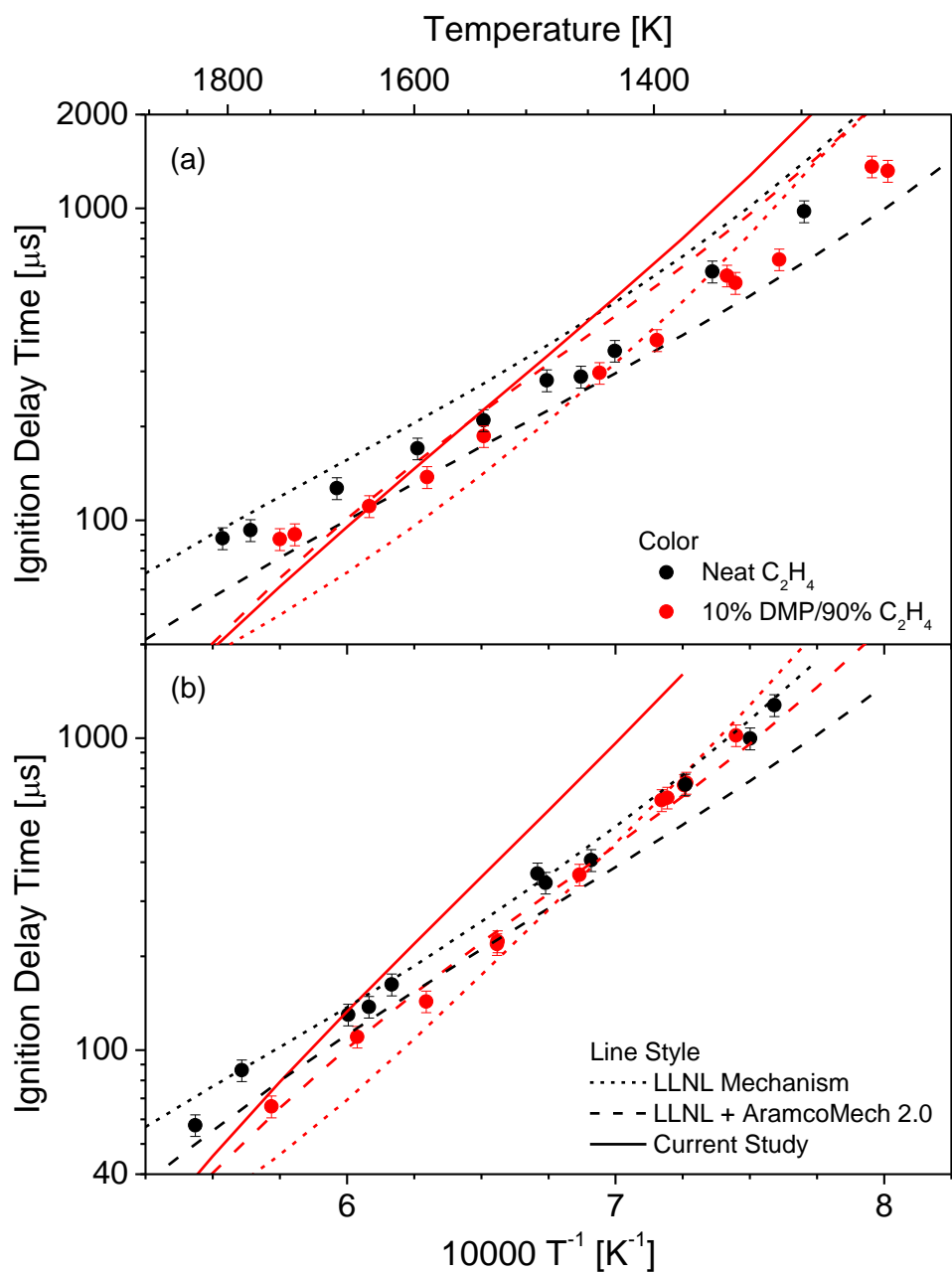


Figure 32. 10% DMP/90% ethylene ignition delay times at (a) $\phi = 0.5$ and (b) $\phi = 1.0$, 1 atm, diluted with 98% argon. ICARE T_5 uncertainty is estimated to be 1%.

For both $\phi = 0.5$ and 1.0 , the AramcoMech 2.0 predicts a faster ignition delay time than that seen in the experiments, Figure 32. There is also a fairly significant difference between the LLNL's hydrocarbon base mechanism. For the DMP, there is once again a significant difference between the two versions of the LLNL mechanism. All of the mechanisms do a better job at predicting the ignition delay time compared to the hydrogen experiments. Similar to the hydrogen results, the predicted slope does not match the experimental data for either $\phi = 0.5$ or 1.0 . For both equivalence ratios, the results are closer at higher temperatures and then diverge from the experimental results as the temperature decreases. The TMP/ethylene results can be found in the Appendix. They were not included because, like the hydrogen modeling, there is not a large difference between the LLNL with AramcoMech 2.0 and the current mechanism. To gain further insight into the discrepancies between model and experiment, the OH^* profiles of each are normalized and plotted on Figure 33 for both hydrogen and ethylene DMP mixtures.

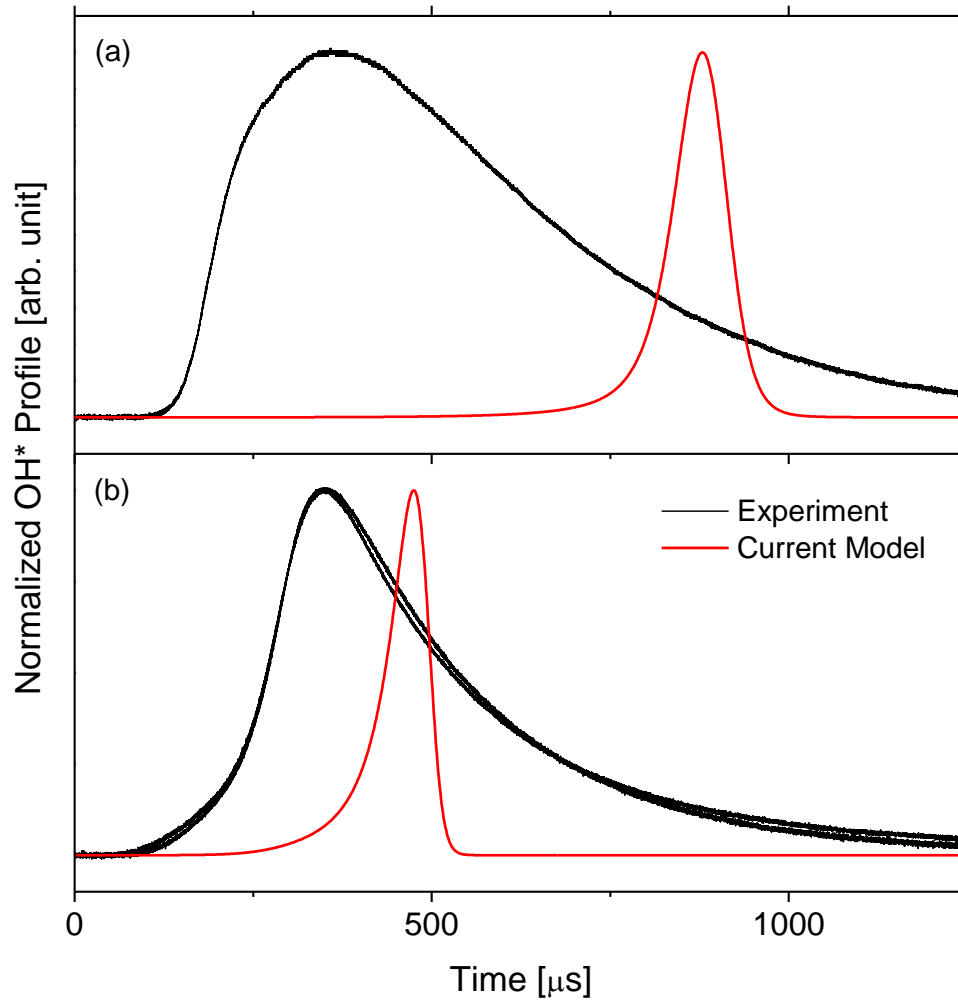


Figure 33. Experimental and model OH* profiles for (a) 10% DMP/ 10% H_2 $\phi = 0.5$, 1447 K, 1.03 atm and (b) 10% DMP/ 90% C_2H_4 $\phi = 1.0$, 1524.5 K, 1.05 atm.

Figure 33a shows the OH* profile of a DMP/hydrogen experiment. The shape of the experimental OH* profile is very broad, but the model predicts a sharp peak. As expected from Figure 30, the ignition time is also significantly different. The OH* profiles of Figure 33b, DMP/ethylene, are much closer in shape and appear to only be shifted from one another up to the peak, but after the peak, the model-predicted OH* profile drops off

dramatically. There is still work to be done in both predicting the overall ignition delay time and the species profiles, namely OH*, but the overall direction of these modeling efforts appear promising. With more improvements, it looks hopeful that an accurate, simple OPC model can be developed.

V.5 References

- [1] T.M. Jayaweera, C.F. Melius, W.J. Pitz, C.K. Westbrook, O.P. Korobeinichev, V.M. Shvartsberg, A.G. Shmakov, I.V. Rybitskaya, H.J. Curran, Flame inhibition by phosphorus-containing compounds over a range of equivalence ratios, *Combust. Flame* 140 (2005) 103-115.
- [2] W. Kan, H. Zhong, H.T. Yu, Theoretical prediction regarding structural and thermodynamical characteristics of stable CH₃PO₂ isomers and unimolecular decomposition mechanisms of species CH₃P(=O)₂, CH₃O-P=O, and CH₂=P(=O)OH, *J. Comput. Chem.* 30 (2009) 2334-50.
- [3] O.V. Dorofeeva, N.F. Moiseeva, Computational study of the thermochemistry of organophosphorus(III) compounds, *J. Phys. Chem. A* 110 (2006) 8925-8932.
- [4] N.L. Haworth, G.B. Bacskay, J.C. Mackie, The role of phosphorus dioxide in the H + OH recombination reaction: Ab initio quantum chemical computation of thermochemical and rate parameters, *J. Phys. Chem. A* 106 (2002) 1533-1541.
- [5] K. Hemelsoet, F. Van Durme, V. Van Speybroeck, M.-F. Reyniers, M. Waroquier, Bond dissociation energies of organophosphorus compounds: An assessment of contemporary ab initio procedures, *J. Phys. Chem. A* 114 (2010) 2864-2873.
- [6] P.A. Sullivan, R. Sumathi, W.H. Green, J.W. Tester, Ab initio modeling of organophosphorus combustion chemistry, *Phys. Chem. Chem. Phys.* 6 (2004) 4296-4309.
- [7] A. Khalfa, M. Ferrari, R. Fournet, B. Sirjean, L. Verdier, P.A. Glaude, Quantum chemical study of the thermochemical properties of organophosphorous compounds, *J. Phys. Chem. A* 119 (2015) 10527-10539.
- [8] J.A.M. Jr., M.J. Frisch, J.W. Ochterski, G.A. Petersson, A complete basis set model chemistry. VII. Use of the minimum population localization method, *J. Chem. Phys.* 112 (2000) 6532-6542.

- [9] A.G. Baboul, L.A. Curtiss, P.C. Redfern, K. Raghavachari, Gaussian-3 theory using density functional geometries and zero-point energies, *J. Chem. Phys.* 110 (1999) 7650-7657.
- [10] L.A. Curtiss, P.C. Redfern, K. Raghavachari, J.A. Pople, Gaussian-3X (G3X) theory: Use of improved geometries, zero-point energies, and Hartree–Fock basis sets, *J. Chem. Phys.* 114 (2001) 108-117.
- [11] G. da Silva, G3X-K theory: A composite theoretical method for thermochemical kinetics, *Chem. Phys. Lett.* 558 (2013) 109-113.
- [12] D.J. Henry, M.B. Sullivan, L. Radom, G3-RAD and G3X-RAD: Modified Gaussian-3 (G3) and Gaussian-3X (G3X) procedures for radical thermochemistry, *J. Chem. Phys.* 118 (2003) 4849-4860.
- [13] G.P.F. Wood, L. Radom, G.A. Petersson, E.C. Barnes, M.J. Frisch, J.A.M. Jr., A restricted-open-shell complete-basis-set model chemistry, *J. Chem. Phys.* 125 (2006) 094106.
- [14] K. Lolders, Revised thermochemical properties of phosphinidene (PH), phosphine (PH₃), phosphorus nitride (PN), and magnesium phosphate (Mg₃P₂O₈), *J. Phys. Chem. Ref. Data* 28 (1999) 1705-1712.
- [15] M.W. Chase, NIST-JANAF Thermochemical Tables, American Institute of Physics, Woodbury, N.Y., 1998.
- [16] P.C. Jordan, Lower electronic levels of the radicals PH and PH₂, *J. Chem. Phys.* 41 (1964) 1442-1449.
- [17] L.V. Gurvich, I.V. Veyts, C.B. Alcock, Thermodynamic properties of individual substances, Hemisphere Pub. Corp., New York :, 1989.
- [18] J.D. Cox, D.D. Wagman, V.A. Medvedev, CODATA key values for thermodynamics, Hemisphere Pub. Corp., New York :, 1989, xiii, 271 pages ; 26 cm.
- [19] Y.-R. Luo, Comprehensive handbook of chemical bond energies, CRC Press, Boca Raton :, 2007, 1655 pages : illustrations ; 27 cm.
- [20] J. Berkowitz, G.B. Ellison, D. Gutman, Three methods to measure RH bond energies, *J. Phys. Chem.* 98 (1994) 2744-2765.

- [21] S.R. Gunn, L.G. Green, The heats of formation of some unstable gaseous hydrides, *J. Phys. Chem.* 65 (1961) 779-783.
- [22] K.A. Gingerich, Gaseous phosphorus compounds. III. Mass spectrometric study of the reaction between diatomic nitrogen and phosphorus vapor and dissociation energy of phosphorus mononitride and diatomic phosphorus, *J. Phys. Chem.* 73 (1969) 2734-2741.
- [23] R.L. Potter, V.N. DiStefano, Thermodynamic functions of some phosphorus compounds, *J. Phys. Chem.* 65 (1961) 849-855.
- [24] A.G. Gaydon, Dissociation energies and spectra of diatomic molecules, Chapman & Hall, London, 1968, xiii, 330 pages 4 plates, illustrations 23 cm.
- [25] D.L. Hildenbrand, K.H. Lau, Thermochemical properties of gaseous POBr and some H-P-O species, *J. Chem. Phys.* 100 (1994) 8373-8376.
- [26] F.R. Hartley, The chemistry of organophosphorus compounds, Wiley, Chichester [England] ;, 1990, 4 volumes : illustrations ; 24 cm.
- [27] I. Rabinovich, V. Nistratov, V. Tel'noi, M. Sheiman, Termodinamika metalloorganicheskikh soedinenii [Thermodynamics of organometallic compounds], Nizhny Novgorod: Publishing house of Nizhegor. University (1996).
- [28] H.M.A. Al-Maydama, A. Finch, P.J. Gardner, A.J. Head, The enthalpies of formation of bis(dimethylamino)cyanophosphine, (dimethylamino)dicyanophosphine, and tricyanophosphine, *J. Chem. Thermodyn.* 27 (1995) 575-584.
- [29] R.H. Davies, A. Finch, P.J. Gardner, A. Hameed, M. Stephens, The standard enthalpies of hydrolysis and formation of tricyanophosphine, *J. Chem. Soc., Dalton Trans.* (1976) 556-558.
- [30] Y.R. Luo, S.W. Benson, A new electronegativity scale for the correlation of heats of formation. 2. The differences in heats of formation between hydrogen and methyl derivatives, *J. Am. Chem. Soc.* 111 (1989) 2480-2482.
- [31] C.L. Tien, J.H. Lienhard, Statistical thermodynamics, Holt, Rinehart, and Winston, 1971.
- [32] D.A. McQuarrie, Statistical thermodynamics, University Science Books, Mill Valley, California, 1973.

- [33] S. Sharma, M.R. Harper, W.H. Green CanTherm. <http://github.com/GreenGroup/RMG-Py>.
- [34] C.W. Gao, J.W. Allen, W.H. Green, R.H. West, Reaction Mechanism Generator: Automatic construction of chemical kinetic mechanisms, Comput. Phys. Commun. 203 (2016) 212-225.
- [35] A. Burcat, B. Ruscic, Chemistry, T.-I.I.o. Tech., Third millenium ideal gas and condensed phase thermochemical database for combustion (with update from active thermochemical tables), Report No. 2005.
- [36] R. Chang, Theories of Reaction Rates in: Physical chemistry for the biosciences, University Science, Sansalito, Calif. :, 2005.
- [37] G.H. Duffey, Reaction Rate Theory in: Modern Physical Chemistry: A Molecular Approach, Springer US, Boston, MA, 2000, pp. 487-508.
- [38] H. Eyring, The Activated Complex in Chemical Reactions, J. Chem. Phys. 3 (1935) 107-115.
- [39] J.R. Barker, T.L. Nguyen, J.F. Stanton, C. Aieta, M. Ceotto, F. Gabas, T.J.D. Kumar, L.L.L. C. G. L. Li, A. Maranzana, N. F. Ortiz, J. M. Preses, J. M. Simmie, J. A. Sonk, and P. J. Stimac MultiWell-2017 Software Suite. <http://clasp-research.engin.umich.edu/multiwell>.
- [40] B.J. R., Multiple-Well, multiple-path unimolecular reaction systems. I. MultiWell computer program suite, Int. J. Chem. Kinet. 33 (2001) 232-245.
- [41] B.J. R., Energy transfer in master equation simulations: A new approach, Int. J. Chem. Kinet. 41 (2009) 748-763.
- [42] D.R. Glowacki, C.-H. Liang, C. Morley, M.J. Pilling, S.H. Robertson, MESMER: An Open-Source Master Equation Solver for Multi-Energy Well Reactions, The Journal of Physical Chemistry A 116 (2012) 9545-9560.
- [43] R.A. Marcus, Unimolecular Dissociations and Free Radical Recombination Reactions, The Journal of Chemical Physics 20 (1952) 359-364.
- [44] J.H. Werner, T.A. Cool, Flame sampling photoionization mass spectrometry of CH₃PO₂ and CH₃OPO₂, Chem. Phys. Lett. 275 (1997) 278-282.
- [45] T. Kathrotia, M. Fikri, M. Bozkurt, M. Hartmann, U. Riedel, C. Schulz, Study of the H+O+M reaction forming OH*: Kinetics of OH* chemiluminescence in hydrogen combustion systems, Combust. Flame 157 (2010) 1261-1273.

CHAPTER VI

CONCLUSIONS

The OPCs DMP, DEP, TMP, DMMP, DEMP, DIMP, and TEP have all been experimentally tested to determine fundamental chemical properties, namely laminar flame speed and ignition delay time. It has been demonstrated that the effect of the OPCs DMMP, DEMP, DIMP, and TEP is to act as a flame suppressant on parent mixtures of hydrogen/air and methane/air at 1 atm and 120 °C by measuring their laminar flame speeds with an optical, spherically expanding laminar flame speed experiment. For methane/air, the OPCs all have similar suppression effects and serve to broaden the laminar flame speed curves in ϕ space while simultaneously decreasing the flame speed by about 30%. In the hydrogen/air experiments, the OPCs differentiate themselves and have an increasing suppression effect with both equivalence ratio and carbon moiety. The suppression effect for DMMP, which was investigated at both 0.1% and 0.3% of the total volume, is decreasingly effective for methane/air while remaining a linear decrease for hydrogen/air over the range of mixtures studied herein. For both parent fuels, the OPCs flame speed reduction was particularly notable at near-stoichiometric and fuel rich conditions, but again their effect on the parent fuels differentiates them by having more of a suppression effect on the fuel lean side for methane than for hydrogen. DIMP has a linear suppression effect between the 0 – 0.4% of the total volume. The Glaude et al. [1] model which contains DIMP was found to be relatively close for hydrogen mixtures, but there are some severe deficiencies for methane mixtures. In a qualitative comparison, 0.5% TEP has as

much of a flame speed decrease as 1% of Halon 1301, and 0.1% of OPCs is comparable to 1% of two other Halon 1301 replacements that have been previously studied. A sensitivity analysis has agreed with the primary inhibition mechanism discussed in Jayaweera et al. [2], but HOPO + O reactions are found to be more important than suggested previously.

Ignition delay time experiments have been performed with the OPCs DMP, DEP, and TEP in hydrogen and ethylene mixtures. It has been found that all of these simple OPCs act to decrease ignition delay times. In most cases, they do decrease the ignition delay time indistinguishably from one another. There is an odd feature found in the OH* profiles of some of the ignition delay time experiments, but it has been determined to be a feature of ethylene ignition. Additional experiments have been performed to test the effect of DEP and TEP separate from the fuels by replacing hydrogen from the experiments with additional argon. When doing this, TEP becomes extremely reactive, igniting even before the reflected shock wave. DEP tests show an increase in ignition delay time compared to the DEP/H₂ experiments.

Finally, efforts to improve the LLNL OPC mechanism included updating its hydrocarbon base mechanism to AramcoMech 2.0 and, more importantly, performing quantum chemistry modeling to add reaction pathways and update OPC thermochemistry with a focus on the OPCs DMP and TMP. The heats of formation have been carefully recalculated using the quantum chemistry composite method ROCBS-QB3 with bond additivity corrections based on a thorough literature review of experimental values of phosphorus-containing species. The rest of the thermochemical properties have been

calculated with a B3LYP/6-311g(2d,d,p) level of theory, compiled with Cantherm, and fit to NASA polynomials using a custom fitting routine. The revised thermochemistry has been found to be improvement based on discrepancies found in the LLNL OPC thermochemistry. The reaction pathways have focused on reactions important to DMP ignition and CH_3OPO reactions. These calculations have been performed using transition state theory at a G3X-K level of theory using a hindered rotor correction. A G3X-K level of theory is necessary to find many of the OPC transition states. These modeling efforts are an ongoing effort, but the current version has been compared with the ignition delay time data obtained herein.

The current model has been shown to be an improvement on the previous OPC mechanism. This conclusion is primarily based on the TMP and DMP experimental data sets closely matching one another, but the previous OPC mechanism predicted that the two species would not be similar; whereas, the current model predicts them to have a very similar slope. The current model does not satisfactorily model the ignition delay time data, but the current results are promising.

In the future, more effort will be put into expanding the current model and hopefully getting it to a state in which it can accurately predict DMP and TMP ignition delay times. As for laminar flame speed, it is possible that the loss of relative effectiveness at larger relative quantities of OPCs could be detrimental to their use as fire suppressants and should be investigated further. Additionally, it would be beneficial to test TMP, DMP or DEP so that the future model could also be validated with laminar flame speed data.

Future shock-tube studies should try to take direct phosphorus compound measurements so that future mechanisms can be improved with specific species' time histories.

These data will be used to further develop previously existing chemical kinetics mechanisms with the hope that such models can be used to further develop OPCs as the next step in fire suppression technology. The developed kinetics mechanisms will also be a great boon to those interested in the destruction of dangerous OPCs such as Sarin.

VI.1 References

- [1] P.A. Glaude, C. Melius, W.J. Pitz, C.K. Westbrook, Detailed chemical kinetic reaction mechanisms for incineration of organophosphorus and fluoroorganophosphorus compounds, *Proc. Combust. Inst.* 29 (2002) 2469-2476.
- [2] T.M. Jayaweera, C.F. Melius, W.J. Pitz, C.K. Westbrook, O.P. Korobeinichev, V.M. Shvartsberg, A.G. Shmakov, I.V. Rybitskaya, H.J. Curran, Flame inhibition by phosphorus-containing compounds over a range of equivalence ratios, *Combust. Flame* 140 (2005) 103-115.

APPENDIX

A.1 Markstein Length Plots

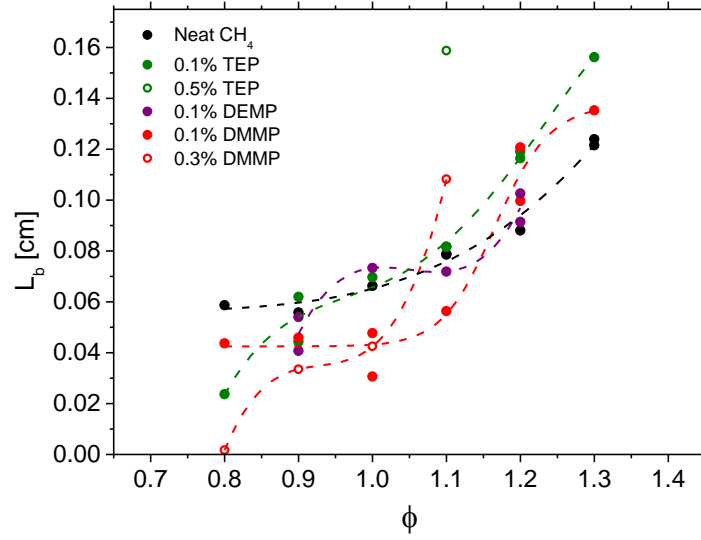


Figure A-1. Burned Markstein lengths of OPCs in methane/air mixture at 1 atm, 120 °C. Dashed lines represent experimental fits.

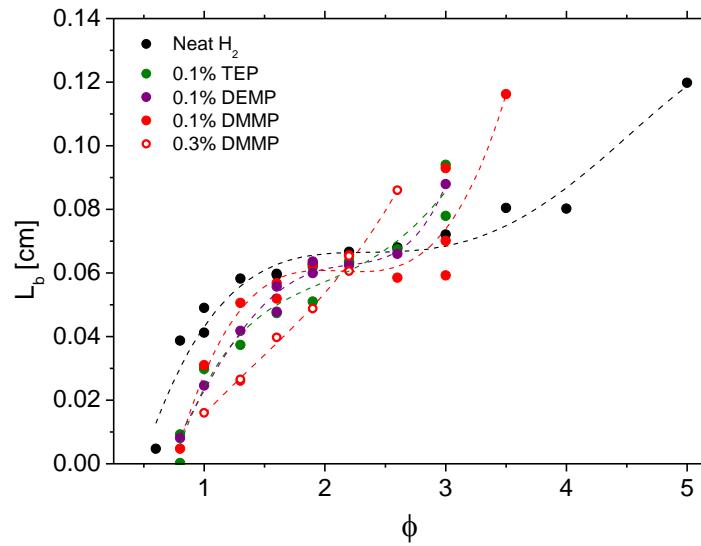


Figure A-2. Burned Markstein lengths of OPCs in hydrogen/air mixture at 1 atm, 120 °C. Dashed lines represent experimental fits.

A.2 Laminar Flame Speed Sensitivity Plots

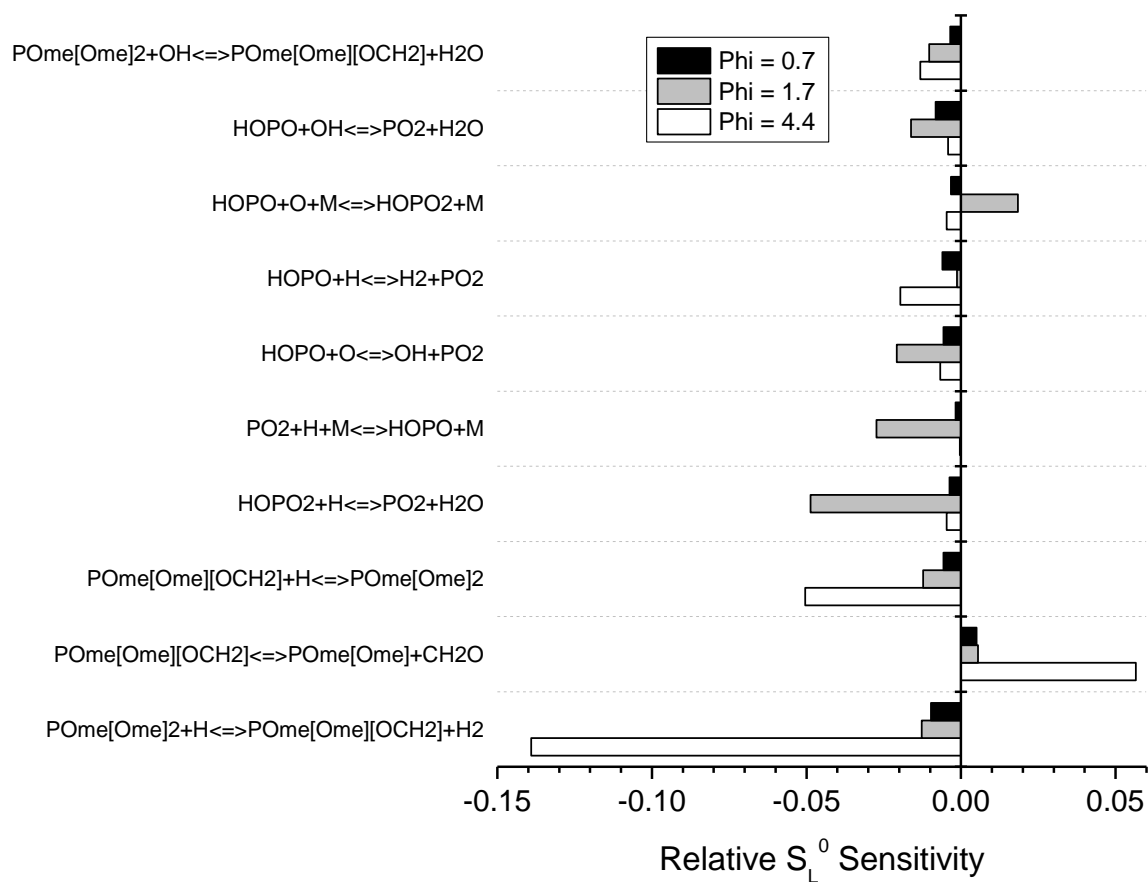


Figure A-3. Top 10 OPC reactions of 0.1% DMMP/H₂/air relative laminar flame speed sensitivity at 1 atm, 120 °C.

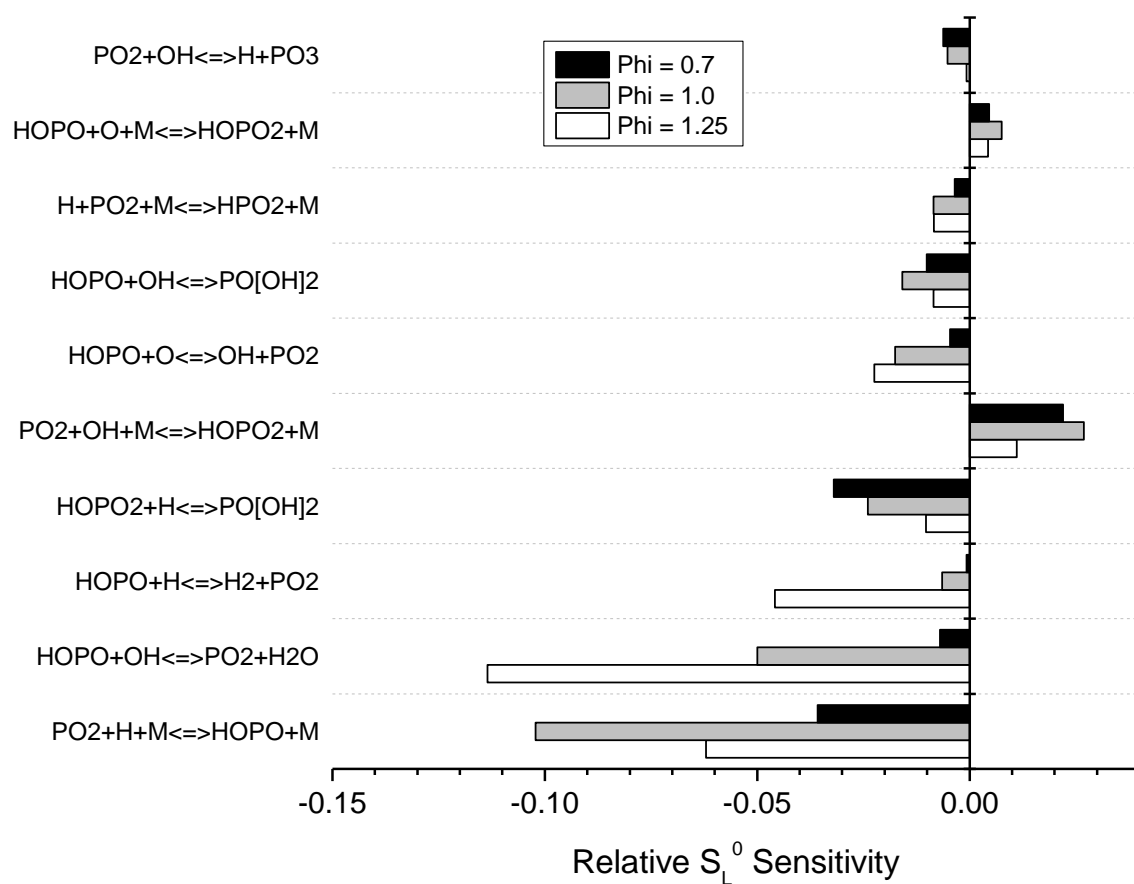


Figure A-4. Top 10 OPC reactions of 0.1% DIMP/CH₄/air relative laminar flame speed sensitivity at 1 atm, 120 °C.

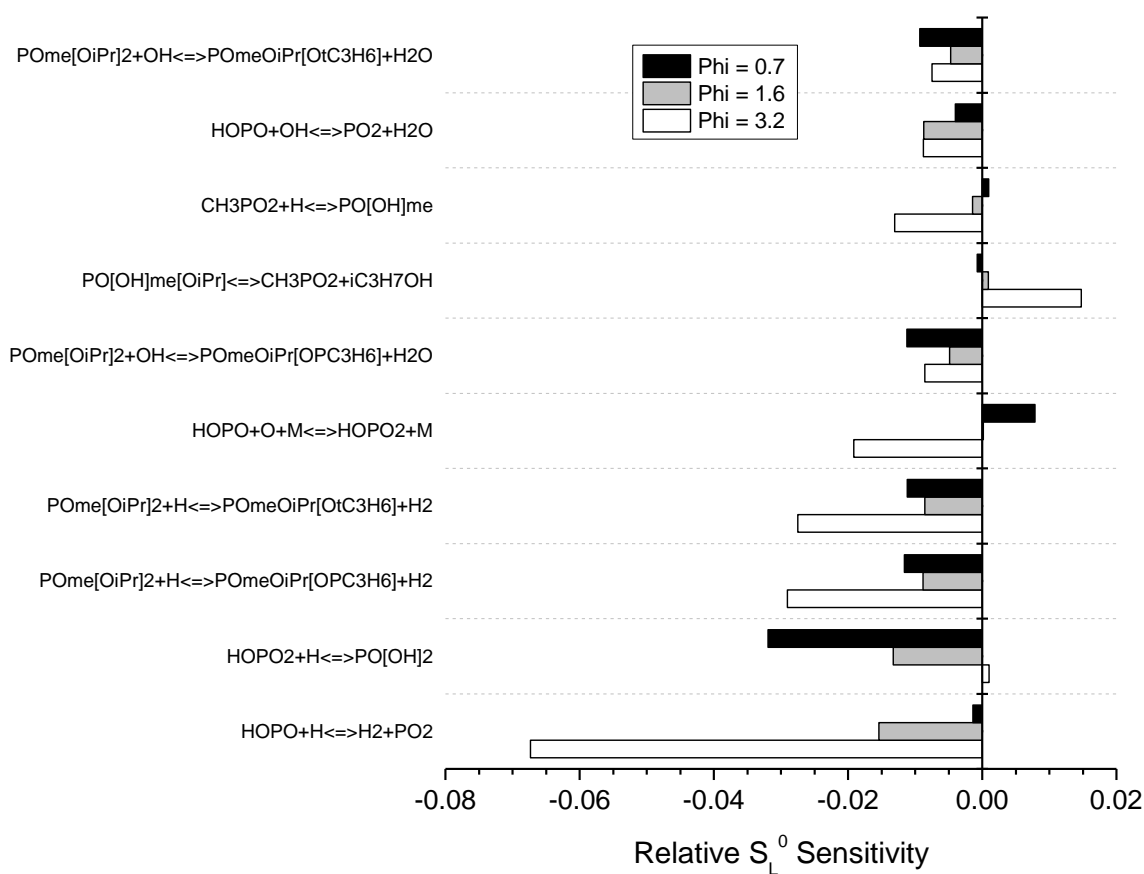


Figure A-5. Top 10 OPC reactions of 0.1% DIMP/H₂/air relative laminar flame speed sensitivity at 1 atm, 120 °C.

A.3 CH₄ Flame Speed Data Tables

Table A-1. Laminar flame speed data for neat CH₄/air.

ϕ	Temp. [°C]	Unburned Density [kg/m ³]	Burned Density [kg/m ³]	S_b^0 [cm/s]	S_L^0 [cm/s]	$S_{L,RC}^0$ [cm/s]	L_b [cm]
0.8	120.3	0.863	0.164	208.3	39.6	40.3	0.059
0.9	120.3	0.859	0.154	272.7	48.7	49.4	0.056
1.0	120.9	0.855	0.147	314.8	54.0	54.6	0.066
1.1	120.8	0.851	0.145	320.5	54.5	55.1	0.079
1.1	120.3	0.853	0.145	322.7	54.8	55.4	0.079
1.2	119.1	0.852	0.146	288.4	49.6	50.2	0.088
1.3	120.0	0.847	0.149	243.5	42.8	43.4	0.122
1.3	120.4	0.846	0.149	243.5	42.8	43.4	0.124

Table A-2. Laminar flame speed data for TEP/CH₄/air.

% TEP	ϕ	Temp. [°C]	Unburned Density [kg/m ³]	Burned Density [kg/m ³]	S_b^0 [cm/s]	S_L^0 [cm/s]	$S_{L,RC}^0$ [cm/s]	L_b [cm]
0.1	0.8	119.7	0.864	0.164	143.4	27.2	27.9	0.024
0.1	0.9	120.5	0.859	0.154	188.8	33.8	34.4	0.044
0.1	0.9	119.9	0.860	0.154	198.9	35.5	36.2	0.062
0.1	1.0	119.9	0.857	0.147	229.7	39.3	40.0	0.070
0.1	1.1	120.6	0.852	0.145	223.8	38.0	38.7	0.082
0.1	1.1	120.5	0.852	0.145	226.7	38.5	39.2	0.082
0.1	1.2	120.3	0.849	0.146	185.9	32.0	32.7	0.119
0.1	1.2	119.9	0.850	0.146	191.0	32.9	33.5	0.116
0.1	1.3	119.8	0.847	0.149	142.0	24.9	25.6	0.156
0.5	1.1	120.5	0.852	0.145	136.7	23.2	23.9	0.159

Table A-3. Laminar flame speed data for 0.1% DEMP/CH₄/air.

ϕ	Temp. [°C]	Unburned Density [kg/m ³]	Burned Density [kg/m ³]	S_b^0 [cm/s]	S_L^0 [cm/s]	$S_{L,RC}^0$ [cm/s]	L_b [cm]
0.9	120.3	0.859	0.154	196.7	35.1	35.8	0.041
0.9	119.6	0.861	0.154	204.0	36.4	37.1	0.054
1.0	120.5	0.855	0.147	238.7	40.9	41.6	0.073
1.1	120.5	0.852	0.145	241.5	41.0	41.7	0.072
1.2	119.2	0.852	0.146	197.3	33.9	34.6	0.103
1.2	119.4	0.851	0.146	200.0	34.4	35.0	0.091

Table A-4. Laminar flame speed data for DMMP/CH₄/air.

% DMMP	ϕ	Temp. [°C]	Unburned Density [kg/m ³]	Burned Density [kg/m ³]	S_b^0 [cm/s]	S_L^0 [cm/s]	$S_{L,RC}^0$ [cm/s]	L_b [cm]
0.1	0.8	119.7	0.864	0.164	145.3	27.6	28.3	0.044
0.1	0.9	120.4	0.859	0.154	200.7	35.9	36.5	0.046
0.1	1.0	120.4	0.856	0.147	226.6	38.8	39.5	0.031
0.1	1.0	120.5	0.855	0.147	232.3	39.8	40.5	0.048
0.1	1.1	120.4	0.852	0.145	230.0	39.1	39.7	0.056
0.1	1.2	120.3	0.849	0.146	213.9	36.9	37.5	0.100
0.1	1.2	119.7	0.851	0.146	213.5	36.7	37.4	0.121
0.1	1.3	120.5	0.846	0.149	168.7	29.6	30.3	0.135
0.3	0.8	120.1	0.863	0.164	98.4	18.7	19.4	0.002
0.3	0.9	120.2	0.860	0.154	133.8	23.9	24.6	0.034
0.3	1.0	120.2	0.856	0.147	158.2	27.1	27.8	0.043
0.3	1.1	120.2	0.853	0.145	161.7	27.5	28.1	0.108

Table A-5. Laminar flame speed data for DIMP/CH₄/air.

% DIMP	ϕ	Temp. [°C]	Unburned Density [kg/m ³]	Burned Density [kg/m ³]	S_b^0 [cm/s]	S_L^0 [cm/s]	$S_{L,RC}^0$ [cm/s]	L_b [cm]
0.1	0.9	120.5	0.859	0.154	200.1	35.8	36.4	0.038
0.1	1.0	120.4	0.856	0.147	224.9	38.5	39.2	0.053
0.1	1.0	120.5	0.855	0.147	226.4	38.8	39.5	0.075
0.1	1.1	120.4	0.852	0.145	221.3	37.6	38.2	0.066
0.1	1.2	120.5	0.849	0.146	182.9	31.5	32.2	0.105

*A.4 H₂ Flame Speed Data Tables***Table A-6.** Laminar flame speed data for Neat H₂/air.

ϕ	Temp. [°C]	Unburned Density [kg/m ³]	Burned Density [kg/m ³]	S_b^0 [cm/s]	S_L^0 [cm/s]	$S_{L,RC}^0$ [cm/s]	L_b [cm]
0.6	119.9	0.727	0.166	706.4	160.9	161.4	0.005
0.8	119.5	0.686	0.137	1263.3	252.8	253.3	0.039
1.0	118.2	0.651	0.121	1692.2	315.5	315.9	0.041
1.0	119.7	0.649	0.121	1719.8	321.7	322.2	0.049
1.3	119.4	0.601	0.114	2095.8	397.1	397.6	0.058
1.6	120.3	0.560	0.110	2143.1	423.2	423.6	0.060
1.6	121.0	0.559	0.110	2151.0	425.4	425.8	0.059
1.9	120.1	0.525	0.108	2054.5	421.8	422.2	0.063
2.2	119.7	0.495	0.106	1891.5	403.1	403.6	0.067
2.2	120.0	0.495	0.106	1906.8	406.6	407.1	0.063
2.6	119.7	0.460	0.103	1659.8	371.4	371.8	0.068
3.0	119.2	0.431	0.101	1454.3	340.3	340.8	0.072
3.5	119.6	0.400	0.099	1208.6	298.6	299.1	0.080
4.0	119.4	0.373	0.097	1012.0	262.6	263.1	0.080
5.0	117.7	0.333	0.094	699.4	197.6	198.2	0.120

Table A-7. Laminar flame speed data for 0.1% TEP/H₂/air.

ϕ	Temp. [°C]	Unburned Density [kg/m ³]	Burned Density [kg/m ³]	S_b^0 [cm/s]	S_L^0 [cm/s]	$S_{L,RC}^0$ [cm/s]	L_b [cm]
0.8	119.7	0.686	0.137	1129.3	226.1	226.6	0.000
0.8	119.7	0.686	0.137	1138.3	227.9	228.4	0.009
1.0	120.7	0.647	0.121	1565.6	293.6	294.0	0.030
1.3	120.4	0.859	0.154	1906.3	342.5	343.0	0.037
1.6	120.7	0.848	0.162	1916.1	367.2	367.6	0.047
1.9	120.4	0.838	0.172	1765.4	362.9	363.3	0.051
1.9	119.6	0.526	0.108	1765.9	362.1	362.6	0.062
2.2	120.3	0.829	0.184	1539.1	341.9	342.4	0.064
2.6	119.8	0.460	0.103	1312.6	293.8	294.2	0.067
3.0	120.5	0.430	0.101	1034.0	242.6	243.1	0.094
3.0	119.8	0.431	0.101	1055.3	247.3	247.8	0.078

Table A-8. Laminar flame speed data for 0.1% DEMP/H₂/air.

ϕ	Temp. [°C]	Unburned Density [kg/m ³]	Burned Density [kg/m ³]	S_b^0 [cm/s]	S_L^0 [cm/s]	$S_{L,RC}^0$ [cm/s]	L_b [cm]
0.8	119.2	0.686	0.137	1144.8	228.9	229.4	0.008
1.0	119.3	0.649	0.121	1610.5	301.0	301.5	0.025
1.3	121.2	0.599	0.114	1931.7	367.5	368.0	0.042
1.6	121.9	0.557	0.110	1978.1	392.0	392.4	0.056
1.6	120.6	0.559	0.110	1962.3	387.7	388.2	0.048
1.9	120.6	0.827	0.166	1878.2	377.1	377.6	0.060
1.9	120.6	0.827	0.166	1863.9	374.3	374.7	0.064
2.2	121.3	0.493	0.105	1656.0	354.1	354.6	0.062
2.6	119.7	0.460	0.103	1360.2	304.3	304.8	0.066
3.0	119.8	0.431	0.101	1120.8	262.6	263.1	0.088
3.0	120.5	0.430	0.101	1115.8	261.8	262.3	0.095

Table A-9. Laminar flame speed data for DMMP/H₂/air.

% DMMP	ϕ	Temp. [°C]	Unburned Density [kg/m ³]	Burned Density [kg/m ³]	S_b^0 [cm/s]	S_L^0 [cm/s]	$S_{L,RC}^0$ [cm/s]	L_b [cm]
0.1	0.8	118.9	0.687	0.137	1174.4	234.7	235.2	0.005
0.1	1.0	119.8	0.649	0.121	1645.3	307.8	308.3	0.031
0.1	1.3	120.2	0.600	0.114	1966.5	373.3	373.8	0.051
0.1	1.6	120.3	0.560	0.110	2022.8	399.4	399.9	0.057
0.1	1.6	120.4	0.559	0.110	2035.1	401.9	402.4	0.052
0.1	1.6	120.5	0.559	0.110	2050.4	405.0	405.5	0.055
0.1	1.9	120.3	0.525	0.108	1918.5	394.0	394.5	0.062
0.1	2.2	120.3	0.494	0.106	1751.3	373.7	374.2	0.066
0.1	2.6	119.8	0.460	0.103	1482.4	331.7	332.2	0.059
0.1	3.0	120.4	0.430	0.101	1214.1	284.8	285.3	0.093
0.1	3.0	119.8	0.431	0.101	1248.9	292.6	293.1	0.059
0.1	3.0	119.7	0.431	0.101	1239.0	290.2	290.7	0.070
0.1	3.5	119.5	0.400	0.099	995.4	245.9	246.4	0.116
0.3	1.0	120.1	0.648	0.121	1409.2	263.9	264.3	0.016
0.3	1.3	120.0	0.601	0.114	1690.9	320.8	321.3	0.026
0.3	1.3	120.1	0.600	0.114	1657.3	314.5	315.0	0.027
0.3	1.6	119.8	0.560	0.111	1654.6	326.3	326.8	0.040
0.3	1.9	119.5	0.526	0.108	1477.2	302.9	303.3	0.049
0.3	2.2	120.0	0.495	0.106	1258.1	268.3	268.8	0.065
0.3	2.2	120.1	0.495	0.106	1270.2	270.9	271.4	0.061
0.3	2.6	120.2	0.460	0.103	1006.0	225.3	225.8	0.086

Table A-10. Laminar flame speed data for DIMP/H₂/air.

% DMMP	ϕ	Temp. [°C]	Unburned Density [kg/m ³]	Burned Density [kg/m ³]	S_b^0 [cm/s]	S_L^0 [cm/s]	$S_{L,RC}^0$ [cm/s]	L_b [cm]
0.1	0.8	120.2	0.685	0.137	1357.5	272.0	272.5	0.027
0.1	1.0	119.9	0.648	0.121	1721.7	322.2	322.7	0.037
0.1	1.3	120.3	0.600	0.114	1895.3	359.9	360.4	0.031
0.1	1.3	120.4	0.600	0.114	1883.1	357.6	358.1	0.032
0.1	1.6	120.4	0.559	0.110	1892.0	373.7	374.1	0.044
0.1	1.9	120.6	0.524	0.108	1748.4	359.3	359.8	0.055
0.1	2.2	120.8	0.494	0.105	1526.0	326.0	326.5	0.057
0.1	2.6	119.3	0.461	0.103	1222.5	273.3	273.8	0.081
0.1	3.0	120.5	0.430	0.101	825.1	193.6	194.1	0.135
0.2	1.6	120.3	0.560	0.110	1814.2	358.2	358.7	0.047
0.2	1.6	119.4	0.561	0.111	1648.0	324.8	325.2	0.062
0.3	1.6	120.2	0.560	0.110	1436.5	283.6	284.1	0.039
0.4	1.6	119.9	0.560	0.110	1161.9	229.2	229.7	0.044

A.5 H₂ Ignition Delay Time Data Tables

Table A-11. Hydrogen ignition delay times at $\phi = 0.5$ and 98% Ar dilution (1.00% H₂/ 1.00% O₂/ 98.00% Ar).

P_5 [atm]	T_5 [K]	Ign. Delay [μs]
1.01	2016	70
1.00	1847	94
1.01	1628	137
1.04	1455	235
1.10	1388	295
1.01	1270	522
1.02	1196	703
0.97	1117	1133
0.99	1081	1400

Table A-12. Hydrogen ignition delay times at $\phi = 1.0$ and 98% Ar dilution (1.35% H₂/ 0.67% O₂/ 97.98% Ar).

P_5 [atm]	T_5 [K]	Ign. Delay [μ s]
0.98	1961	99
0.99	1824	123
0.98	1730	160
0.96	1587	229
1.07	1484	280
1.06	1479	287
1.04	1395	370
1.04	1333	549
1.05	1306	550
1.02	1191	978
1.02	1149	1155

Table A-13. Hydrogen/DMP ignition delay times at $\phi = 0.5$ and 98% Ar dilution (0.08% DMP/0.69% H₂/ 1.23% O₂/ 97.99% Ar).

P_5 [atm]	T_5 [K]	Ign. Delay [μ s]
1.01	1665	65
1.04	1574	81
1.10	1482	118
1.03	1447	148
0.99	1369	248
0.99	1302	329
1.00	1252	411
0.96	1204	505
0.96	1170	737
0.97	1148	831

Table A-14. Hydrogen/DEP ignition delay times at $\phi = 0.5$ and 98% Ar dilution (0.07% DEP/0.56% H₂/ 1.37% O₂/ 98.00% Ar).

P_5 [atm]	T_5 [K]	Ign. Delay [μ s]
1.02	1867	32
1.01	1722	51
0.98	1580	86
0.98	1483	135
0.97	1378	239
1.05	1359	259
0.98	1366	268
1.00	1331	292
0.96	1246	457

Table A-15. Hydrogen/TMP ignition delay times at $\phi = 0.5$ and 98% Ar dilution (0.08% TMP/0.63% H₂/ 1.31% O₂/ 97.98% Ar).

P_5 [atm]	T_5 [K]	Ign. Delay [μ s]
0.99	1734	64
0.97	1615	104
1.04	1529	139
0.97	1394	217
1.07	1324	293
1.01	1224	411
1.02	1177	555
0.94	1098	922

A.6 *Neat OPC Ignition Delay Time Data Tables*

Table A-16. DEP ignition delay times with hydrogen from Table A-14 replaced with Ar. (0.007% DEP/ 1.38% O₂/ 98.56% Ar).

P_5 [atm]	T_5 [K]	Ign. Delay [μs]
1.02	1965	59
0.95	1931	60
1.00	1787	104
0.99	1687	159
1.02	1551	247
1.02	1556	259
1.01	1518	331
1.01	1430	560

Table A-17. TMP ignition delay times with hydrogen from Table A-15 replaced with Ar. (0.008% TMP/ 1.31% O₂/ 98.61% Ar).

P_5 [atm]	T_5 [K]	Ign. Delay [μs]
0.99	1541	119
0.99	1502	267

A.7 C_2H_4 Ignition Delay Time Data Tables

Table A-18. Ethylene ignition delay times at $\phi = 0.5$ and 98% Ar dilution (0.29% C_2H_4 / 1.71% O_2 / 98.00% Ar).

P_5 [atm]	T_5 [K]	Ign. Delay [μs]
0.98	1806	88
0.99	1773	93
0.98	1677	127
0.98	1597	170
1.00	1536	209
0.99	1483	281
1.01	1455	289
0.98	1429	349
0.96	1359	627
0.97	1298	979

Table A-19. Ethylene ignition delay times at $\phi = 1.0$ and 98% Ar dilution (0.5% C_2H_4 / 1.50% O_2 / 98.00% Ar).

P_5 [atm]	T_5 [K]	Ign. Delay [μs]
1.02	1840	57
1.00	1783	86
0.97	1665	130
1.43	1644	138
0.97	1622	162
1.02	1484	344
0.96	1491	368
1.04	1447	407
0.98	1377	711
0.75	1333	998
0.96	1317	1276

Table A-20. Ethylene/DMP ignition delay times at $\phi = 0.5$ and 98% Ar dilution (0.03% DMP/0.25% C₂H₄/ 1.72% O₂/ 97.99% Ar).

P_5 [atm]	T_5 [K]	Ign. Delay [μ s]
0.99	1739	87
0.98	1722	90
1.02	1644	111
0.95	1588	138
1.04	1536	186
1.01	1441	297
1.00	1398	378
0.97	1343	577
0.98	1349	609
0.99	1314	686
0.94	1248	1319
0.92	1257	1362

Table A-21. Ethylene/DMP ignition delay times at $\phi = 1.0$ and 98% Ar dilution (0.05% DMP/0.44% C₂H₄/ 1.51% O₂/ 97.99% Ar).

P_5 [atm]	T_5 [K]	Ign. Delay [μ s]
0.97	1748	66
0.97	1656	110
0.99	1588	143
1.04	1525	219
1.03	1524	223
1.02	1456	365
0.99	1394	633
0.94	1390	645
1.03	1378	707
0.96	1377	720
1.02	1342	1022

Table A-22. Ethylene/DEP ignition delay times at $\phi = 0.5$ and 98% Ar dilution (0.03% DEP/0.23% C₂H₄/ 1.73% O₂/ 98.01% Ar).

P_5 [atm]	T_5 [K]	Ign. Delay [μ s]
1.00	1715	79
0.99	1636	99
0.99	1635	106
0.98	1599	122
1.03	1567	130
0.96	1478	235
1.04	1424	283
1.00	1407	342
1.00	1358	451
0.99	1309	640
0.99	1318	698
0.98	1273	934

Table A-23. Ethylene/DEP ignition delay times at $\phi = 1.0$ and 98% Ar dilution (0.05% DEP/0.41% C₂H₄/ 1.54% O₂/ 98.00% Ar).

P_5 [atm]	T_5 [K]	Ign. Delay [μ s]
0.96	1739	73
1.04	1717	76
1.00	1647	103
0.96	1546	169
0.99	1484	257
1.04	1427	360
0.99	1431	406
0.98	1422	436
0.98	1385	539
0.99	1395	558
0.99	1349	823
0.98	1307	1225

Table A-24. Ethylene/TMP ignition delay times at $\phi = 0.5$ and 98% Ar dilution (0.03% TMP/0.24% C₂H₄/ 1.72% O₂/ 98.00% Ar).

P_5 [atm]	T_5 [K]	Ign. Delay [μ s]
1.01	1801	60
1.00	1721	79
1.01	1618	111
1.01	1634	113
1.01	1517	168
1.00	1461	229
1.00	1465	237
0.98	1392	393
1.04	1363	448
1.00	1336	578
0.99	1328	653
0.97	1272	961

Table A-25. Ethylene/TMP ignition delay times at $\phi = 1.0$ and 98% Ar dilution (0.05% TMP/0.43% C₂H₄/ 1.52% O₂/ 98.00% Ar).

P_5 [atm]	T_5 [K]	Ign. Delay [μ s]
1.03	1794	60
1.01	1706	80
1.02	1608	125
1.02	1559	164
1.01	1507	241
1.00	1499	254
1.05	1447	338
1.01	1452	358
0.99	1386	639
1.01	1357	740
0.98	1336	923
1.01	1333	1032

A.8 Additional C_2H_4 Ignition Delay Time Modeling Plots

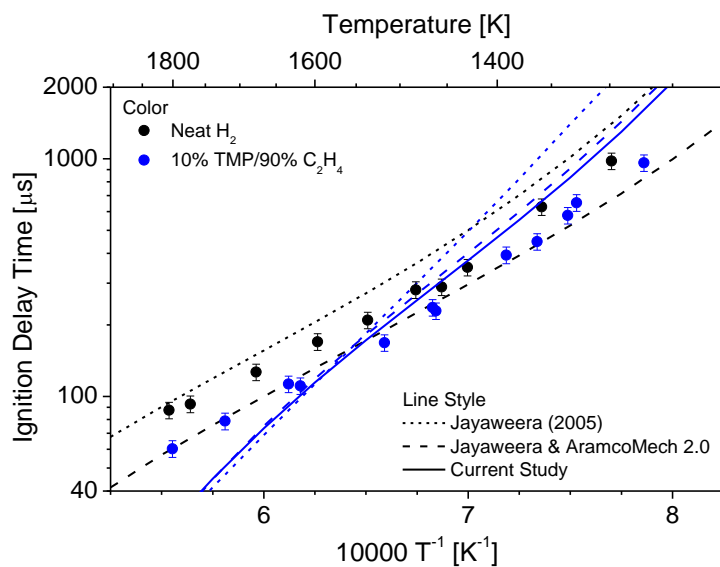


Figure A-6. Ethylene-based ignition delay times ($\phi = 0.5$, 1 atm, diluted with 98% argon). ICARE T_5 uncertainty is estimated to be 1%.

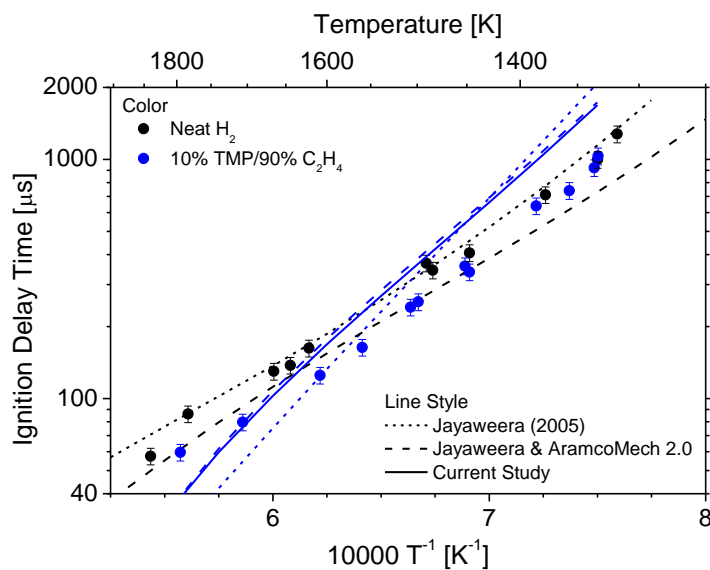


Figure A-7. Ethylene-based ignition delay times ($\phi = 1.0$, 1 atm, diluted with 98% argon). ICARE T_5 uncertainty is estimated to be 1%.

A.9 DMP and TMP OPC Submechanism

Table A-26. DMP/TMP mechanism thermodynamic properties.

P	8/18/99	ivtanP	1	0	0	OG	300.000	5000.000	1000.000	01
	2.50176312e+00	0.00000000e+00	0.00000000e+00	0.00000000e+00	0.00000000e+00	0.00000000e+00	0.00000000e+00	0.00000000e+00	0.00000000e+00	2
	3.73265706e+04	5.36347667e+00	2.50176312e+00	0.00000000e+00	0.00000000e+00	0.00000000e+00	0.00000000e+00	0.00000000e+00	0.00000000e+00	3
	0.00000000e+00	0.00000000e+00	3.73265706e+04	5.36347667e+00						4
PO	sikes0204180	1P	1			G	250.000	5000.000	1707.200	1
	3.56732193e+00	1.07565433e-03	4.86866457e-07	9.79036055e-11	7.27563342e-15					2
	-4.96869077e+03	4.75731096e+00	3.02850433e+00	2.23715294e-03	1.11918389e-06					3
	7.92919879e-11	5.03063643e-14	4.81714523e+03	7.61492973e+00						4
PO2	sikes0204180	2P	1			G	250.000	5000.000	1795.600	1
	6.03365184e+00	8.68585448e-04	3.17832283e-07	5.33289133e-11	3.39268329e-15					2
	-3.73506750e+04	5.44745968e+00	3.09954884e+00	8.24270127e-03	7.33529953e-06					3
	3.03679847e-09	4.79962173e-13	3.64065181e+04	1.00914925e+01						4
PO3	sikes0204180	3P	1			G	250.000	5000.000	1644.900	1
	8.85148310e+00	1.00413007e-03	3.55213716e-07	5.73789107e-11	3.49881290e-15					2
	-5.77724956e+04	1.91681571e+01	3.71036799e+00	1.50081626e-02	1.50705778e-05					3
	7.04250600e-09	1.25608769e-12	5.62025052e+04	7.70449840e+00						4
HPO	sikes020418H	1O	1P	1		G	250.000	5000.000	1435.800	1
	4.50632458e+00	2.54763292e-03	1.06348234e-06	2.02613053e-10	1.45137318e-14					2
	-1.30223492e+04	1.36540279e+00	2.85464646e+00	5.37316614e-03	1.86843414e-06					3
	-5.53854432e-10	3.36611852e-13	1.23949339e+04	1.05181176e+01						4
HPO2	sikes020418H	1O	2P	1		G	250.000	5000.000	1664.300	1
	7.16004016e+00	2.48593438e-03	9.07918118e-07	1.54468698e-10	1.00571056e-14					2
	-5.27609093e+04	1.26685637e+01	2.15846541e+00	1.46875611e-02	1.27641739e-05					3
	5.52667673e-09	9.52504724e-13	5.10128146e+04	1.40943426e+01						4
HOPO	sikes020418H	1O	2P	1		G	250.000	5000.000	1555.500	1
	9.02565030e+00	5.65169519e-04	2.61861206e-07	5.31123062e-11	3.94809590e-15					2
	-5.96833795e+04	2.16385755e+01	1.55780627e+00	2.09184478e-02	2.15308929e-05					3
	1.01007060e-08	1.80525526e-12	5.74327453e+04	1.73491921e+01						4
HOPO2	sikes020418H	1O	3P	1		G	250.000	5000.000	1461.500	1
	9.95515378e+00	2.32599141e-03	8.69618980e-07	1.49281051e-10	9.72761952e-15					2
	-8.90629835e+04	2.54171857e+01	1.87813814e+00	2.56998998e-02	2.76854656e-05					3
	1.43665356e-08	2.90072984e-12	8.66797654e+04	1.64225766e+01						4
PO[H][OH]	sikes020418H	2O	2P	1		G	250.000	5000.000	1329.000	1
	8.39000827e+00	3.51142679e-03	1.28980832e-06	2.23842433e-10	1.49531821e-14					2
	-4.78942599e+04	1.69712302e+01	1.46769447e+00	2.76802030e-02	3.36799010e-05					3
	1.97123543e-08	4.41761845e-12	4.62440771e+04	1.74844341e+01						4
PO[OH]2	sikes020418H	2O	3P	1		G	250.000	5000.000	1442.800	1
	9.45604551e+00	4.46193372e-03	1.56752438e-06	2.63378624e-10	1.71869497e-14					2
	-8.37721979e+04	1.80900846e+01	5.58707400e+00	1.77522886e-02	1.85565631e-05					3
	9.81701663e-09	2.00885241e-12	8.28748004e+04	1.15519884e+00						4
PO[OH]3	sikes020418H	3O	4P	1		G	250.000	5000.000	1003.600	1
	1.30310628e+01	5.79654384e-03	1.96939597e-06	3.21714169e-10	2.05341179e-14					2
	-1.42972182e+05	3.72748209e+01	5.66630410e+00	3.77626997e-02	5.45449291e-05					3
	3.90249889e-08	1.07501484e-11	1.41595015e+05	2.29798583e+00						4
PO[OH]2O	sikes020418H	2O	4P	1		G	250.000	5000.000	1113.500	1
	1.20299118e+01	4.92338989e-03	1.76877889e-06	3.03123595e-10	2.01194388e-14					2
	-1.10500980e+05	3.20649998e+01	5.86592178e+00	2.86709497e-02	3.71653111e-05					3
	2.42790762e-08	6.19366967e-12	1.09170929e+05	1.98273965e+00						4
P2O3	11/24/03BACG2	O	3P	2H	0	OG	300.000	3000.000	1000.000	1
	0.85027510E+01	0.68059505E-02	0.44982937E-05	0.12943537E-08	0.13843932E-12					2
	-0.82155913E+05	0.98718714E+01	0.46753674E+01	0.20306654E-01	0.23472860E-04					3
	0.14050913E-07	0.35937510E-11	0.81252103E+05	0.91649802E+01						4
P2O4	11/24/03BACG2	O	4P	2H	0	OG	300.000	3000.000	1000.000	1
	0.98937530E+01	0.90879256E-02	0.57987209E-05	0.16371645E-08	0.17306518E-12					2
	-0.11277818E+06	0.16534077E+02	0.48550607E+01	0.26990353E-01	0.31001919E-04					3
	0.18491050E-07	0.46874867E-11	0.11160022E+06	0.84817916E+01						4
P2O5	11/24/03BACG2	O	5P	2H	0	OG	300.000	3000.000	1000.000	1
	0.13654491E+02	0.72700557E-02	0.47059756E-05	0.13655235E-08	0.14829849E-12					2
	-0.14140792E+06	0.37267141E+02	0.34434411E+01	0.44575959E-01	0.57860881E-04					3
	0.36601824E-07	0.93245468E-11	0.13910535E+06	0.13088470E+02						4
CH3PO	sikes020418C	1H	3O	1P	1G		250.000	5000.000	1649.600	1
	7.67287823e+00	6.57369648e-03	2.33699472e-06	3.90263882e-10	2.50645014e-14					2
	-2.31378157e+04	1.37186112e+01	2.14043471e+00	1.97125758e-02	1.50660690e-05					3
	6.26759824e-09	1.09012172e-12	2.11193086e+04	1.60904213e+01						4

CH3PO2	sikes020418C	1H	3O	2P	1G	250.000	5000.000	1687.900	1
9.88200886e+00	7.17222753e-03	-2.52160756e-06	4.16360550e-10	-2.64607447e-14					2
-6.31076313e+04	-2.56021907e+01	1.67919867e+00	2.71184010e-02	-2.20012836e-05					3
9.32128219e-09	-1.60187260e-12	-6.02046828e+04	1.83592976e+01						4
CH3OPO	sikes090418C	1H	3O	2P	1G	250.000	5000.000	1608.900	1
9.68513449e+00	8.59318066e-03	-3.58463516e-06	6.78057020e-10	-4.80765986e-14					2
-5.77057805e+04	-2.35366183e+01	2.33257979e+00	2.26498863e-02	-1.16675940e-05					3
1.49592972e-09	2.87664835e-13	-5.49434735e+04	1.68971606e+01						4
CH3OPO2	sikes020418C	1H	3O	3P	1G	250.000	5000.000	1797.000	1
1.21555722e+01	8.04711466e-03	-3.02166353e-06	5.25127739e-10	-3.47693673e-14					2
-8.77169757e+04	-3.62379869e+01	2.47171631e+00	2.90773111e-02	-2.04685369e-05					3
7.07987294e-09	-9.75220564e-13	-8.40881297e+04	1.64821946e+01						4
PO[OH]2ME	sikes020418C	1H	5O	3P	1G	250.000	5000.000	1276.400	1
1.40336800e+01	1.04138245e-02	-3.73877430e-06	6.35272313e-10	-4.16341041e-14					2
-1.15818409e+05	-4.38244023e+01	1.94071805e+00	5.59751441e-02	-7.01751335e-05					3
4.41000059e-08	-1.06690863e-11	-1.13086034e+05	1.55503133e+01						4
PO[OH]2[OME]	sikes020418C	1H	5O	4P	1G	250.000	5000.000	1458.500	1
1.55643947e+01	1.11038489e-02	-3.92424976e-06	6.55251617e-10	-4.22160125e-14					2
-1.41471195e+05	-4.90107987e+01	6.35195357e+00	3.96183101e-02	-3.91851433e-05					3
2.06711479e-08	-4.34525956e-12	-1.38864411e+05	-1.81287884e+00						4
PO[OH]ME	sikes020418C	1H	4O	2P	1G	250.000	5000.000	1487.000	1
1.14294145e+01	7.92003635e-03	-2.80503579e-06	4.69640535e-10	-3.03502835e-14					2
-5.78880712e+04	-3.19351191e+01	2.00464396e+00	3.73341010e-02	-3.87685883e-05					3
2.03975929e-08	-4.18576992e-12	-5.52941728e+04	1.61687317e+01						4
PO[OH][OME]	sikes020418C	1H	4O	3P	1G	250.000	5000.000	1679.200	1
1.12573254e+01	1.06165851e-02	-3.90617993e-06	6.74317841e-10	-4.46550919e-14					2
-8.18612709e+04	-2.62858842e+01	4.88560657e+00	2.58129942e-02	-1.76733087e-05					3
6.29106267e-09	-9.14700989e-13	-7.97040326e+04	7.78890931e+00						4
PO[H]ME[OME]	sikes020418C	2H	7O	2P	1G	250.000	5000.000	1764.900	1
1.52652672e+01	1.42437673e-02	-4.95031762e-06	8.04110322e-10	-5.01399072e-14					2
-7.58770725e+04	-5.32398146e+01	2.85468980e+00	4.04039465e-02	-2.64293934e-05					3
8.97867774e-09	-1.26605055e-12	-7.10194439e+04	1.47906571e+01						4
PO[H][OME]2	sikes020418C	2H	7O	3P	1G	250.000	5000.000	1551.900	1
1.68205808e+01	1.53635112e-02	-5.44636317e-06	9.00345831e-10	-5.70125346e-14					2
-1.02287454e+05	-5.88365474e+01	2.93121333e+00	4.96981819e-02	-4.02853644e-05					3
1.78931787e-08	-3.33298420e-12	-9.74163639e+04	1.54611557e+01						4
P[OH]ME[OME]	sikes020418C	2H	7O	2P	1G	250.000	5000.000	1611.200	1
1.71025726e+01	1.19071380e-02	-4.03972200e-06	6.44575213e-10	-3.96654811e-14					2
-7.04448777e+04	-6.21218596e+01	1.34552102e+00	5.52719257e-02	-5.13393814e-05					3
2.43133695e-08	-4.53898328e-12	-6.55035848e+04	2.03454758e+01						4
POME[OME]	sikes210418C	2H	6O	2P	1G	250.000	5000.000	1664.300	1
1.48474635e+01	1.20221061e-02	-4.18410447e-06	6.85590789e-10	-4.33183428e-14					2
-5.69125704e+04	-4.97862780e+01	1.83419390e+00	4.41961380e-02	-3.63571321e-05					3
1.57926966e-08	-2.78838779e-12	-5.23406070e+04	1.97967519e+01						4
PO[OME]2	sikes020418C	2H	6O	3P	1G	250.000	5000.000	1798.900	1
1.36126208e+01	1.60219323e-02	-5.87835017e-06	1.00831570e-09	-6.62546144e-14					2
-8.02267544e+04	-3.78645196e+01	3.48827274e+00	3.70007163e-02	-2.19183272e-05					3
6.34971865e-09	-7.15985153e-13	-7.63758098e+04	1.75664664e+01						4
PO[OH]ME[OME]	sike020418C	2H	7O	3P	1G	250.000	5000.000	1483.300	1
1.77543213e+01	1.44118612e-02	-5.13481248e-06	8.62900515e-10	-5.58899046e-14					2
-1.14770160e+05	-6.40204729e+01	9.71100516e-01	6.60880218e-02	-6.81820069e-05					3
3.59804431e-08	-7.44326219e-12	-1.10028909e+05	2.19752732e+01						4
PO[OH]ME[OCH2]	sik020418C	2H	6O	3P	1G	250.000	5000.000	1328.500	1
1.71258261e+01	1.26225382e-02	-4.56651286e-06	7.78134709e-10	-5.10099133e-14					2
-8.96606161e+04	-5.85871095e+01	2.59661514e+00	6.37327818e-02	-7.56371130e-05					3
4.56817909e-08	-1.07164758e-11	-8.60551219e+04	1.39317026e+01						4
PO[OH][OME][CH2]	s020418C	2H	6O	3P	1G	250.000	5000.000	1397.200	1
1.68283391e+01	1.26659174e-02	-4.50119114e-06	7.53147586e-10	-4.84922658e-14					2
-8.71568549e+04	-5.66510115e+01	2.19369598e+00	6.17603863e-02	-6.98654164e-05					3
4.03336523e-08	-9.05344958e-12	-8.33221130e+04	1.71352873e+01						4
POME[OME]O	sikes210418C	2H	6O	3P	1G	250.000	5000.000	1784.800	1
1.89950256e+01	1.07213617e-02	-3.63019331e-06	5.81573664e-10	-3.60896325e-14					2
-8.40170615e+04	-7.25754993e+01	8.77405824e-01	5.55725770e-02	-4.72226256e-05					3
1.99378161e-08	-3.29994274e-12	-7.77848934e+04	2.40501256e+01						4
PO[OH][OME]2	sikes020418C	2H	7O	4P	1G	250.000	5000.000	1732.900	1
1.95391386e+01	1.46706021e-02	-5.07468709e-06	8.25684718e-10	-5.17588923e-14					2
-1.40702768e+05	-7.07010843e+01	6.45919763e+00	4.54274768e-02	-3.39224263e-05					3
1.34520916e-08	-2.19102525e-12	-1.35967226e+05	-2.22940920e-01						4
PO[OME]2O	sikes020418C	2H	6O	4P	1G	250.000	5000.000	1274.100	1
1.46444798e+01	1.85568715e-02	-7.06322265e-06	1.24342761e-09	-8.30859504e-14					2
-1.06755061e+05	-4.27404573e+01	1.02054217e+01	1.93623255e-02	7.12519402e-06					3

-1.39448714e-08	4.39148640e-12	-1.04534425e+05	-1.60202535e+01		4
PO[OH]OME[OCH2]	si020418C	2H	60 4P 1G	250.000 5000.000 1589.500	1
1.85155981e+01	1.32215155e-02	-4.64744126e-06	7.69284206e-10	-4.90552263e-14	2
-1.15234307e+05	-6.17710673e+01	8.02331252e+00	4.06093513e-02	-3.37206660e-05	3
1.52809829e-08	-2.84720116e-12	-1.11717703e+05	-6.19490899e+00		4
POME[OME]2	sikes020418C	3H	90 3P 1G	250.000 5000.000 1783.800	1
2.17892811e+01	1.73569188e-02	-5.85008536e-06	9.24773355e-10	-5.63336887e-14	2
-1.13840603e+05	-8.34161174e+01	5.17027772e+00	5.27866632e-02	-3.60065494e-05	3
1.30328051e-08	-1.96941655e-12	-1.07257689e+05	7.71115815e+00		4
POME[OME][OCH2]	si020418C	3H	80 3P 1G	250.000 5000.000 1461.100	1
2.07816002e+01	1.65277543e-02	-5.84067450e-06	9.65089092e-10	-6.11754736e-14	2
-8.85567309e+04	-7.69301264e+01	2.80586537e+00	7.05020662e-02	-7.13417502e-05	3
3.78272031e-08	-7.96785193e-12	-8.32718240e+04	1.57940558e+01		4
PO[CH2][OME]2	sike020418C	3H	80 3P 1G	250.000 5000.000 1653.000	1
2.16906982e+01	1.50764143e-02	-5.10029545e-06	8.10087469e-10	-4.95261849e-14	2
-8.70443628e+04	-8.35079189e+01	3.25036850e+00	6.24245755e-02	-5.46610931e-05	3
2.51210079e-08	-4.63125365e-12	-8.07033944e+04	1.45353501e+01		4
PO[OME]3	sikes050418C	3H	90 4P 1G	250.000 5000.000 1625.300	1
2.04387235e+01	2.24283711e-02	-8.30840129e-06	1.44010885e-09	-9.56264826e-14	2
-1.38166017e+05	-7.43760866e+01	6.10859015e+00	5.42608014e-02	-3.54475297e-05	3
1.20314667e-08	-1.70036393e-12	-1.32918006e+05	3.32226620e+00		4
PO[OME]2[OCH2]	sik020418C	3H	80 4P 1G	250.000 5000.000 1749.800	1
2.29307091e+01	1.73714805e-02	-6.32367360e-06	1.07733046e-09	-7.04029345e-14	2
-1.14691851e+05	-8.76233995e+01	6.11046348e+00	5.53251985e-02	-3.98527505e-05	3
1.47733779e-08	-2.23579309e-12	-1.08475642e+05	3.51397654e+00		4
C2H5OPO2	sikes020418C	2H	50 3P 1G	250.000 5000.000 1740.500	1
1.66522313e+01	1.11146085e-02	-4.02048340e-06	6.79032677e-10	-4.39702746e-14	2
-9.47558874e+04	-5.97896845e+01	1.13572520e+00	4.72965813e-02	-3.72920930e-05	3
1.48517071e-08	-2.37546557e-12	-8.91462433e+04	2.38537957e+01		4
PO[OH]2[OET]	sikes020418C	2H	70 4P 1G	250.000 5000.000 1412.300	1
1.88032661e+01	1.57690606e-02	-5.67230857e-06	9.61926274e-10	-6.28207645e-14	2
-1.47506870e+05	-6.52209644e+01	4.98406345e+00	5.88551623e-02	-6.00768505e-05	3
3.28273639e-08	-7.17218079e-12	-1.43578038e+05	5.56530932e+00		4
PO[OH]ME[OET]	sike020418C	3H	90 4P 1G	250.000 5000.000 1641.400	1
2.34674107e+01	1.91738703e-02	-6.89128656e-06	1.16193056e-09	-7.52652463e-14	2
-1.47171373e+05	-9.19703442e+01	2.99829002e+00	7.06047418e-02	-5.81587346e-05	3
2.48751929e-08	-4.30406512e-12	-1.40239869e+05	1.69310398e+01		4
PO[OH][OET]2	8/99 GlauDP	1O	4H 11C 4G	300.000 5000.000 1396.000	01
2.32375305e+01	2.68920611e-02	-1.04378111e-05	1.89994080e-09	-1.24780524e-13	2
-1.47242547e+05	-8.51610667e+01	7.97791917e-01	8.44939153e-02	-6.81477587e-05	3
2.85364266e-08	-4.85697498e-12	-1.39982865e+05	3.34919550e+01		4
POME[OET]2	8/18/99 GlauDP	1O	3H 13C 5G	300.000 5000.000 1400.000	01
2.26491894e+01	3.51180942e-02	-1.52781721e-05	2.96731560e-09	-2.01306367e-13	2
-1.17881723e+05	-8.49533314e+01	-3.26829467e+00	1.05787770e-01	-8.98484029e-05	3
3.87727624e-08	-6.73836501e-12	-1.10002600e+05	5.04682416e+01		4
PO[OET]3	8/18/99 GlauDP	1O	4H 15C 6G	300.000 5000.000 1408.000	01
2.58190857e+01	3.69798412e-02	-1.15622977e-05	1.68450905e-09	-9.33386933e-14	2
-1.47984273e+05	-9.38603557e+01	-1.45794555e+00	1.22031767e-01	-1.13504156e-04	3
5.62732684e-08	-1.09719328e-11	-1.40629962e+05	4.50883025e+01		4
PO[OH]2[CH2]	sikes020418C	1H	40 3P 1G	250.000 5000.000 931.400	1
1.35536013e+01	8.20062008e-03	-2.91143663e-06	4.88670326e-10	-3.16224033e-14	2
-8.88399881e+04	-3.90309480e+01	2.13218921e+00	6.33247714e-02	-1.05596721e-04	3
8.68992264e-08	-2.74846217e-11	-8.68647695e+04	1.41430373e+01		4
PO[OH]2[OCH2]	sike020418C	1H	40 4P 1G	250.000 5000.000 1187.700	1
1.50832142e+01	9.17925896e-03	-3.33210241e-06	5.73847400e-10	-3.81607082e-14	2
-1.16204585e+05	-4.35363185e+01	7.82174027e+00	3.71779745e-02	-4.55269243e-05	3
2.94224552e-08	-7.47889765e-12	-1.14596827e+05	-8.03011637e+00		4
CH2OPO2	sikes030418C	1H	20 3P 1G	250.000 5000.000 1492.200	1
1.29165898e+01	4.66899220e-03	-1.77376211e-06	3.12057764e-10	-2.09215207e-14	2
-6.21947237e+04	-3.77505680e+01	4.13790068e+00	2.91006850e-02	-2.91354550e-05	3
1.46344146e-08	-2.91416869e-12	-5.94630426e+04	8.13313071e+00		4
PO[H][OH][OME]	sik020418C	1H	50 3P 1G	250.000 5000.000 1492.200	1
1.35915772e+01	1.07806528e-02	-3.80099917e-06	6.26990182e-10	-3.96886970e-14	2
-1.03645698e+05	-4.16192821e+01	3.36013326e+00	3.88916274e-02	-3.53638255e-05	3
1.73722999e-08	-3.48412332e-12	-1.00377238e+05	1.20679097e+01		4
P[OH]3	11/9/01 Pitz P	1O	3H 3 OG	300.000 5000.000 1400.000	31
1.64881553e+01	2.05354184e-03	-8.26481813e-07	1.42275902e-10	-8.85545784e-15	2
-1.00161107e+05	-5.36914436e+01	3.14297667e+00	4.10039208e-02	-4.45410762e-05	3
2.22434587e-08	-4.21297379e-12	-9.63687710e+04	1.51162583e+01		4
P[OH]2[OME]	sikes030418C	1H	50 3P 1G	250.000 5000.000 1370.100	1
1.50656416e+01	8.87876061e-03	-3.09802383e-06	5.11981624e-10	-3.26918422e-14	2

-9.84013950e+04-4.82470994e+01 2.96199025e+00 4.96706044e-02-5.66811158e-05	3
3.23605971e-08-7.15966972e-12-9.53436862e+04 1.25511802e+01	4
CH2OPO sikes040518C 1H 2O 2P 1G 250.000 5000.000 1703.100	1
1.27519511e+01 2.58189223e-03-1.12432711e-06 2.15776717e-10-1.53125124e-14	2
-3.44442928e+04-4.01769128e+01 3.47671179e+00 2.37361976e-02-1.93386333e-05	3
7.23527844e-09-1.03739012e-12-3.11715993e+04 9.81126839e+00	4
PO[H][OME] 040518C 1H 4O 2P 1G 250.000 5000.000 1584.300	1
1.08695742e+01 8.70850864e-03-3.16121576e-06 5.37672134e-10-3.50986955e-14	2
-4.64323930e+04-2.89317006e+01 2.09012043e+00 3.11847256e-02-2.64365513e-05	3
1.18878908e-08-2.18475063e-12-4.34647201e+04 1.76969367e+01	4
PO[H][OME]O 040518C 1H 4O 3P 1G 250.000 5000.000 1590.500	1
1.48685842e+01 7.45150768e-03-2.58579922e-06 4.23326914e-10-2.67748497e-14	2
-7.22828834e+04-5.06347393e+01-1.13234550e+00 5.40970034e-02-5.56265835e-05	3
2.77104720e-08-5.30882401e-12-6.75997347e+04 3.20732588e+01	4
PO[H][OME][OCH2] 210418C 2H 6O 3P 1G 250.000 5000.000 1436.800	1
1.67562935e+01 1.30035770e-02-4.69092084e-06 7.93735438e-10-5.15921857e-14	2
-7.76454676e+04-5.58501055e+01 3.57585455e+00 5.27123774e-02-5.41323303e-05	3
2.96834747e-08-6.50399563e-12-7.36887429e+04 1.22644352e+01	4

Table A-27. DMP/TMP mechanism.

!***** PHOSPHORUS MECHANISM *****				
!***** Small oxides MECHANISM ***				
! Jayaweera (2005)				
! Assumed pcenter is at 60 atm				
! assumed that PO is not as reactive as PO2, so reduced a-factor by 2/3rds.				
PO2+PO(+M)<=>P2O3(+M)	4.000E+14	-1.000	0.0	
LOW/ 1.000E+20	-2.000	0.0	/	
! Assumed pcenter is at 30 atm				
PO2+PO2(+M)<=>P2O4(+M)	6.000E+14	-1.000	0.0	
LOW/ 2.000E+20	-2.000	0.0	/	
! Assumed pcenter is at 30 atm				
! analogy with no2+no3 reaction, but this rxn is has a deeper well, so make A-factor 3				
! times larger than atmospheric chemistry value.				
PO2+PO3(+M)<=>P2O5(+M)	6.000E+14	-1.000	0.0	
LOW/ 5.000E+20	-2.000	0.0	/	
! Twa				
PO2+OH+M<=>HOPO2+M	1.600E+24	-2.280	285.0	
H2O/16/ H2/2.5/				
! (removed times 10) Twa				
PO3+H+M<=>HOPO2+M	4.800E+24	-2.370	1430.0	
H2O/16/ H2/2.5/				
HOPO+O+M<=>HOPO2+M	1.200E+27	-2.990	2040.0	! Twa
H2O/16/ H2/2.5/				
! par inverse				
H2+PO3<=>HOPO2+H	2.000E+12	0.000	0.0	
! The above reaction occurs by chem. act route at 1 atm and below.				
! replace Ea with G2 value:				
! Chemically activated paths from Mackie et al:				
! HOPO+OH goes thru CHEmically activated path go to PO2+H2O instead:				
! Mackie, Bacskay,Haworth J.Phys.Chem.106:10825(2002)				
HOPO+OH<=>PO2+H2O	3.720E+13	-0.219	3200.0	
DUPLICATE				
! Reaction PO[OH]2+h=>:				
! Chemaster results for HOPO2+h => products, high pressure rate constants from BACMP4				
! Chemaster inputfile HOPO2_hhinp, 11/12/03				
! HOPO2+h =>products				
! (comment in rate at needed pressure, below)				
HOPO2+H<=>PO[OH]2	1.270E+32	-6.100	8702.0	
PLOG / 1.000	1.270E+32	-6.100	8702.0	/
PLOG / 3.000	3.780E+29	-5.250	8135.0	/
PLOG / 10.000	2.780E+26	-4.220	7329.0	/
PLOG / 30.000	2.610E+23	-3.240	6477.0	/
PLOG / 100.000	1.520E+20	-2.220	5508.0	/
HOPO2+H<=>PO2+H2O	5.160E+19	-1.830	10726.0	
PLOG / 1.000	5.160E+19	-1.830	10726.0	/
PLOG / 3.000	2.250E+18	-1.410	10971.0	/
PLOG / 10.000	6.800E+15	-0.660	10823.0	/
PLOG / 30.000	4.770E+12	0.270	10312.0	/
PLOG / 100.000	3.790E+08	1.450	9424.0	/
DUPLICATE				
HOPO2+H<=>PO2+H2O	1.450E+28	-4.970	44605.0	
PLOG / 1.000	1.450E+28	-4.970	44605.0	/
PLOG / 3.000	5.570E+25	-4.150	44070.0	/
PLOG / 10.000	1.200E+23	-3.270	43415.0	/
PLOG / 30.000	3.850E+20	-2.460	42738.0	/
PLOG / 100.000	9.100E+17	-1.620	41972.0	/
DUPLICATE				
! New inhibition loop for HOPO2 reacting with OH:				
! CFM estimate				
HOPO2+OH<=>PO[OH]2O	1.000E+19	-2.000	0.0	

```

! CFM estimate
PO[OH]2O+H<=>HOPO2+H2O          2.000E+13    0.000    0.0

! This reaction below has different products that Mackie who gives HOPO
! Do we keep this rxn?
! Glaude est.
PO[OH]2+H<=>HPO2+H2O          4.000E+19   -2.000    0.0

! Is the rxn below CHemically activated or an abstraction?
! Melius/Pitz est. (no Ea since O-H bond is weak)
PO[OH]2+OH<=>HOPO2+H2O        2.000E+13    0.000    0.0

! Tsang86 gives 2.4e13 for CH2OH+H=CH2O+OH
! CH2OH+H=CH2O+H2 of 6.0e12
! This looks like an abstraction, but no activation energy!
! Melius/Pitz est; Tsang87 gives
PO[OH]2+H<=>HOPO2+H2          5.000E+12    0.000    0.0

! Is this the right products or should it be mol. elimination of water?:
! Glaude est.
PO[OH]2+OH<=>PO[OH]3          1.000E+13    0.000    0.0
! Glaude est.
PO[OH]2+O<=>HOPO2+OH          5.000E+13    0.000    0.0

! Add organophos species with 2 P's: (H2O can add from above or below to
! either oxygen with either hydrogen: 2^3 in a-factor
! CFM initial est.
P2O4+H2O<=>HOPO+HOPO2        1.000E+11    0.000    0.0
! CFM initial est.
P2O5+H2O<=>HOPO2+HOPO2        1.000E+11    0.000    0.0

! Glaude est. Forward A-factor from CH3OH+O.
! CFM tried to compute adduct, and it does not exist.
! (Rxn was converting HOPO to HOPO2 under lean conditions)
HOPO2+O<=>OH+PO3              1.000E+13    0.000   12300.0

! Glaude estimate based on H2O+OH=H2O+OH
HOPO2+OH<=>H2O+PO3            1.200E+06    2.000   2000.0

! Glaude: Analogy with Tsang's cO+HO2
HOPO+HO2<=>HOPO2+OH           1.500E+14    0.000   23600.0
! Glaude est. based on Marinov's c2h5OH+HO2
HOPO2+HO2<=>H2O2+PO3           2.500E+12    0.000   24600.0

! Glaude est. based on Walker's rH+O2
HOPO2+O2<=>HO2+PO3             7.000E+12    0.000   66000.0

! Glaude est. based Tsang's CH3OH+CH3
HOPO2+CH3<=>CH4+PO3            1.500E+12    0.000   13100.0

PO+OH+M<=>HOPO+M              1.000E+21   -2.090   1590.0 !Twa
H2O/16/  H2/2.5/

! H adds to O, Twa*15/3, rate used in Wainner et al. HOTWC 2000.
PO2+H+M<=>HOPO+M              4.870E+24   -2.040    645.0
H2O/16/  H2/2.5/
DUPLICATE

! Activation barrier calculated from BACG2
! Abstraction route. Melius est. 11/27/01;
! The tst for H should be tighter than the tst for OH abstraction, therefore
! the A-factor should be lower.
HOPO+H<=>H2+PO2                1.000E+13    0.000   11000.0
! Glaude est. Forward A-factor is from CH3OH+O=CH3O+OH Ea estimated to be zero.
HOPO+O<=>OH+PO2                1.000E+13    0.000    0.0
! Glaude est.
HOPO+O<=>H+PO3                  1.000E+12    0.000   15000.0
! Atk86 Ht (abstraction route)
HOPO+OH<=>PO2+H2O              1.200E+06    2.000  -1500.0
DUPLICATE

HOPO+HO2<=>H2O2+PO2            2.500E+12    0.000   23300.0

HOPO+O2<=>HO2+PO2              7.000E+12    0.000   45300.0

HOPO+CH3<=>CH4+PO2             1.500E+12    0.000   13100.0

```

PO+O+M<=>PO2+M H2O/16/ H2/2.5/	1.600E+25	-2.630	1720.0 ! Twa
! CFM est. based on radical-radical recombination			
PO+OH<=>H+PO2	1.000E+13	0.000	0.0
! Demore97 nO+HO2			
PO+HO2<=>PO2+OH	2.100E+12	0.000	-500.0
! CFM est. Tight TST, no barrier			
PO+O2<=>PO2+O	1.000E+12	0.000	0.0
PO+CH3<=>CH3PO	1.000E+13	0.000	0.0
! (undid times 10 above)			
PO2+O+M<=>PO3+M H2O/16/ H2/2.5/	1.300E+27	-3.150	1880.0
! Twarowski, C&F, 1995.			
H+PO3<=>PO2+OH	3.160E+13	0.000	40.0
PO2+HO2<=>OH+PO3	5.000E+11	0.000	0.0
! Glaude est.			
PO2+O2<=>O+PO3	1.000E+12	0.000	30000.0
! Glanzer74 no2+CH3			
CH3+PO2<=>CH3PO2	6.300E+14	-0.600	0.0
PO2+CH3<=>CH3O+PO	5.000E+11	0.000	43300.0
PO2+CH3O<=>CH2O+HOPO			
HOPO+PO3<=>PO2+HOPO2	5.000E+11	0.000	0.0
PO3+PO<=>PO2+PO2			
CH3+PO3<=>CH3OPO2	5.000E+11	0.000	0.0
PO3+CH3<=>CH3O+PO2	5.000E+11	0.000	15300.0
REV / 5.000E+11 0.000 11000.0 /			
PO3+CH3O<=>CH2O+HOPO2	1.000E+13	0.000	0.0
CH3PO+H<=>CH3+HPO			
CH3PO+O<=>CH3+PO2	1.000E+13	0.000	0.0
CH3PO2<=>CH3PO+O	1.000E+14	0.000	133000.0
REV / 6.200E+13 0.000 3000.0 /			
H+PO+M<=>HPO+M			
H2O/16/ H2/2.5/	1.800E+22	-1.950	1330.0 ! Twa
HPO+H<=>H2+PO	2.400E+08	1.500	0.0
HPO+O<=>OH+PO	1.700E+08	1.500	0.0
HPO+O<=>PO2+H	1.000E+13	0.000	3000.0
HPO+O2<=>PO+HO2	7.000E+12	0.000	20000.0
HPO+OH<=>PO+H2O	1.200E+06	2.000	-2000.0
HPO+OH<=>PO[H][OH]	1.400E+12	0.000	0.0 ! Add
! The above reaction occurs by chem. act route at 1 atm and below:			
! Addition path. CFM decreased Mackie A-factor.			
HOPO+H<=>H2O+PO	3.000E+12	0.000	8300.0
PO[H][OH]+H<=>HOPO+H2	5.000E+13	0.000	0.0
PO[H][OH]+OH<=>HOPO+H2O	1.000E+13	0.000	0.0
PO[H][OH]+O<=>HOPO+OH	5.000E+13	0.000	0.0
HPO+HO2<=>PO+H2O2			
	2.000E+11	0.000	5000.0
HPO+PO2<=>PO+HOPO			
	2.000E+11	0.000	0.0
HPO+PO3<=>PO+HOPO2			
	2.000E+11	0.000	0.0
HPO+CH3<=>PO+CH4			
	8.100E+05	1.870	0.0
! H+PO2=> products where H adds to the P			
! H+PO2 is chemically activated. Assume 1% is stabilized and 99% goes to			
! HOPO product.			
! 1% of Twa*15/10/3			
H+PO2+M<=>HPO2+M	4.870E+21	-2.040	645.0
H2O/16/ H2/2.5/			
! Twa*15/10/3 to match Babushok			
H+PO2+M<=>HOPO+M	4.870E+23	-2.040	645.0
DUPLICATE			
H2O/16/ H2/2.5/			
! Add isomerization reaction for HPO2<=>HOPO			
! A and Ea from BACMP4 TST (used cis-HOPO)			
HPO2<=>HOPO	2.350E+14	0.000	46400.0

HPO2+H<=>H2+PO2	2.400E+08	1.500	5000.0
HPO2+H<=>PO[H][OH]	5.000E+12	0.000	5000.0
HPO2+O<=>OH+PO2	1.700E+08	1.500	2500.0
HPO2+O2<=>PO2+HO2	7.000E+12	0.000	34400.0
HPO2+OH<=>H2O+PO2	1.200E+06	2.000	-2000.0
HPO2+OH<=>H+HOPO2	1.000E+12	0.000	2000.0
HPO2+HO2<=>H2O2+PO2	2.000E+11	0.000	10000.0
HPO2+CH3<=>CH4+PO2	8.100E+05	1.870	7000.0
HPO+PO2<=>HPO2+PO	1.000E+11	0.000	0.0
HPO2+PO2<=>HOPO+PO2	5.000E+11	0.000	0.0
HPO2+PO3<=>HOPO2+PO2	5.000E+11	0.000	0.0
!**** DMMP MECHANISM *****			
POME[OME]2<=>CH2O+P[OH]ME[OME]	9.300E+13	0.000	87300.0
P[OH]ME[OME]<=>CH3OH+CH3PO	1.100E+14	0.000	42000.0
! initiations			
POME[OME][OCH2]+H<=>POME[OME]2	1.500E+14	0.000	0.0
PO[CH2][OME]2+H<=>POME[OME]2	1.500E+14	0.000	0.0
POME[OME]O+CH3<=>POME[OME]2	5.000E+12	0.000	0.0
PO[OME]2+CH3<=>POME[OME]2	5.000E+12	0.000	0.0
POME[OME]+CH3O<=>POME[OME]2	5.000E+12	0.000	0.0
! Ingham & Walker94			
POME[OME]2+O2<=>POME[OME][OCH2]+HO2	4.200E+13	0.000	52600.0
POME[OME]2+O2<=>PO[CH2][OME]2+HO2	2.100E+13	0.000	58000.0
!H-abstractions			
! Dean & Bozzelli			
POME[OME]2+H<=>POME[OME][OCH2]+H2	1.440E+09	1.500	7140.0
POME[OME]2+OH<=>POME[OME][OCH2]+H2O	7.200E+06	2.000	750.0
REV / 1.165E+07 1.770 20630.0 /			
POME[OME]2+O<=>POME[OME][OCH2]+OH	1.020E+09	1.500	5425.0
POME[OME]2+CH3<=>POME[OME][OCH2]+CH4	4.900E+06	1.870	10650.0
REV / 4.786E+07 1.640 15850.0 /			
POME[OME]2+HO2<=>POME[OME][OCH2]+H2O2	3.000E+12	0.000	21100.0
POME[OME]2+H<=>PO[CH2][OME]2+H2	7.200E+08	1.500	10650.0
POME[OME]2+O<=>PO[CH2][OME]2+OH	5.000E+08	1.500	9475.0
POME[OME]2+OH<=>PO[CH2][OME]2+H2O	3.600E+06	2.000	3450.0
REV / 3.091E+06 1.770 19130.0 /			
POME[OME]2+CH3<=>PO[CH2][OME]2+CH4	2.400E+06	1.870	14180.0
REV / 1.243E+07 1.640 15180.0 /			
POME[OME]2+HO2<=>PO[CH2][OME]2+H2O2	1.500E+12	0.000	25320.0
!Radical isomerization			
! from Curran98			
PO[CH2][OME]2<=>POME[OME][OCH2]	1.800E+12	0.000	19700.0
!Radical decompositions			
POME[OME]<=>CH3PO2+CH3	2.000E+13	0.000	36000.0
POME[OME]<=>CH3OPO+CH3	1.000E+14	0.000	32100.0
POME[OME]O<=>CH3PO2+CH3O	2.000E+13	0.000	35000.0
POME[OME]O<=>CH3OPO2+CH3	2.000E+13	0.000	34000.0
POME[OME][OCH2]<=>POME[OME]+CH2O	2.000E+13	0.000	38950.0
!Radical combinations			
POME[OME]+H<=>PO[H]ME[OME]	1.500E+14	0.000	0.0
POME[OME]+OH<=>PO[OH]ME[OME]	1.000E+13	0.000	0.0
POME[OME]+O<=>POME[OME]O	5.000E+13	0.000	0.0
PO[OME]2+OH<=>PO[OH][OME]2	1.000E+13	0.000	0.0
PO[OME]2+O<=>PO[OME]2O	5.000E+13	0.000	0.0
POME[OME][OCH2]+OH<=>POME[OME]O+CH2OH	1.000E+13	0.000	0.0
POME[OME][OCH2]+O<=>POME[OME]O+CH2O	5.000E+13	0.000	0.0
PO[CH2][OME]2+OH<=>PO[OME]2+CH2OH	1.000E+13	0.000	0.0
PO[CH2][OME]2+O<=>PO[OME]2+CH2O	5.000E+13	0.000	0.0
PO[H]ME[OME]+H<=>POME[OME]+H2	6.800E+13	0.000	8100.0

PO[H]ME[OME]+OH<=>POME[OME]+H2O	1.200E+06	2.000	-1500.0
PO[H]ME[OME]+O<=>POME[OME]+OH	1.000E+13	0.000	0.0
!Additions			
! remove h additions to the "O" on P=O since Melius calcs show this does not happen.			
POME[OME]2+OH<=>PO[OH][OME]2+CH3	3.600E+13	-0.530	2300.0
POME[OME]2+OH<=>PO[OH]ME[OME]+CH3O	7.200E+13	-0.540	6200.0
! ** PO[OH][OME]2 sub-MECHANISM *			
PO[OH][OME]2<=>CH3OPO2+CH3OH	2.500E+13	0.000	44000.0
PO[OH][OME]2+H<=>PO[OH]OME[OCH2]+H2	1.440E+09	1.500	7140.0
PO[OH][OME]2+O<=>PO[OH]OME[OCH2]+OH	1.020E+09	1.500	5425.0
PO[OH][OME]2+OH<=>PO[OH]OME[OCH2]+H2O	7.200E+06	2.000	750.0
PO[OH][OME]2+CH3<=>PO[OH]OME[OCH2]+CH4	4.900E+06	1.870	10650.0
PO[OH][OME]2+HO2<=>PO[OH]OME[OCH2]+H2O2	3.000E+12	0.000	21100.0
PO[OH]OME[OCH2]<=>PO[OH][OME]+CH2O	2.000E+13	0.000	38950.0
PO[OH][OME]<=>HOPO2+CH3	2.000E+13	0.000	36000.0
REV / 1.000E+12 0.000 19000.0 /			
PO[OH][OME]<=>HOPO+CH3O	1.000E+14	0.000	40400.0
CH3OPO2+H<=>PO[OH][OME]	1.000E+13	0.000	5000.0
PO[OH]OME[OCH2]+H<=>PO[OH][OME]2	1.500E+14	0.000	0.0
PO[OH][OME]+H<=>PO[H][OH][OME]	1.500E+14	0.000	0.0
PO[OH][OME]+OH<=>PO[OH]2[OME]	1.000E+13	0.000	0.0
PO[OH][OME]+O<=>HOPO2+CH3O	5.000E+13	0.000	0.0
! remove h additions to the "O" on P=O since Melius calcs show this does not happen.			
PO[OH][OME]2+OH<=>PO[OH]2[OME]+CH3O	1.000E+12	0.000	2000.0
! ** PO[OH]ME[OME] sub-MECHANISM *			
PO[OH]ME[OME]<=>CH3PO2+CH3OH	2.500E+13	0.000	44000.0
! as CH3coOH to co2			
PO[OH]ME[OME]<=>CH3OPO2+CH4	3.000E+11	0.000	61000.0
PO[OH]ME[OME]+H<=>PO[OH]ME[OCH2]+H2	7.200E+08	1.500	7140.0
PO[OH]ME[OME]+H<=>PO[OH][OME][CH2]+H2	7.200E+08	1.500	10650.0
PO[OH]ME[OME]+O<=>PO[OH]ME[OCH2]+OH	5.000E+09	1.500	5425.0
PO[OH]ME[OME]+O<=>PO[OH][OME][CH2]+OH	5.000E+08	1.500	9475.0
PO[OH]ME[OME]+OH<=>PO[OH]ME[OCH2]+H2O	3.600E+06	2.000	750.0
PO[OH]ME[OME]+OH<=>PO[OH][OME][CH2]+H2O	3.600E+06	2.000	3450.0
PO[OH]ME[OME]+CH3<=>PO[OH]ME[OCH2]+CH4	2.400E+06	1.870	10650.0
REV / 2.182E+07 1.660 15750.0 /			
PO[OH]ME[OME]+CH3<=>PO[OH][OME][CH2]+CH4	2.400E+06	1.870	14180.0
REV / 1.157E+07 1.660 15180.0 /			
PO[OH]ME[OME]+HO2<=>PO[OH]ME[OCH2]+H2O2	1.500E+12	0.000	21100.0
PO[OH]ME[OME]+HO2<=>PO[OH][OME][CH2]+H2O2	1.500E+12	0.000	25320.0
PO[OH][OME][CH2]<=>PO[OH]ME[OCH2]	1.800E+12	0.000	19300.0
REV / 9.000E+11 0.000 24700.0 /			
PO[OH]ME[OCH2]<=>PO[OH]ME+CH2O	2.000E+13	0.000	38950.0
! changed barrier CFM and products			
CH3PO2+H<=>HOPO+CH3	1.000E+13	0.000	0.0
CH3PO+OH<=>PO[OH]ME	1.400E+12	0.000	0.0
! changed barrier CFM			
HOPO+CH3<=>PO[OH]ME	1.000E+12	0.000	0.0
PO[OH][OME][CH2]+H<=>PO[OH]ME[OME]	1.500E+14	0.000	0.0
PO[OH]ME[OCH2]+H<=>PO[OH]ME[OME]	1.500E+14	0.000	0.0
! remove h additions to the "O" on P=O since Melius calcs show this does not happen.			
PO[OH]ME[OME]+OH<=>PO[OH]2[OME]+CH3	1.000E+13	-0.340	2200.0
PO[OH]ME[OME]+OH<=>PO[OH]2ME+CH3O	1.300E+13	-0.370	6270.0
! ** PO[OH]2[OME] sub-MECHANISM *			
PO[OH]2[OME]<=>HOPO2+CH3OH	2.500E+13	0.000	46000.0
! leave following reverse rate const.			
! Reference indicates is was necessary for Glaude et al. to			

```

! increase reverse Ea by 2 kcal, so reverse rate is important
PO[OH]2[OME]<=>CH3OPO2+H2O          5.000E+13    0.000    46000.0
REV / 1.470E+09    0.670    30.0 /    ! thermo E+2

PO[OH]2[OME]+H<=>PO[OH]2[OCH2]+H2      7.200E+08    1.500    7140.0
PO[OH]2[OME]+O<=>PO[OH]2[OCH2]+OH      5.000E+09    1.500    5425.0
PO[OH]2[OME]+OH<=>PO[OH]2[OCH2]+H2O    3.600E+06    2.000    750.0
PO[OH]2[OME]+CH3<=>PO[OH]2[OCH2]+CH4    2.400E+06    1.870    10650.0
PO[OH]2[OME]+HO2<=>PO[OH]2[OCH2]+H2O2  1.500E+12    0.000    21100.0
PO[OH]2[OCH2]<=>CH2O+PO[OH]2          2.000E+13    0.000    38950.0

PO[OH]2[OCH2]+H<=>PO[OH]2[OME]          1.500E+14    0.000    0.0
! remove h additions to the "O" on P=O since Melius calcs show this does not happen.
PO[OH]2[OME]+OH<=>PO[OH]3+CH3O          1.000E+12    0.000    2000.0

! ** PO[OH]2[me] sub-MECHANISM *

PO[OH]2ME<=>CH3PO2+H2O          5.000E+13    0.000    39000.0
PO[OH]2ME<=>HOPO2+CH4          6.000E+11    0.000    61000.0
PO[OH]2ME+OH<=>PO[OH]3+CH3        1.000E+12    0.000    2000.0

! ** PO[OH]3 sub-MECHANISM *

! from reverse rate of 2.72E+13 exp(-4.67E+04cal/RT)
HOPO2+H2O<=>PO[OH]3          5.920E+17    -1.348    8470.0
! where Ea is from BACG2 TST and A-factor multiplied by 0.54 to
! match Glaude et al. forward rate at 1000K. Glaude found results are very sensitive to
! the fwd rate const. Forward Ea from BACG2 TST is 8.0 kcal/mole

! ** CH3PO2 sub-MECHANISM *

CH3PO2+OH<=>HOPO2+CH3          1.000E+12    0.000    2000.0

! ** CH3OPO2 sub-MECHANISM *

CH3OPO2+OH<=>HOPO2+CH3O          1.000E+12    0.000    2000.0

CH3OPO2+H<=>CH2OPO2+H2          7.200E+08    1.500    4860.0
CH3OPO2+OH<=>CH2OPO2+H2O        3.600E+06    2.000    -1000.0
CH3OPO2+O<=>CH2OPO2+OH          5.000E+08    1.500    2800.0

CH3OPO2+O<=>CH3OPO+O2          5.000E+12    0.000    15000.0

CH2OPO2<=>CH2O+PO2            2.000E+13    0.000    21000.0

! ** Eliminations "a 3 centres" *****

PO[H]ME[OME]<=>CH3PO+CH3OH          7.000E+13    0.000    55000.0
PO[H][OH][OME]<=>HOPO+CH3OH          7.000E+13    0.000    45000.0
PO[H][OH][OME]<=>H2O+CH3OPO          7.000E+13    0.000    46000.0

! ** P trivalent sub-MECHANISM ***
! Reverse barrier is 34.6 kcal/mole from BAC-G2:
! G2P730C is the transition state
! From BAC code, k=2*2*10^10.37*e(-18.55/RT) Ea at 600K.
! (2*2 is for degeneracy of how H2O approaches)
HOPO+H2O<=>P[OH]3          9.400E+10    0.000    18550.0
HOPO+CH3OH<=>P[OH]2[OME]      5.000E+11    0.000    3000.0
REV / 2.500E+13    0.000    43000.0 /
CH3OPO+H2O<=>P[OH]2[OME]      1.000E+12    0.000    2000.0
REV / 2.500E+13    0.000    46000.0 /

! ***** TMP MECHANISM *****

PO[OME]2[OCH2]+H<=>PO[OME]3          1.500E+14    0.000    0.0
PO[OME]2+CH3O<=>PO[OME]3          5.000E+12    0.000    0.0
PO[OME]2O+CH3<=>PO[OME]3          5.000E+12    0.000    0.0
PO[OME]3+O2<=>PO[OME]2[OCH2]+HO2    6.300E+13    0.000    52600.0
PO[OME]3+H<=>PO[OME]2[OCH2]+H2      2.200E+09    1.500    7140.0
PO[OME]3+O<=>PO[OME]2[OCH2]+OH      1.500E+09    1.500    5425.0
PO[OME]3+OH<=>PO[OME]2[OCH2]+H2O    1.100E+07    2.000    750.0
PO[OME]3+CH3<=>PO[OME]2[OCH2]+CH4    7.200E+06    1.870    10650.0
PO[OME]3+HO2<=>PO[OME]2[OCH2]+H2O2  4.500E+12    0.000    21100.0
PO[OME]2O<=>CH3OPO2+CH3O          4.000E+13    0.000    37700.0
PO[OME]2[OCH2]+OH<=>PO[OME]2O+CH2OH  1.000E+13    0.000    0.0
PO[OME]2[OCH2]+O<=>PO[OME]2O+CH2O    5.000E+13    0.000    0.0

```

PO[OME]2[OCH2]<=>PO[OME]2+CH2O	2.000E+13	0.000	38950.0
PO[OME]3+OH<=>PO[OH][OME]2+CH3O	1.000E+12	0.000	2000.0
! *****			
! ***** CH3OPO MECHANISM *****			
! *****			
! ***** New Calculations *****			
! *****			
CH3OPO+H<=>HPO2+CH3	2.000E+12	0.000	2000.0
CH3OPO+OH<=>PO[OH][OME]	1.400E+12	0.000	0.0
CH3OPO+O<=>CH3OPO2	1.000E+12	0.000	0.0
CH3OPO+O<=>CH3+PO3	5.000E+12	0.000	0.0
CH3OPO+O<=>CH3O+PO2	2.000E+12	0.000	0.0
! Rate constants calculated with PES obtained at the G3X-K level of theory,			
! using hindered rotor correction. Master equation solved with the MESMER software			
! Arrhenius parameters are valid in the 500-2500 K temperature range			
CH3OPO<=>H+CH2OPO	1.105E+37	-7.840	107755.4
PLOG / 0.010	3.606E+80	-21.187	142448.3 /
PLOG / 0.100	8.758E+16	-2.899	97542.1 /
PLOG / 1.000	1.105E+37	-7.840	107755.4 /
PLOG / 10.000	1.124E+48	-10.162	117449.7 /
PLOG / 100.000	2.130E+40	-7.427	116032.1 /
CH3OPO<=>CH3O+PO	4.186E+52	-12.255	122309.3
PLOG / 0.010	7.944E+34	-9.014	95140.9 /
PLOG / 0.100	2.152E+19	-4.199	84702.1 /
PLOG / 1.000	4.186E+52	-12.255	122309.3 /
PLOG / 10.000	1.464E+49	-10.697	117806.1 /
PLOG / 100.000	6.429E+41	-8.101	116489.3 /
CH3OPO<=>CH3+PO2	1.046E+43	-8.599	82114.2
PLOG / 0.010	3.763E+48	-10.850	81408.7 /
PLOG / 0.100	1.159E+48	-10.329	82962.9 /
PLOG / 1.000	1.046E+43	-8.599	82114.2 /
PLOG / 10.000	1.831E+37	-6.735	80785.3 /
PLOG / 100.000	5.570E+28	-4.197	76630.9 /
CH3OPO<=>CH2O+HPO	3.185E+33	-6.184	67917.6
PLOG / 0.010	3.088E+42	-9.174	69366.4 /
PLOG / 0.100	5.850E+37	-7.603	68419.9 /
PLOG / 1.000	3.185E+33	-6.184	67917.6 /
PLOG / 10.000	2.829E+24	-3.474	63622.9 /
PLOG / 100.000	1.571E+15	-0.767	58555.2 /
CH2OPO+H<=>CH3+PO2	8.382E+14	-0.452	701.2
PLOG / 0.010	5.778E+14	-0.407	581.5 /
PLOG / 0.100	7.231E+14	-0.435	640.9 /
PLOG / 1.000	8.382E+14	-0.452	701.2 /
PLOG / 10.000	4.450E+16	-0.915	2504.6 /
PLOG / 100.000	3.514E+15	-0.539	4460.2 /
CH2OPO+H<=>CH2O+HPO	5.773E+12	0.058	-299.9
PLOG / 0.010	5.838E+12	0.057	-286.7 /
PLOG / 0.100	5.803E+12	0.058	-290.6 /
PLOG / 1.000	5.773E+12	0.058	-299.9 /
PLOG / 10.000	9.990E+13	-0.272	1066.5 /
PLOG / 100.000	1.223E+13	0.051	3135.1 /
! Rate constants calculated with PES obtained at the G3X-K level of theory,			
! using hindered rotor correction. Master equation solved with the MESMER software			
! Arrhenius parameters are valid in the 500-2500 K temperature range			
CH3OPO+H<=>CH2OPO+H2	7.061E+05	2.616	7142.8
CH3OPO+CH3<=>CH2OPO+CH4	3.832E-01	3.817	8673.2
CH3OPO+OH<=>CH2OPO+H2O	2.453E-01	3.799	-1671.5
CH2OPO<=>CH2O+PO	3.532E+32	-6.213	39043.7
PLOG / 0.010	1.022E+30	-6.088	35117.6 /
PLOG / 0.100	5.567E+31	-6.282	37105.5 /
PLOG / 1.000	3.532E+32	-6.213	39043.7 /
PLOG / 10.000	1.039E+31	-5.499	39966.9 /
PLOG / 100.000	1.187E+26	-3.863	38842.4 /

```

! *****
! ***** DMP MECHANISM *****
! *****

! PO[H][OME]2<=>CH3OPO+CH3OH          7.000E+13    0.000  46000.0
! PO[OME]2+H<=>PO[H][OME]2            1.500E+14    0.000    0.0

! PO[H][OME]2+H<=>PO[OME]2+H2          6.800E+13    0.000   8100.0
! PO[H][OME]2+OH<=>PO[OME]2+H2O        1.200E+06    2.000  -1500.0
! PO[H][OME]2+O<=>PO[OME]2+OH          1.000E+13    0.000    0.0
! PO[H][OME]2<=>CH3OPO+CH3OH          7.000E+13    0.000  46000.0

! PO[OME]2<=>CH3OPO2+CH3                4.000E+13    0.000  36000.0
! PO[OME]2<=>CH3OPO+CH3O                2.000E+14    0.000  45100.0

!---- DiMethylPhosphite Unimolecular Decomposition ----

! Rate constants calculated with PES obtained at the G3X-K level of theory,
! using hindered rotor correction. Master equation solved with the MESMER software
! Arrhenius parameters are valid in the 500-2500 K temperature range

PO[H][OME]2<=>CH3+PO[H][OME]O          8.872E+51   -10.573  111864.6
PLOG / 0.010    7.260E+77   -18.340  124051.2 /
PLOG / 0.100    6.075E+61   -13.567  115612.4 /
PLOG / 1.000    8.872E+51   -10.573  111864.6 /
PLOG / 10.000   2.329E+38    -6.634  103955.4 /
PLOG / 100.000  1.973E+24    -2.654   94111.0 /

PO[H][OME]2<=>CH3O+PO[H][OME]          1.414E+77   -17.704  149735.0
PLOG / 0.010    4.159E+84   -20.802  143113.0 /
PLOG / 0.100    3.995E+84   -20.238  149219.4 /
PLOG / 1.000    1.414E+77   -17.704  149735.0 /
PLOG / 10.000   5.955E+61   -13.090  143260.1 /
PLOG / 100.000  2.842E+38    -6.470  127333.9 /

PO[H][OME]2<=>H+PO[H][OME][OCH2]       7.158E+69   -15.526  138909.5
PLOG / 0.010    1.369E+84   -20.398  138240.4 /
PLOG / 0.100    1.171E+77   -17.949  138500.5 /
PLOG / 1.000    7.158E+69   -15.526  138909.5 /
PLOG / 10.000   1.481E+47    -8.971  125025.2 /
PLOG / 100.000  1.586E+27    -3.291  111610.7 /

PO[H][OME]2<=>H+PO[OME]2                1.067E+56   -11.620  120083.4
PLOG / 0.010    2.330E+81   -19.349  130436.8 /
PLOG / 0.100    3.656E+71   -16.234  127867.6 /
PLOG / 1.000    1.067E+56   -11.620  120083.4 /
PLOG / 10.000   8.366E+37    -6.389  109101.4 /
PLOG / 100.000  2.914E+24    -2.538  100485.0 /

PO[H][OME]2<=>CH3OH+CH3OPO             4.364E+33    -5.949   84495.4
PLOG / 0.010    1.022E+64   -14.728  103104.5 /
PLOG / 0.100    1.449E+47    -9.861   92608.9 /
PLOG / 1.000    4.364E+33    -5.949   84495.4 /
PLOG / 10.000   8.972E+21    -2.598   77107.4 /
PLOG / 100.000  7.963E+11     0.247   70203.7 /

PO[H][OME]2<=>CH2O+H2+CH3OPO           6.069E+37    -7.204   95816.8
PLOG / 0.010    2.877E+65   -15.382  110189.8 /
PLOG / 0.100    7.537E+52   -11.608  104363.4 /
PLOG / 1.000    6.069E+37    -7.204   95816.8 /
PLOG / 10.000   1.812E+22    -2.748   86021.8 /
PLOG / 100.000  2.827E+08     1.162   76567.1 /

! Temporary rate constants since no Hindered Rotor correction nor pressure dependence
!
PO[H][OME]<=>CH3+HPO2                    4.059E+12     0.450   36718.0
PO[H][OME]<=>H+CH3OPO                    8.854E+12     0.590   28813.0

PO[H][OME]O<=>H+CH3OPO2                 6.232E+12     0.400   21083.0

!---- DiMethylPhosphite H Abstraction Reactions ----
! Rate constants calculated with PES obtained at the G3X-K level of theory,
! using hindered rotor correction. Master equation solved with the MESMER software

```

! Arrhenius parameters are valid in the 500-2500 K temperature range

PO[H][OME]2+H<=>PO[H][OME][OCH2]+H2	3.858E+06	2.502	7179.9
PO[H][OME]2+H<=>PO[OME]2+H2	2.447E+07	1.972	4242.2
PO[H][OME]2+CH3<=>PO[H][OME][OCH2]+CH4	3.457E+00	3.688	9820.2
PO[H][OME]2+CH3<=>PO[OME]2+CH4	7.804E+01	3.037	5237.0
PO[H][OME]2+OH<=>PO[H][OME][OCH2]+H2O	2.441E+06	2.184	58.8
PO[H][OME]2+OH<=>PO[OME]2+H2O	4.208E+05	2.180	69.3

!---- DMP Radicals Decomposition reactions ----

! Rate constants calculated with PES obtained at the G3X-K level of theory,
! using hindered rotor correction. Master equation solved with the MESMER software
! Arrhenius parameters are valid in the 500-2500 K temperature range

PO[H][OME][OCH2]<=>PO[OME]2	1.002E+43	-9.534	41422.3
PLOG / 0.010	1.589E+55	-13.748	42968.8 /
PLOG / 0.100	1.019E+43	-9.856	38810.7 /
PLOG / 1.000	1.002E+43	-9.534	41422.3 /
PLOG / 10.000	1.502E+39	-8.172	41589.2 /
PLOG / 100.000	1.134E+30	-5.368	37972.2 /

PO[H][OME][OCH2]<=>CH2O+PO[H][OME]	1.040E+36	-7.132	46540.2
PLOG / 0.010	8.392E+26	-5.334	35859.5 /
PLOG / 0.100	5.902E+33	-6.870	42341.2 /
PLOG / 1.000	1.040E+36	-7.132	46540.2 /
PLOG / 10.000	4.844E+31	-5.596	46621.0 /
PLOG / 100.000	9.748E+21	-2.640	42564.9 /

PO[OME]2<=>CH3+CH3OPO2	2.473E+44	-9.328	54071.6
PLOG / 0.010	1.748E+42	-9.360	47881.5 /
PLOG / 0.100	2.509E+44	-9.645	51498.9 /
PLOG / 1.000	2.473E+44	-9.328	54071.6 /
PLOG / 10.000	1.715E+40	-7.863	54112.1 /
PLOG / 100.000	7.616E+31	-5.268	51106.2 /

PO[OME]2<=>CH3O+CH3OPO	8.444E+44	-9.629	55786.1
PLOG / 0.010	8.051E+41	-9.455	48892.6 /
PLOG / 0.100	8.592E+44	-9.968	53101.2 /
PLOG / 1.000	8.444E+44	-9.629	55786.1 /
PLOG / 10.000	1.753E+40	-7.998	55621.2 /
PLOG / 100.000	2.553E+32	-5.530	53139.6 /

PO[OME]2<=>CH2O+PO[H][OME]	4.345E+60	-14.306	72892.3
PLOG / 0.010	3.399E+46	-11.105	55026.9 /
PLOG / 0.100	2.464E+55	-13.220	64367.5 /
PLOG / 1.000	4.345E+60	-14.306	72892.3 /
PLOG / 10.000	4.193E+60	-13.912	79592.5 /
PLOG / 100.000	1.981E+53	-11.498	82632.0 /

PO[H][OME][OCH2]<=>CH3+CH3OPO2	9.719E+50	-11.223	58099.0
PLOG / 0.010	3.139E+37	-8.068	41448.9 /
PLOG / 0.100	6.747E+45	-10.101	50133.7 /
PLOG / 1.000	9.719E+50	-11.223	58099.0 /
PLOG / 10.000	2.639E+50	-10.736	63650.1 /
PLOG / 100.000	3.045E+42	-8.221	65159.3 /

PO[H][OME][OCH2]<=>CH3O+CH3OPO	2.050E+50	-11.184	58691.1
PLOG / 0.010	1.753E+36	-7.904	41645.2 /
PLOG / 0.100	6.852E+44	-9.991	50470.8 /
PLOG / 1.000	2.050E+50	-11.184	58691.1 /
PLOG / 10.000	2.172E+50	-10.844	64758.6 /
PLOG / 100.000	2.385E+42	-8.305	66465.0 /

Table A-28. DMP/TMP submechanism transport properties.

PO[OH]2O	2	527.600	5.580	0.000	0.000	1.000 ! pag
PO	1	346.400	4.395	0.000	0.000	1.000 ! pag
PO2	2	410.600	4.842	0.000	0.000	1.000 ! pag
PO3	2	468.200	5.217	0.000	0.000	1.000 ! pag
HPO	2	350.700	4.426	0.000	0.000	1.000 ! pag
HPO2	2	104.887	4.814	3.085	3.382	1.000 ! pag
HOPO	2	96.875	4.962	1.864	3.706	1.000
HOPO2	2	471.700	5.239	0.000	0.000	1.000 ! pag
PO[H][OH]	2	418.200	4.892	0.000	0.000	1.000 ! pag
PO[OH]2	2	475.100	5.261	0.000	0.000	1.000 ! pag
PO[OH]3	2	530.700	5.602	0.000	0.000	1.000 ! pag
CH3PO	2	406.900	4.817	0.000	0.000	1.000 ! pag
CH3PO2	2	464.900	5.196	0.000	0.000	1.000 ! pag
CH3POPO	2	132.900	5.288	2.470	5.470	1.000 !
CH3OPO2	2	518.000	5.526	0.000	0.000	1.000 ! pag
PO[OH]2ME	2	524.400	5.565	0.000	0.000	1.000 ! pag
PO[OH]2[OME]	2	573.500	5.855	0.000	0.000	1.000 ! pag
PO[OH]2[OCH2]	2	570.500	5.838	0.000	0.000	1.000 ! pag
PO[OH]ME	2	468.400	5.218	0.000	0.000	1.000 ! pag
PO[OH][OME]	2	521.200	5.546	0.000	0.000	1.000 ! pag
PO[H]ME[OME]	2	518.200	5.527	0.000	0.000	1.000 ! pag
PO[H][OME]2	2	300.674	5.444	2.783	7.639	1.000 !
P[OH]ME[OME]	2	518.200	5.527	0.000	0.000	1.000 ! pag
POME[OME]	2	514.900	5.507	0.000	0.000	1.000 ! pag
PO[OME]2	2	352.941	5.324	1.706	8.012	1.000 !
PO[OH]ME[OME]	2	567.600	5.821	0.000	0.000	1.000 ! pag
PO[OH]ME[OCH2]	2	564.600	5.803	0.000	0.000	1.000 ! pag
PO[OH][OME][CH2]	2	564.600	5.803	0.000	0.000	1.000 ! pag
POME[OME]O	2	564.600	5.803	0.000	0.000	1.000 ! pag
PO[OH][OME]2	2	614.100	6.088	0.000	0.000	1.000 ! pag
PO[OME]2O	2	611.200	6.072	0.000	0.000	1.000 ! pag
PO[OH]OME[OCH2]	2	611.200	6.072	0.000	0.000	1.000 ! pag
POME[OME]2	2	608.500	6.056	0.000	0.000	1.000 ! pag
POME[OME][OCH2]	2	605.600	6.04	0.000	0.000	1.000 ! pag
PO[CH2][OME]2	2	605.600	6.04	0.000	0.000	1.000 ! pag
PO[OME]3	2	652.900	6.303	0.000	0.000	1.000 ! pag
PO[OME]2[OCH2]	2	650.100	6.288	0.000	0.000	1.000 ! pag
CH2OPO2	2	515.000	5.51	0.000	0.000	1.000 ! pag
PO[H][OH][OME]	2	524.400	5.56	0.000	0.000	1.000 ! pag
P[OH]3	2	478.600	5.28	0.000	0.000	1.000 ! pag
P[OH]2[OME]	2	524.400	5.56	0.000	0.000	1.000 ! pag
! wjp: same as po[oh]3						
P2O3	2	530.700	5.602	0.000	0.000	1.000 !
P2O4	2	530.700	5.602	0.000	0.000	1.000 !
P2O5	2	530.700	5.602	0.000	0.000	1. !
PO[H][OME]O	2	518.000	5.526	3.198	6.688	1.000 ! pag
PO[H][OME]	2	132.900	5.288	2.619	5.831	1.000 !
PO[H][OME][OCH2]	2	300.674	5.444	1.953	7.312	1.000 !
CH2OPO	2	132.900	5.288	1.965	6.251	1.000 !